UNIQUE TEMPLATING OF AND APPLICATIONS ENABLED THROUGH MESOPOROUS COLLOIDS

BY

MATTHEW DAVE GOODMAN

DISSERTATION

Submitted in partial fulfillment of the requirements
for the degree of Doctor of Philosophy in Materials Science and Engineering
in the Graduate College of the
University of Illinois at Urbana-Champaign, 2014

Urbana, Illinois

Doctoral Committee:

Professor Paul V. Braun, Chair
Assistant Professor Lane W. Martin
Assistant Professor Shen Dillon
Professor Kenneth S. Suslick

ABSTRACT

This work describes the templating process and applications enabled by utilizing mesoporous colloids, colloidal crystals, and films. Silica colloidal crystals, having colloids of less than 300 nm, were fabricated and used as a template for silicon deposition. Brillouin Light Scattering (BLS) experiments conducted on a silicon templated silica colloidal crystal show unusual behavior in the BLS spectrum where the Stokes and anti-Stokes phonon intensities were asymmetrical. The dispersion relationship between the phonon frequencies and wave vectors had no phononic band bending, possibility due to the unusual phenomenon.

Mesoporous silica was used as a template for platinum and silicon deposition. After a successful colloidal crystal fabrication from mesoporous silica colloids, platinum was deposited and partially infiltrated the mesopores. Removing the silica template revealed a mesoporous platinum shell, replicating the mesopores of the colloids and the colloidal crystal structures. The silicon-silica composite was used to study the thermal conductivity of the confined silicon. Polycrystalline silicon, deposited as a reference, was shown to have a thermal conductivity of 38 $W\ m^{-1}K^{-1}$; the silicon-silica composite had an effective thermal conductivity between 2.2 and 2.4 $W\ m^{-1}K^{-1}$, an order of magnitude less than the polycrystalline film. Material thermal conductivity of the silicon could not be determined with simple modeling; accurate results need a more detailed investigation.

The first successful carbon colloidal crystal is fabricated through tailoring the surface charge of the individual colloids through a partial oxidation. This colloidal crystal was used as a unique template for a variety of materials. The templated materials penetrate deep into the mesopores,

creating a nanostructured inverse opal after carbon removal. Crucially, the carbon removal is completely orthogonal to the deposited material removal, allowing thorough template replication and preserving the fine-scale mesostructure of the colloid. This approach can be generalized for templating materials, which are inherently difficult to template with conventional colloidal crystals.

Two major applications were investigated utilizing the mesoporous colloids. The first involved the templating of titania for improvement in dye-sensitized solar cells. A carbon colloidal crystal could successfully be fabricated on the conductive glass substrate after an initial titania deposition. Titania was deposited and infiltrated the mesoporous carbon colloidal crystal template. After titania crystallization, the carbon was removed orthogonally through a simple oxidation, followed by solar cell assembly. The performance of the cell indicated low dye loading in the titania nanostructure; however, experiments to increase the dye loading were unsuccessful.

The second major application investigated also utilized the carbon colloidal crystal. Lithium battery anodes were fabricated by having the active materials, silicon and Fe_3O_4, inside the mesopores. The mesoporous carbon is unique in that it provides a porous, conductive network, allowing both electrolyte diffusion and electron extraction, and confines the active materials. This confinement minimizes capacity loss through electrical isolation of the active materials and suppresses any pulverization or migration. The silicon-carbon anode showed stability through 85 cycles after the addition of vinylene carbonate to the electrolyte, effectively stabilizing the solid-electrolyte interface. The Fe_3O_4-carbon anode showed excellent coulombic efficiency with a

dramatic decrease in the charge hysteresis, from 0.90 V in conventional systems to 0.60 V in the templated, confined anode, attributed to the confinement of the Fe_3O_4 active material. Preliminary magnetic measurements were also conducted on the deposited iron-carbon composite, showing unique behavior.

To Stac

ACKNOWLEDGMENTS

This work is the culmination of years of work that could not have been accomplished without the support of a number of people. My advisor, Prof. Paul Braun, provided me with indispensable guidance on my doctoral research, yet still allowed personal pursuits on various topics. Additionally, his support outside the research lab was instrumental in my development, be it in academic courses, career options, or a myriad of other endeavors. My Toyota collaborators, Dr. Kazuhisa Yano and Dr. Narihito Tatsuda, were a tremendous asset: their numerous discussions on the research projects and the extensive mesoporous samples they provided allowed for some truly unique results. I would also like to acknowledge my committee members, Prof. Lane W. Martin, Prof. Shen Dillon, and Prof. Kenneth S. Suslick, for providing valuable feedback and critical assessment.

In the Braun group, I have worked with some amazing people who have significantly assisted in my progress. Dr. Matthew George was instrumental when I first arrived and helped me settle into research at the University of Illinois. Dr. Dara Gough provided numerous discussions on various chemistries, allowed me a place to stay for a summer in Albuquerque, and was always up for a game of soccer. Dr. Abby Juhl, Dr. Mark Losego, Dr. Sidhartha Gupta, Dr. Aaron Jackson, Dr. Erik Nelson, Dr. Joe Geddes, Dr. Jiung Cho, Bibek Parajuli, and Ha Seong Kim have all helped through discussions, running samples for me, or teaching me a new technique. Dr. Agustin Mihi, Dr. Kevin Arpin, Dr. Hui (Steven) Zhang, and Dr. Hailong Ning have all been influential and contributed significantly to my success. Current group members of James Pikul, Chunjie Zhang, Neil Krueger, Junjie Wang, Jin Gu Kang, Runyu Zhang, and Osman Cifci have also been helpful in their discussions and suggestions. A special thanks to Sanghyeon Kim and Qiye Zheng, who

helped fabricate and run the last few experiments. Additionally, I'd like to thank David Gross, who assisted in the FIB liftouts in the iron oxide work. To everyone else in the Braun group, past and present, thank you for making these years here memorable.

The work presented here benefited from financial support by Toyota Central R&D and the U.S. Department of Energy 'Light Material Interactions in Energy Conversion' Energy Frontier Research Center under grant DE-SC0001293. Additionally, this work was carried out in part in the Frederick Seitz Materials Research Laboratory Central Research Facilities, University of Illinois. I would like to thank all the staff in the MRL and Beckman who trained, assisted, or ran samples for me.

Furthermore, I would like to acknowledge all the support staff that made things easier for me. Erica Malloch, thank you for your tireless help and assistance in keeping my schedule coordinated with Prof. Braun's. The support staffs in the Materials Science Department and the MRL offices have been amazing: Judy Brewer, Michelle Malloch, Kimberly Anderson, Debbie Kluge, Sandy Helregel, Cindy Brya, Susie Lighty and Chris Jones.

Finally, I would like to thank my family for their support. To my parents, thank you for pushing me to pursue my passions. Cassie and Philip: I thank you for always providing a joke, a much-needed distraction, and even a grounding rod. Stacy, thanks for your love, support, encouragement, and perspective.

TABLE OF CONTENTS

CHAPTER 1

INTRODUCTION

Chapter 1 introduces the key components and background of the work presented in this thesis: colloidal crystals, their optical properties, and typical fabrication routes. Current templating strategies involving colloidal crystals are described and specific applications presented. Additionally, limitations in the materials available for conventional colloidal crystals and the subsequent templating strategies are illustrated. Chapter 2 describes work done using non-porous silica colloids for Brillouin Light Scattering experiments. By depositing silicon on a silica colloidal crystal, the phononic band structure of the composite is investigated; this work was done in collaboration with Dr. Huihui Pan and Prof. Jay Bass. Chapter 3 provides two examples of templated materials utilizing mesoporous silica. Platinum was deposited into the mesopores of silica colloids arranged in a colloidal crystal. Additionally, silicon was deposited into mesopores with preliminary thermal transport experiments conducted. Initial work done on mesoporous carbon colloids are presented in Chapter 4. After fabrication into a colloidal crystal, the carbon is used as a unique template to create porous oxide and semiconductor inverse opals. Results in this chapter have been published in *Advanced Optical Materials* [1]. The mesoporous carbon colloidal crystals were then used as templates for titania infiltration, shown in Chapter 5. The carbon was removed and the porous titania investigated for dye-sensitized solar cell applications. Chapter 6 expands on the carbon template with silicon and iron deposited in the mesopores. The iron was oxidized to Fe_3O_4 without removing the carbon template and thoroughly characterized. The Fe_3O_4-carbon and the silicon-carbon composites were tested as anodes for lithium batteries. Finally, Chapter 7 presents overall conclusions of this work.

1.1 Colloidal Crystals and Their Optical Properties

Colloidal crystals are periodic assemblies of colloidal particles, typically (but not necessarily) less than 1 μm in diameter. Most commonly, the colloids are arranged in a hexagonal, close-packed face-center cubic (FCC) structure [2]. Other crystal structures have been formed; however, the literature is dominated by FCC structures due to the fact that this is the preferred crystal structure for most colloidal systems [3-6]. Naturally occurring colloidal crystals, or opals, have been the fascination of people for the unique optical properties, namely opalescence, associated with the structures. The opalescence results from their periodic nanostructure, where the periodicity is similar to the wavelength of light (**Figure 1**) [7, 8]. This periodic structure alters photon propagation, resulting in a photonic band structure that is superficially analogous to semiconductors and electronic band diagrams, as semiconductors have a periodicity of atoms similar to the wavelength of electrons [9]. Comparing the non-simplified band diagrams of the electronic bands of semiconductors to the photonic bands of colloidal crystals reinforces this comparison, shown in **Figure 2**. Structures with a photonic band gap over all directions are stated to contain a photonic band gap; typically colloidal crystals have a photonic gap in only one or two directions, commonly referred to as a stop band [7, 9, 10]. Importantly, this modulation of photon propagation is due to the optical properties of the colloids, namely the dielectric permittivity (and in special cases, the magnetic permeability), rather than the electronic properties of the atoms in semiconductors [11]. The dielectric permittivity and the magnetic permeability are commonly simplified to the refractive index of the colloids due to the relationship of

$$\boldsymbol{n = \sqrt{\epsilon_r \mu_r}} \qquad \textbf{1}$$

where the refractive index, *n*, is related to the relative permittivity, ϵ_r, and relative permeability, μ_r. At optical frequencies with typical dielectric materials (e.g., oxides), the relatively permeability, μ_r, is effectively 1 and can be ignored [12]. However, if the colloids interact with the magnetic field, e.g., magnetic domains of iron within the colloids, the permeability must be taken into consideration. While colloidal crystals can in principle be made from any colloid, naturally occurring opals consist mainly of silica colloids containing impurities of iron, aluminum, or titanium, and fabricated colloidal crystals are made of primarily silica, polystyrene, or poly(methyl methacrylate) colloids [8].

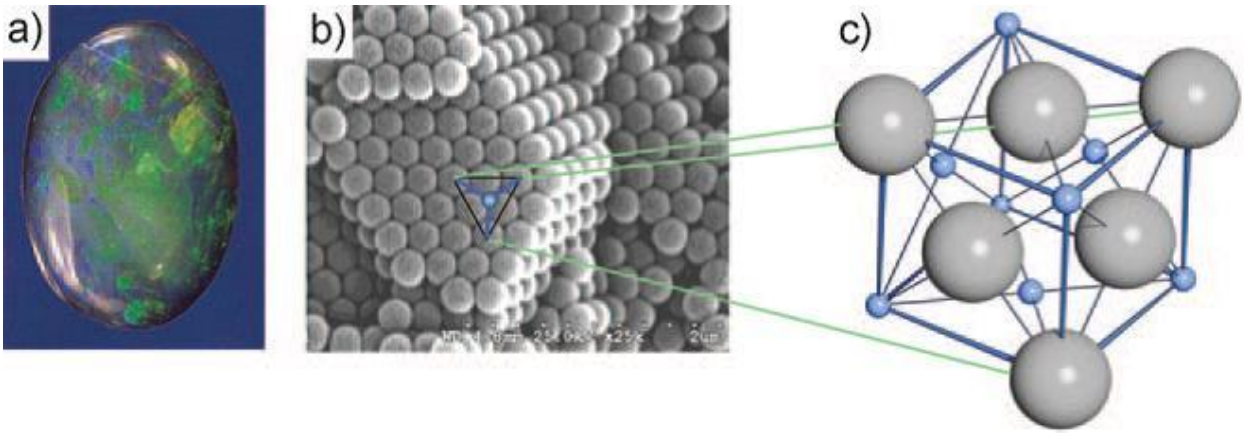

Figure 1. (a) Naturally occurring opal. (b) The periodic structure of the opal; light interacting with this structure results in the color observed. (c) The FCC structure present in this crystal. In this example, the colloidal particles are approximately 300 nm in diameter. Adopted from Reference [8].

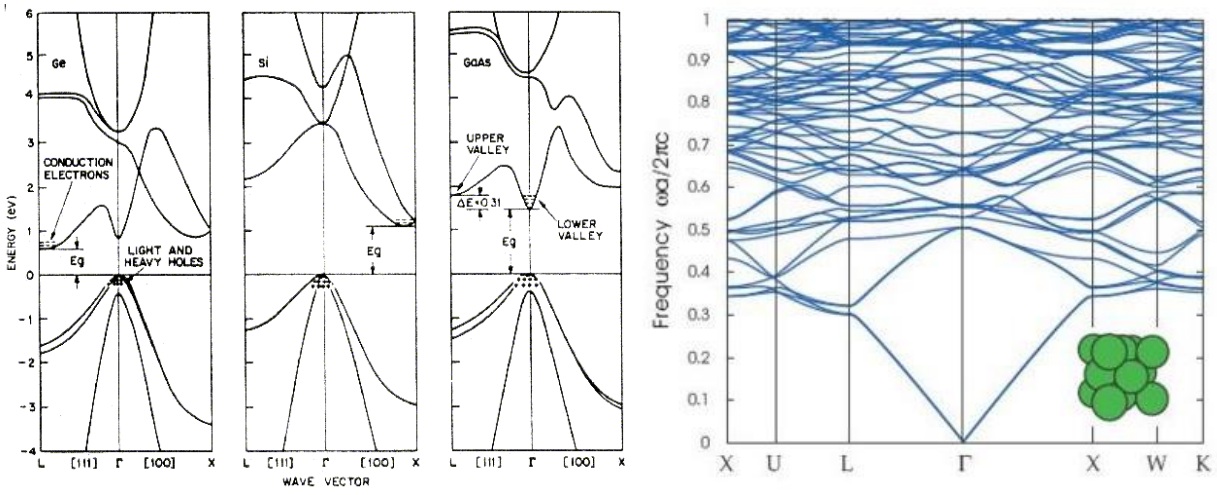

Figure 2. Left: Non-simplified electronic band diagrams of germanium (Ge), silicon (Si), and gallium arsenide (GaAs) showing energy (frequency) vs. wave vector (position), adapted from Reference [13]. Right: photonic band diagram of a colloidal crystal, showing frequency vs. position. There is no full photonic band gap; only stop band (i.e., band gap in one direction). Adopted from Reference [7].

In naturally occurring opals, between the silica colloids there is typically porous, water-containing silica; this porous silica provides mechanical integrity as well as changes the optical properties [8]. While colloidal crystals cannot have full photonic band gaps, regardless of the refractive index of the spheres, inverse opals, where the voids between the colloids are filled with a material and the colloids removed, can have a full photonic band gap if the refractive index of the infilled material is sufficiently high [9-11, 14, 15]. The optical properties of the inverse structure, as with the colloidal crystal template, are again determined by their dielectric properties, more conveniently expressed as the refractive index contrast of the materials [16]. Structures with a higher refractive index contrast (e.g., silicon-air structure compared to silica-air) have a larger photonic band gap, i.e., no allowed photonic states over a larger spectrum range

[7]. As such, many research groups have utilized colloidal crystals as templates, infilling the interstitial voids with a host of materials including high index materials of silicon [17], titania [18, 19], and zinc oxide [20], as well as lower refractive index materials of hydrogels [21] and carbon [22] for other interesting applications. In the case of naturally occurring opals, instead of a silica-air colloid crystal, with a refractive index contrast of ~0.55 (*n* of silica is ~1.55, air is 1), the refractive index contrast is now smaller, as the porous silica and water interstitial material's index is greater than 1. Indeed, by simply changing the amount of hydration in the interstitial, the optical properties can be influenced, shown in **Figure 3**. Additionally, the lower index contrast reduces scattering, changing the milky, opaque appearance of the opal to one that has a clearer structure where the color seems to come from deeper in the opal. This change in optical properties via an analyte is heavily utilized in sensor applications, both using a colloidal crystal [23-25] as well as an inverse opal replicate [20, 21].

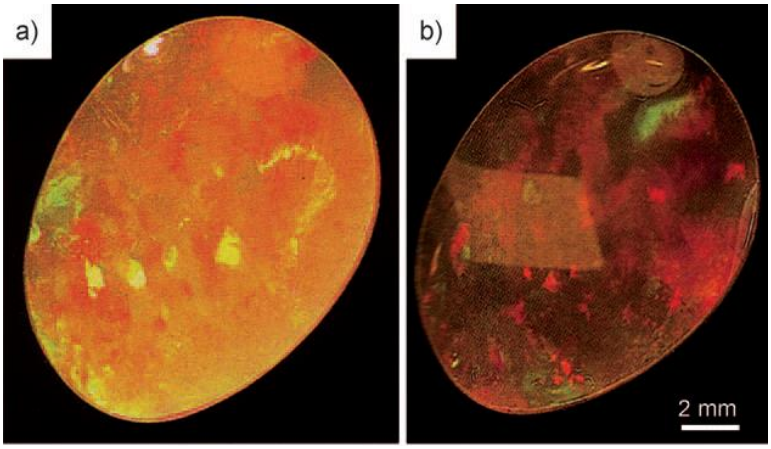

Figure 3. (a) Naturally occurring hydrophane opal in the dehydrated state. (b) Same opal in the hydrated state. Figure adapted from Reference [26].

1.2 Fabricating Colloidal Crystals

Colloidal crystals are advantageous in conducting research for two main reasons: their three-dimensional periodic structure alters photon properties in all directions, which is the most interesting in terms of photonic crystals and described in the previous section, and secondly, the relative ease of fabricating colloidal crystals through bottom-up self-assembly [8, 27-30]. Colloidal crystal fabrication can be broadly classified as a bottom-up assembly technique, in which colloids are driven to pack together through use of a variety of fields. These different methods are summarized in **Figure 4**; for discussion on each method, Marlow, et al., provides an excellent summary [8]. For this work, the flow-induced method of colloidal crystal fabrication was exclusively used.

Colloidal crystal fabrication begins with the individual colloids. As mentioned previously, most colloidal crystals are fabricated with silica, polystyrene, or poly(methyl methacrylate) spheres. This is due to one of the main requirements for a high-quality colloidal crystal: the colloids must be monodisperse. Increasing the colloidal size distribution creates packing defects, which disrupt the lattice similar to substitution atoms on the atomic scale. Experimentally, a size distribution of greater than 5% leads to numerous defects, with the resulting structure having little long-range order and inferior optical properties. Colloids of silica, polystyrene, and poly(methyl methacrylate) can be easily fabricated with low polydispersity and are available commercially [31, 32].

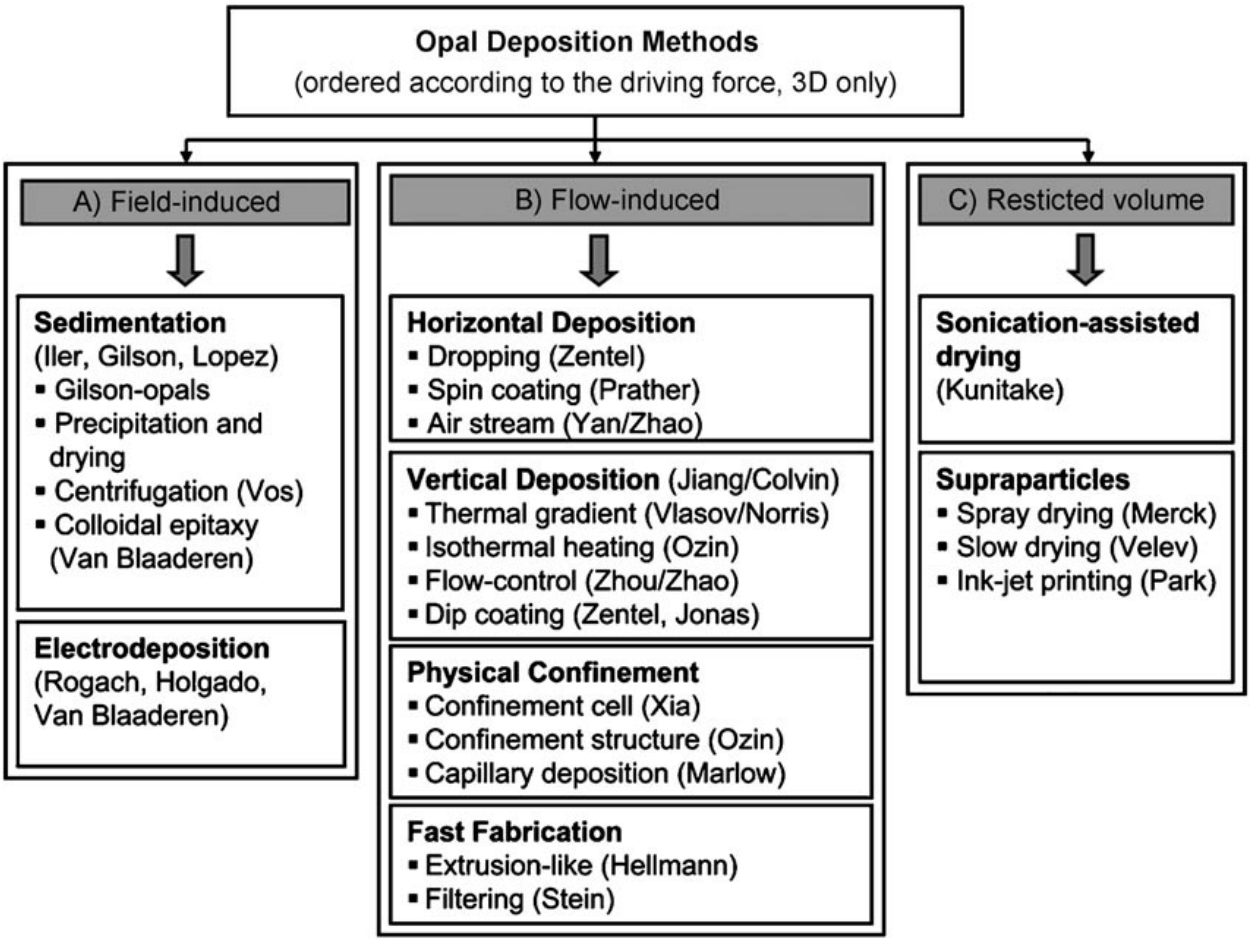

Figure 4. Colloidal crystal (opal) deposition methods, as summarized by Marlow, et al. Adopted from Reference [8].

While the exact mechanisms for colloidal crystal formation are not firmly established [2], experimental results provide some insight. A stable suspension of the colloids, with any excess surface contamination removed, is necessary for high-quality colloidal crystals; this suspension has been typically water- or ethanol-based. The suspension needs to be stable longer than the colloidal crystal fabrication; most high-quality crystals use suspensions that are stable for days or weeks. With polymeric colloids, this requirement is easily met; however, silica colloids tend to crash out of solution, especially when the colloid diameter becomes greater than 700 nm. These

larger silica colloids require unique deposition procedures to form a well-ordered colloidal crystal, with some recent success using dimethyl sulfoxide (DMSO) as the solvent [33].

This work utilized a hybrid horizontal-vertical deposition method. One of the easiest ways to create an opalescent film is to allow a colloidal suspension to dry on a flat substrate. The suspension is pinned at the circumference where the solvent evaporates the quickest [34]. Due to particle convection, and thus the flow-induced classification, the resulting film is thickest at the pinned contact line and thinnest in the center. Pinning contact lines and using a variety of suspensions have resulted in a number of unique arrays [35] with the particle convection well understood [36]. A modification of the horizontal deposition method utilizes spincoating; however, a successful ordered film requires precise control of numerous parameters, including the colloid concentration, spinning speed, and suspension viscosity [37].

Vertical deposition sets the substrate into the suspension vertically, as shown in **Figure 5**. There are several advantages gained when the substrate is placed vertically, chief among them the smaller amount of suspension needed and lower defect concentration. A key challenge in the horizontal deposition method is the sedimentation of the colloids: any colloid that crashes out of solution prior to packing into the close-pack structure results in a defect. With the vertical deposition method, any colloids unstable enough to sediment will instead deposit on the floor of the deposition vial, preserving the substrate and providing fewer defects in the resulting colloidal crystal. With vertical deposition relying on solvent evaporation, the rate of crystal formation was inherently slow, limiting the suspension to small colloids. Heating, mechanical agitation, and using ethanol as the solvent increases the evaporation rate and allows larger colloids to be used.

With vertical deposition, there is a thickness gradient the further down the substrate. Some groups have attempted pulling the substrate out of the suspension during drying to prevent this variation [38, 39]. The process utilized in this work places the suspension vial, along with a clean substrate, at approximately 30°, uses ethanol exclusively as the solvent, and is isothermally heated to an experimentally determined temperature. This conserves the colloids, requiring only tens of milligrams that can be reused, eliminates potential problems with water's high surface tension, and allows crystal formation of colloids with diameters of 500 nm. Due to the thickness variation, as the substrates were static during deposition, the highest quality areas were typically within 5 mm of the initial deposition line. Modifying this procedure could result in larger high-quality areas, but this was not necessary in the work presented here.

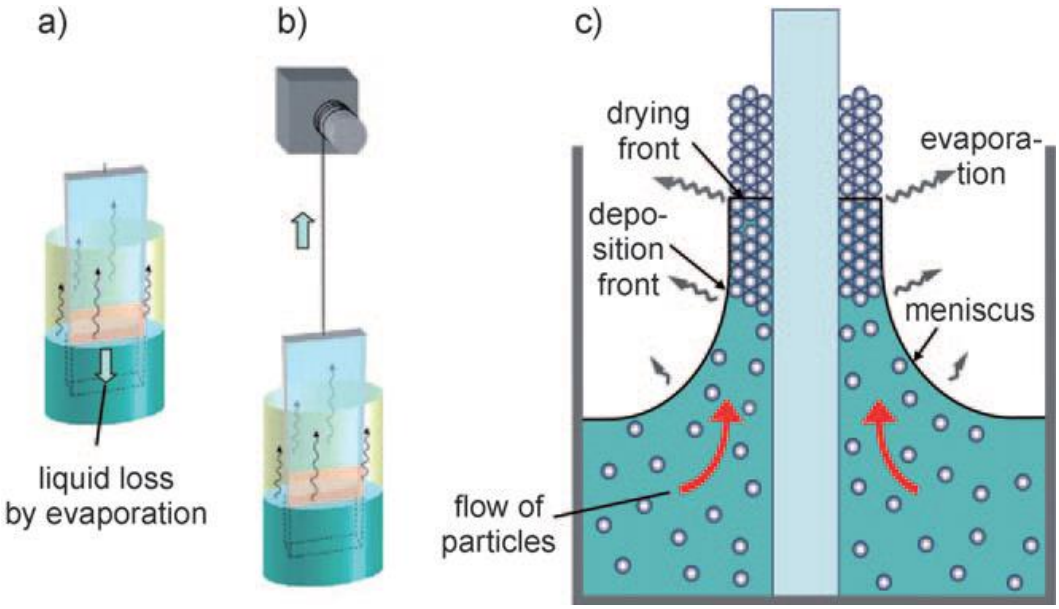

Figure 5. Vertical deposition of colloidal crystals: (a) stationary substrate, with the film depositing solely on solvent evaporation; (b) modified setup with the substrate slowly pulled from the suspension; (c) mechanism of colloidal crystal growth. Adopted from Reference [8].

While these experimental conditions can be tailored for high-quality colloidal crystal formation, the actual mechanisms are not fully understood. As mentioned previously, the convection of colloids is well understood [36] and drives the colloids to pack at the meniscus. However, a clear understanding of why the colloids pack in a closed-pack, FCC structure, instead of a hexagonal ABA packing or even a random glass, is still missing. One hypothesis is a solvent flow argument proposed by Norris, et al, depicted in **Figure 6** [2]. During colloidal crystal formation, solvent is driven through the packed colloids and evaporated (see Figure 5). The "clear niche" in Figure 6, one that does not have a colloid directly behind it, allows higher solvent flux and drives the colloid to pack in the FCC ABC packing. Additionally, colloids and the substrate must have a relatively strong and long-range repulsive force; otherwise, short-range attractive forces (van der Waals) will cause colloid aggregation and premature deposition on the substrate creating defects that disrupt the colloidal crystal. Self-assembly of high-quality colloidal crystals require colloids that are both monodisperse and form a stable suspension (typically accomplished by imparting them with a repulsive surface charge [8, 40]).

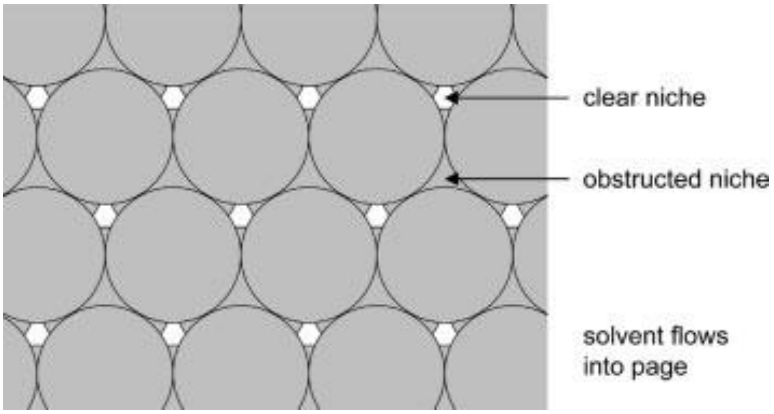

Figure 6. Proposed mechanism for flow-induced colloidal crystal formation. Adopted from Reference [2].

Modifying the experimental conditions of the colloidal deposition has resulted in a number of unique structures. Due to the colloidal crystal's and inverse opal's modification of photonic bands, work has progressed in using them for improving photovoltaic devices. As silicon cells can be made with high efficiency, most of the work has been focused on dye-sensitized solar cells (DSSC) [41-46]. In DSSC, the light is absorbed through a dye, typically ruthenium-based, which is excited from the ground state [47]. The excited electron is then transferred into the conduction band of a wide-band gap semiconductor, typically nanoparticles of titania, and transported to the back contact to be collected. The dye accepts an electron from the electrolyte, with the oxidized electrolyte reduced at the front contact. Due to the dye's optical absorption, the majority of the red part of the visible spectrum passes through the cell and is not utilized [44]. Incorporating a colloidal crystal into the cell would allow select wavelength to be reflected back, improving the absorption. Additionally, the porous structure of the colloidal crystal allows the electrolyte to regenerate the dye. A challenging part of using a colloidal crystal is the fabrication on the rough nanoparticle titania surface. By fabricating the colloidal crystal on a sacrificial substrate, followed by a polymeric infilling and etching, the colloidal crystal can be transferred to the titania with high fidelity (see **Figure 7**) [48]. Additionally, the colloidal crystal can be used as a template prior to transferring; templating with the colloidal crystal on the titania will fill the pores between the titania nanoparticles, preventing the electrolyte from reaching and regenerating the dye.

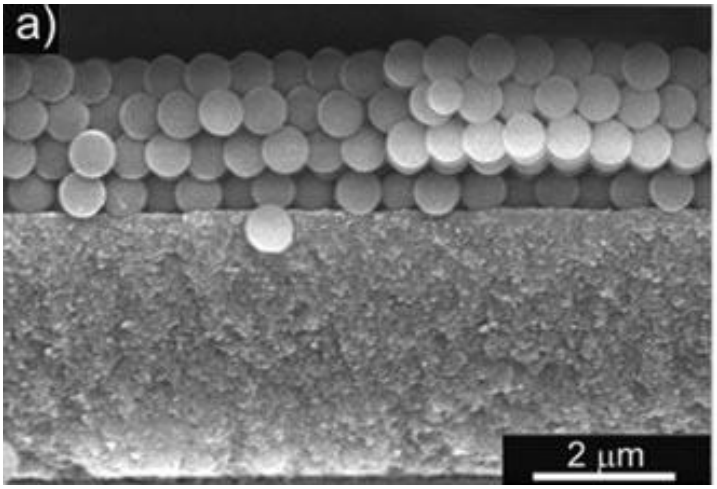

Figure 7. Silica colloidal crystal transferred onto a nanoparticle titania surface for DSSC testing. Adapted from Reference [48].

Another interesting development was realized by Finlayson, et al. [27]. In their work, a suspension of a core-shell polymeric colloid (polystyrene as the core and polyethylacrylate as the shell) was subjected to a shearing force as the PET substrates were drawn over a sharp, 90° edge. This induces long-range ordering of the colloidal crystal (greater than 10 cm^2). Through the addition of a small amount of carbon black powder (<0.1 wt%), they were able to obtain brilliant colors (**Figure 8**). The addition of carbon black absorbs the high frequency scattered light, drastically improving the contrast [49]. Their induced shear technique allows for large area films to be fabricated, opening the possibilities for further advancements.

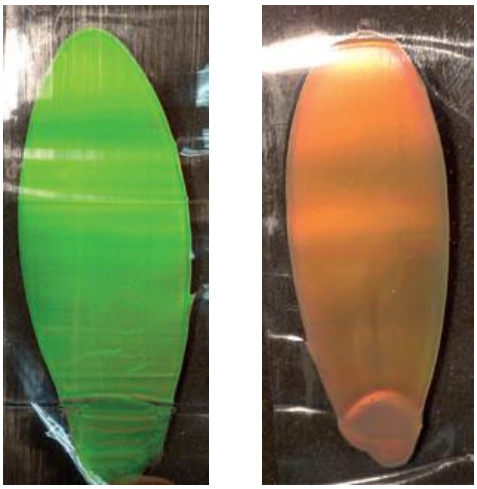

Figure 8. Polymeric core-shell colloidal crystals, with the addition of carbon black. Left: polystyrene core diameter of 215 nm; right: core diameter of 250 nm. Angle of viewing is normal incidence. Samples are approximately 6 cm long. Adapted from Reference [27].

1.3 Current Templating Strategies with Colloidal Crystals

The use of colloidal crystals as templates to impart periodic patterns into various materials has been broadly employed to create, for example, unique optoelectronic devices [48, 50], sensors [21, 51-54], and energy storage devices [55, 56]. The general motivation for templating is to utilize the colloidal crystals' interconnected 3D structure to define the 3D structure of a material that is inherently difficult to form into a highly regular 3D structure on its own. A single replication yields a structure that is an inverse of the colloidal template, and a double replication yields the original structure of the template. This process is only successful if the colloidal template can withstand the deposition conditions of the material to be templated and there exist conditions whereby the original template can be removed without damaging the templated material. Given that the most popular template, silica, can only be removed with hydrofluoric acid or strong base, chemicals that dissolve many materials, this can be challenging. Polymer

templates (e.g. polystyrene or poly(methyl methacrylate)) are easy to remove, but cannot withstand high-temperature deposition strategies, limiting their use [8]. Thermally stable colloids that could be removed under orthogonal conditions, i.e., conditions that do not damage the templated material, would allow currently inaccessible materials templating strategies. Additionally, if the templates contained additional desirable structural complexities (e.g. a high surface area) which are replicated in the templated material, additional applications may emerge; for example, dye sensitized solar cells require high-surface area electrodes [57], as do many other catalytic devices.

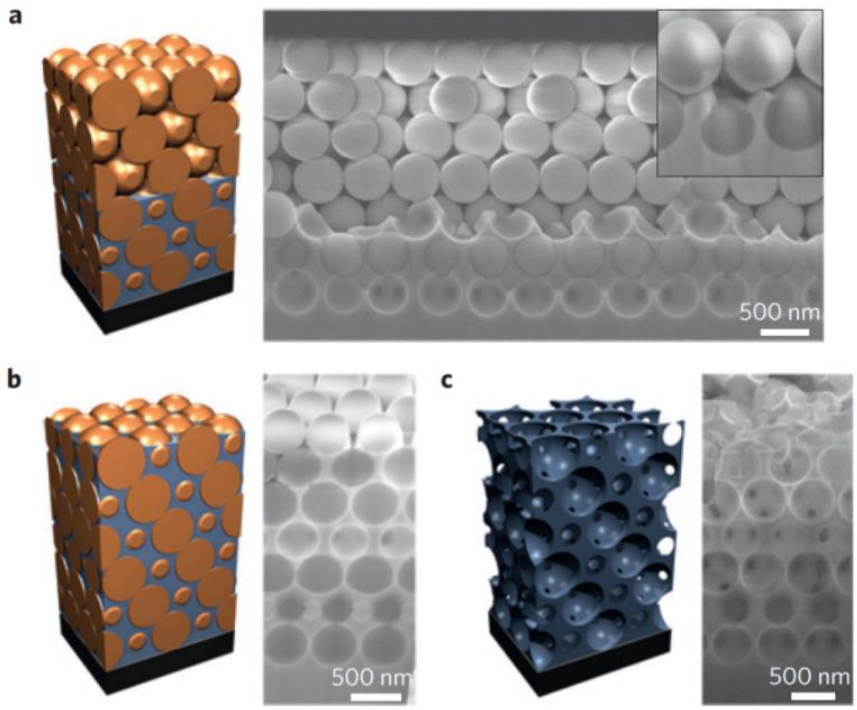

Figure 9. GaAs epitaxial growth through a silica colloidal crystal. (a) Schematic and scanning electron microscopy (SEM) image showing the bottom-up growth of the GaAs, where the GaAs has grown through 4 layers. (b) Schematic and SEM image of the GaAs-filled silica colloidal

crystal. (c) Schematic and SEM image of GaAs inverse opal once the silica template was removed. Adapted from Reference [50].

Two examples of templating in the Braun group have utilized the colloidal crystal for modifying the light emission of a templated emitter as well as a template for a three-dimensional metal electrode. Nelson, et al., was able to fabricate a silica colloidal crystal on a gallium arsenide (GaAs) substrate [50]. Through tailoring the deposition conditions, an epitaxial, single-crystal GaAs was grown from the bottom substrate (**Figure 9**). By incorporating an indium gallium arsenide (InGaAs) emitting layer, sandwiched between two GaAs layers, the change in emission could be realized. This templating took advantage of the GaAs' resistance to the hydrofluoric acid etching that removed the silica colloidal crystal. In the other example, Zhang, et al., was able to use a polystyrene colloidal crystal, on a tungsten foil, as the template [56, 58]. The final structure was a 3D porous nickel scaffold where active materials for batteries could be deposited (**Figure 10**). By annealing the polystyrene after colloidal assembly, the interconnects between the colloids increased and allowed larger voids after templating. Nickel was electrodeposited in the interstitials and the colloids removed via a solvent rinse. To further increase the void space, an electropolish was done prior to depositing the active materials. The final structure allowed for improved battery performance due to the 3D structure.

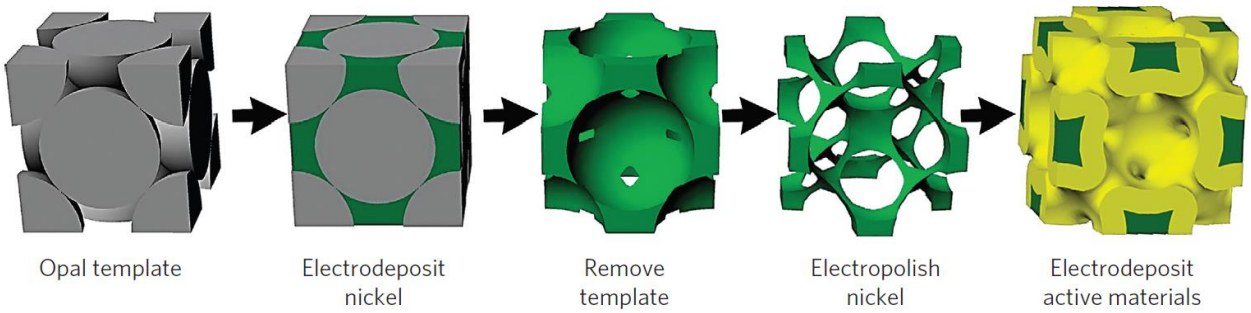

Figure 10. Schematic of templating process used by Zhang, et al., creating a 3D porous electrode. Adapted from Reference [56].

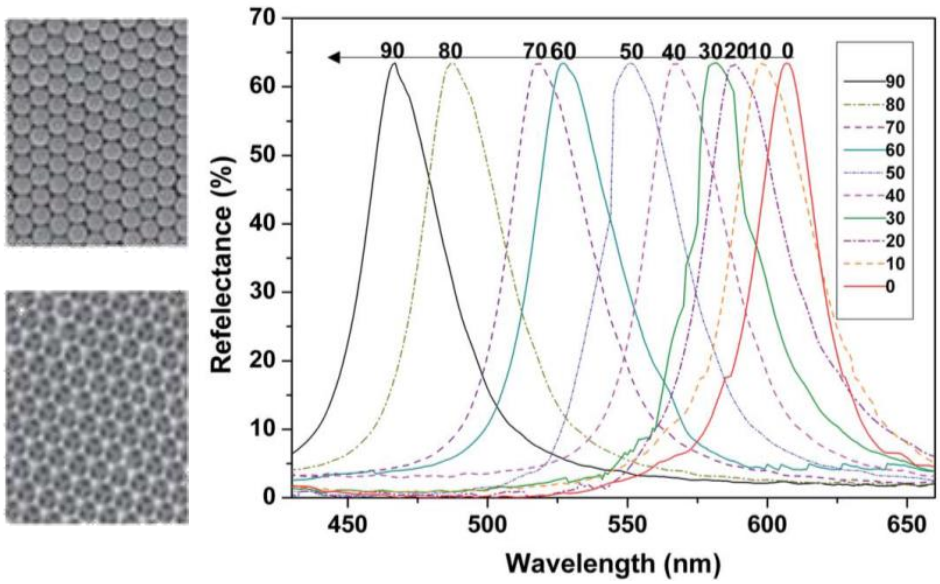

Figure 11. Top left: polystyrene colloidal crystal used as a template for PAM. Bottom left: Inverse opal of PAM after polystyrene removal. Right: optical response of the inverse PAM opal with varying ethanol concentrations in water. Adapted from Reference [52].

Another example capitalizing on the optical properties was conducted by Pan, et al. [52]. Intriguingly, the colloidal crystal utilized was again made from polystyrene colloids; however, the templating material was another polymer, namely polyacrylamide (PAM). To template the

PAM, PAM precursors were allowed to infiltrate the polystyrene colloidal crystal, after which the sample was placed in an oven for the monomers to polymerize, followed again by a solvent rinse to remove the polystyrene. The PAM inverse opal showed excellent optical properties, which were used to detect ethanol concentrations in an aqueous solution (**Figure 11**). By increasing the ethanol concentration, there is a blue-shift in the optical response. This is due to the PAM response to the solution: water will swell the cross-linked PAM but the alcohol will cause it to shrink. Increasing the alcohol content displaces the water, thus gradually shrinking the structure. As the optical response is dictated by the lattice spacing, this results in the blue-shift seen in Figure 11. Numerous groups have utilized inverse opals in sensor applications where the analyte of interest interacts with the structure [20, 21, 53, 59-61].

In summary, while colloidal crystals are an important research tool, they currently have strong limitations. The colloids used are typically limited to either silica or polystyrene, both of which have tradeoffs in their properties. Silica is stable at high temperatures; however, a harsh removal is needed, which limits the templated material. Polystyrene can be easily removed via a solvent rinse, but it can be utilized only where the temperature does not exceed 100 °C. Finally, the colloidal crystal template allows only for an inverse opal structure, limiting the potential applications.

1.4 Porous Carbon

Porous carbon is broadly utilized both for fundamental studies and large-scale commercial applications, including water purification, ion exchange [62], catalysis [63], conventional battery electrodes [64], emerging battery electrode designs [65], capacitor electrodes [55], and as a

polymer filler. The incorporation of small amounts of carbon-black into polymer-based colloidal crystals has resulted in brilliant colors by absorbing the scattered light, as shown previously [27]. An interesting study was done to make a carbon inverse opal using a silica colloidal crystal as a template, as reported by Isshiki, et al. [55]. In this, furfuryl alcohol was infiltrated into the silica colloidal crystal, polymerized, and carbonized (**Figure 12**). After etching the silica template, the inverse carbon opal was tested as a capacitor, showing that the higher surface area carbon increases the specific capacity.

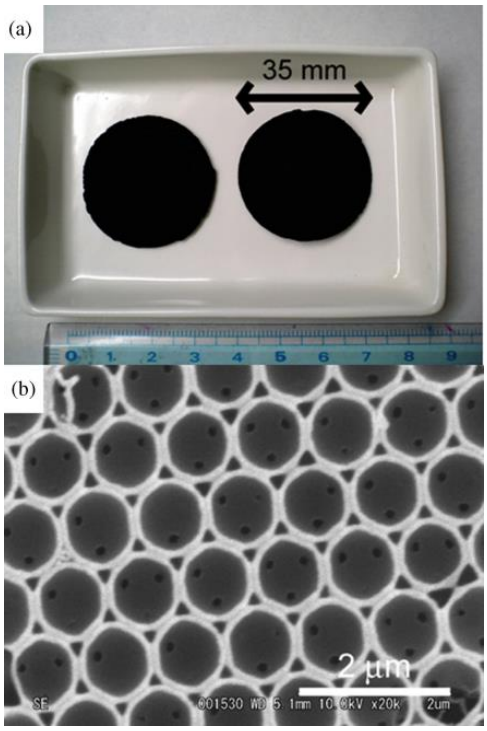

Figure 12. Inverse carbon opal fabricated from a silica colloidal crystal template. Adopted from Reference [50].

While carbon spheres [66-71] and inverse opals [22, 55, 72] have been fabricated, carbon colloidal crystals have been realized only through Chemical Vapor Deposition (CVD) on a

sacrificial, mesoporous silica colloidal crystal [73]. While this creates the colloidal crystal structure, it would be much more attractive to utilize the self-assembly of carbon colloids, which would eliminate the CVD and etching steps as well as enable large crack-free structures. Due to carbon's high thermal stability (>1000 °C in inert environment) [74], a self-assembled carbon colloidal crystal would be an ideal template for materials that can be grown only at high temperature. Additionally, carbon can be removed by a simple oxidation step, eliminating the HF etching step required to remove silica.

1.5 Mesoporous Silica and Carbon Spheres

The majority of this work is an extension from and performed in collaboration with Dr. Kazuhisa Yano, Dr. Narihito Tatsuda, and coworkers from Toyota Research and Development. In 2003 and 2004, Yano and coworkers started reporting success on making monodisperse silica spheres having mesopores throughout the structure [75, 76]. The mesopores were created during the silica colloid growth by adding in a surfactant, typically an alkyltrimethylammonium bromide or chloride. By changing the alkyl length, e.g., a chain of 8 carbons compared to 14 carbons, the diameter of the mesopores can be tailored: a longer alkyl chain resulted in a larger pore diameter. These spheres are characterized through nitrogen adsorption measurements to determine the mesoporous properties. Infilling the silica with platinum allows for direct observation of the pores through transmission electron microscopy, shown in **Figure 13**.

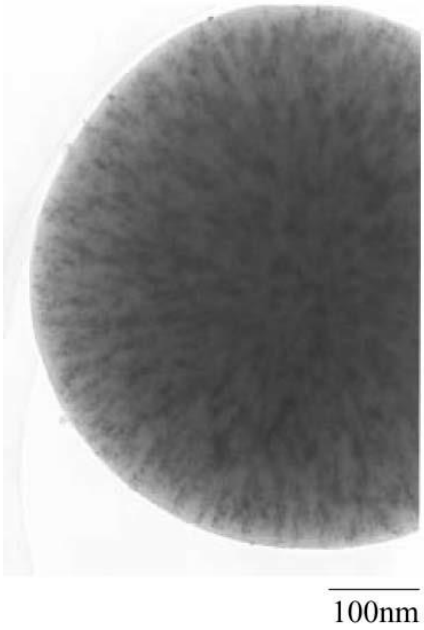

Figure 13. Transmission electron micrograph of a platinum infiltrated mesoporous silica sphere. Dark areas in the sphere correspond to the infiltrated platinum. Adopted from Reference [75].

These monodispersed mesoporous silica spheres were then able to be utilized as a template for monodispersed starburst carbon spheres (MSCS) [77]. Furfuryl alcohol is infiltrated into the silica mesopores, polymerized, carbonized, with the silica finally removed via a hydrofluoric acid etch. The resulting carbon colloids have "spokes" that are inverse replicates of the silica mesopores; the diameter of the carbon colloids is slightly less than the template due to volume restriction during polymerization and carbonization. A transmission electron micrograph can be seen in **Figure 14**. The diameter of the "spokes" can be tailored via the surfactant used during silica colloid growth; tailoring the mesoporous nature of the MSCS is more difficult due to the templating process: the MSCS mesopores were silica in the original template. Yano and coworkers were not able to utilize the MSCS in a self-assembled colloidal crystal. However, they

were able to create a MSCS colloidal crystal through the combination of bottom-up self-assembly of the mesoporous silica spheres and converting them to the MSCS through the established templating route.

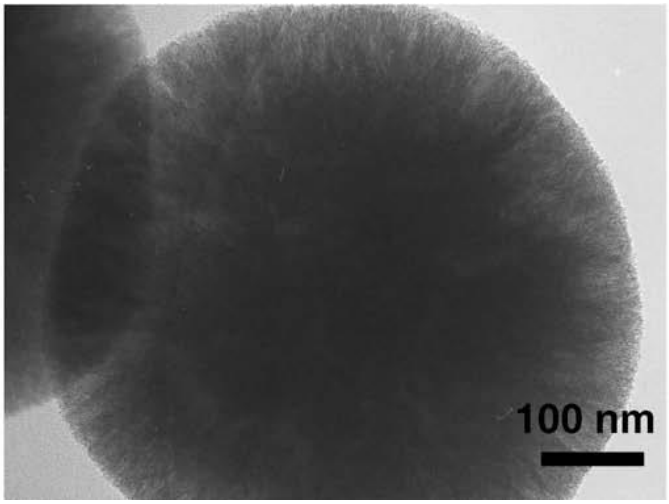

Figure 14. Transmission electron micrograph of the MSCS. Adopted from Reference [77].

CHAPTER 2

BRILLOUIN LIGHT SCATTERING IN SILICON INVERSE OPALS

This chapter describes work done using non-porous silica colloids for Brillouin Light Scattering experiments. Silica colloids were fabricated into a colloid crystal and used as a template for silicon deposition via CVD. Utilizing small (less than 400 nm diameter) colloids, the resulting silicon structure has periodicity on the wavelength of visible light, allowing strong interactions. By scattering light off the structure, the phononic band structure can be investigated. This work was done in collaboration with Dr. Huihui Pan and Prof. Jay Bass, who conducted the measurements on the samples provided.

2.1 Brillouin Light Scattering

Brillouin Light Scattering (BLS) occurs when monochromatic light is scattered and reflected by an acoustic wave. As photons travel several orders of magnitude faster than phonons, the acoustic wave can be described as quasi-stationary [78]. This acoustic wave, which shifts atoms slightly as it propagates, changes the density of the material in a periodic fashion and behaves as a one-dimensional Bragg stack, sharply reflecting photons that meet the Bragg conditions. To date, BLS studies on colloidal crystals have been scant [79-82], even as they show interesting acoustic behaviors. Similar to electronic and photonic behavior in low-dimensional systems, acoustic waves in a silica colloidal crystal have distinct propagation modes where the continuous energy landscape changes to discrete bands [83]. By having a periodic structure, the photonic crystal inverse opal has the potential of unique responses due to the photon and phonon confinements. To investigate Brillouin Light Scattering, an inverse opal of silicon using small diameter colloids is desired. By having small diameter colloids as the template, the periodicity of

the silicon inverse opal will be on the order of the wavelength of visible light. Thus, a strong reflectance peak can be observed, both in the colloidal crystal sample as well as the inverse opal, when the incident light is normal to the sample surface; the colloidal crystal's optical response is due to the stop band while the inverse opal's response is due to a photonic band gap. By rotating the incident light off normal, the different photonic bands can be accessed. With a generated acoustic wave, these bands can be further influenced due to the effective refractive index modulation due to the compression and expansion of lattice constants.

2.2 Silica Colloidal Crystal Fabrication

Due to the template inversion into silicon, the process dictates that silica colloids be arranged into colloidal crystals. While silica colloidal crystals have been fabricated in the Braun group, most have utilized silica colloids with diameters greater than 400 nm [17, 84-86]; below this, the assembled arrays have had numerous defects (e.g., vacancies and general colloidal disorder) that prevent further utilization, especially in optical studies. For the BLS studies, however, it is required that the colloidal crystal have the smaller periodicity to allow probing of the photonic bands. Also required is the use of substrates, ideally transparent, that can withstand the silicon crystallization conditions of heating to 1000 °C. Quartz is an obvious choice; however, assembly of silica on quartz has also been problematic. Silicon substrates can also be used; the optical measurements could be obtained through reflection instead of transmission. A silicon substrate, however, does allow the complete removal of the silica colloidal crystal via HF etching, which a quartz substrate does not allow.

Initially, 400 nm diameter silica colloids were synthesized using the Stöber method [31] (**Figure 15)**; after calcination at 550 °C for 6 hr to remove surfactants and prevent cracking in the assembled array, the colloid diameter reduced to approximately 380 nm. Fresh quartz slides were cut to size, blown with dry air, and then cleaned in piranha solution (3:1 volume ratio of sulfuric acid (H_2SO_4) to hydrogen peroxide (H_2O_2); *Caution: extremely exothermic and reactive*) for 1 hr. After cleaning, the quartz substrates were thoroughly rinsed in Millipore water, followed by an ethanol rinse and blown dry. The substrates were then placed at a 20° angle in a scintillation vial containing 2, 3, or 4 wt% silica in ethanol, all within an incubator at a constant temperature between 32 and 40 °C. Experimentally, it was determined that the best colloidal crystals, i.e., with the best optical properties, were obtained using the 3 and 4 wt% silica ethanolic solutions at an incubation temperature of 32 °C. Comparing with larger diameter silica colloids, the observed trend for high-quality colloidal crystals requires a lower temperature when using a smaller silica colloid, assuming other parameters are held constant (e.g., colloid solution concentration). Presumably, the larger silica colloids sediment quicker, requiring the faster evaporation of the solvent for colloidal assembly.

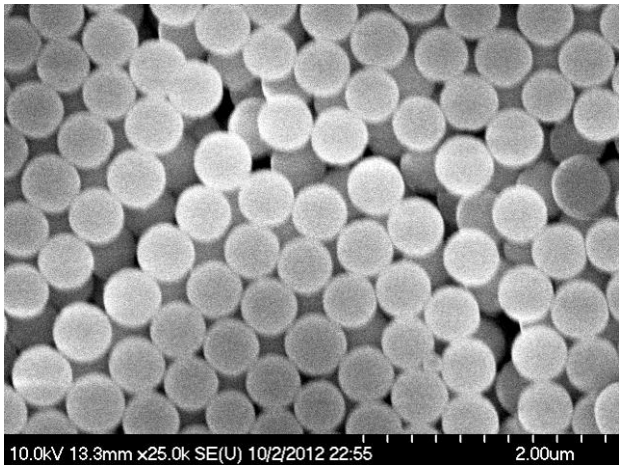

Figure 15. SEM of precalcined silica colloids used for colloidal crystal fabrication. Colloid diameter is approximately 400 nm.

A silica colloidal crystal was then fabricated on the quartz substrates. The silica colloidal crystal, consisting of 8 layers of silica colloids, showed reasonable opalescence; optical reflectance was measured, shown in **Figure 16**, with a main peak of 44% at 937 nm. Increasing the number of colloid layers would increase the magnitude of the reflectance peak, assuming the resulting layers still assembled with little to no defects. Si CVD was then conducted, depositing approximately 30 nm (3hr, 350 °C, ~50 mbar disilane). After CVD, the sample had a brownish appearance due to the amorphous silicon. Crystallization of the silicon was attempted by heating to 1000 °C for 10 hr. Unfortunately, oxygen was present during the crystallization, due to gas

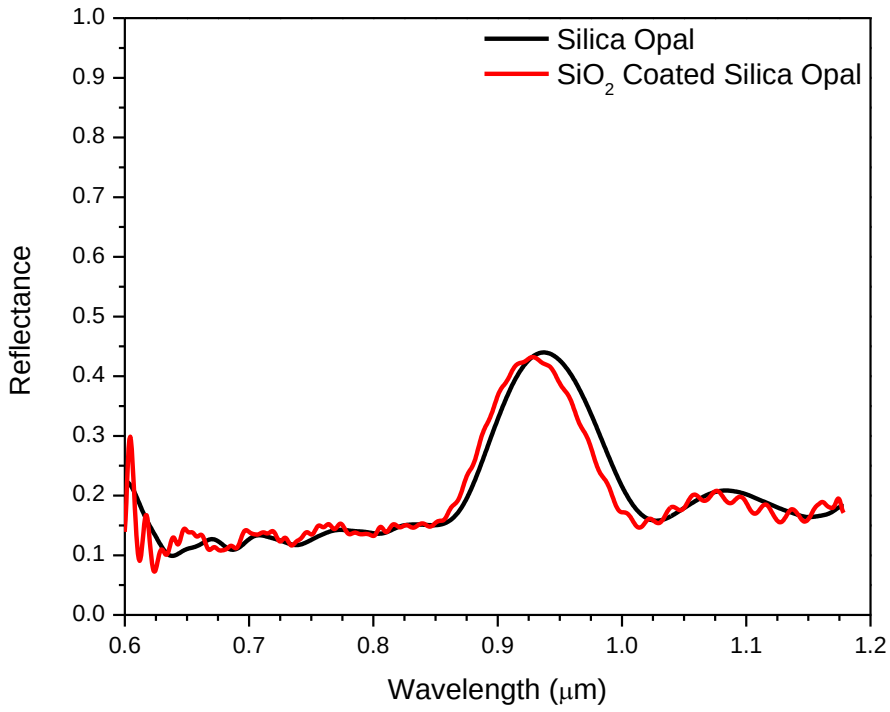

Figure 16. Optical reflectance measurements on silica colloidal crystal (black) and colloidal crystal after Si CVD with subsequent oxidation (red). The main peak blue shifted slightly from 937 nm (44%) to 928 nm (43%) after the silicon oxidation.

impurity, a leak, or an incomplete purge, and the silicon oxidized to silica. The colloidal crystal remained opalescent, with the new reflectance data also shown in Figure 16. Interestingly, the main reflection peak blue shifted slightly to 928 nm, with a reflectance of 43%. SEM micrographs were taken of the oxidized silicon colloidal crystal (**Figure 17**). "Dots" were evident on the surface of the colloids, as well as nano-ribbons on the top surface. These are probably due to a poor CVD run and the oxidation process.

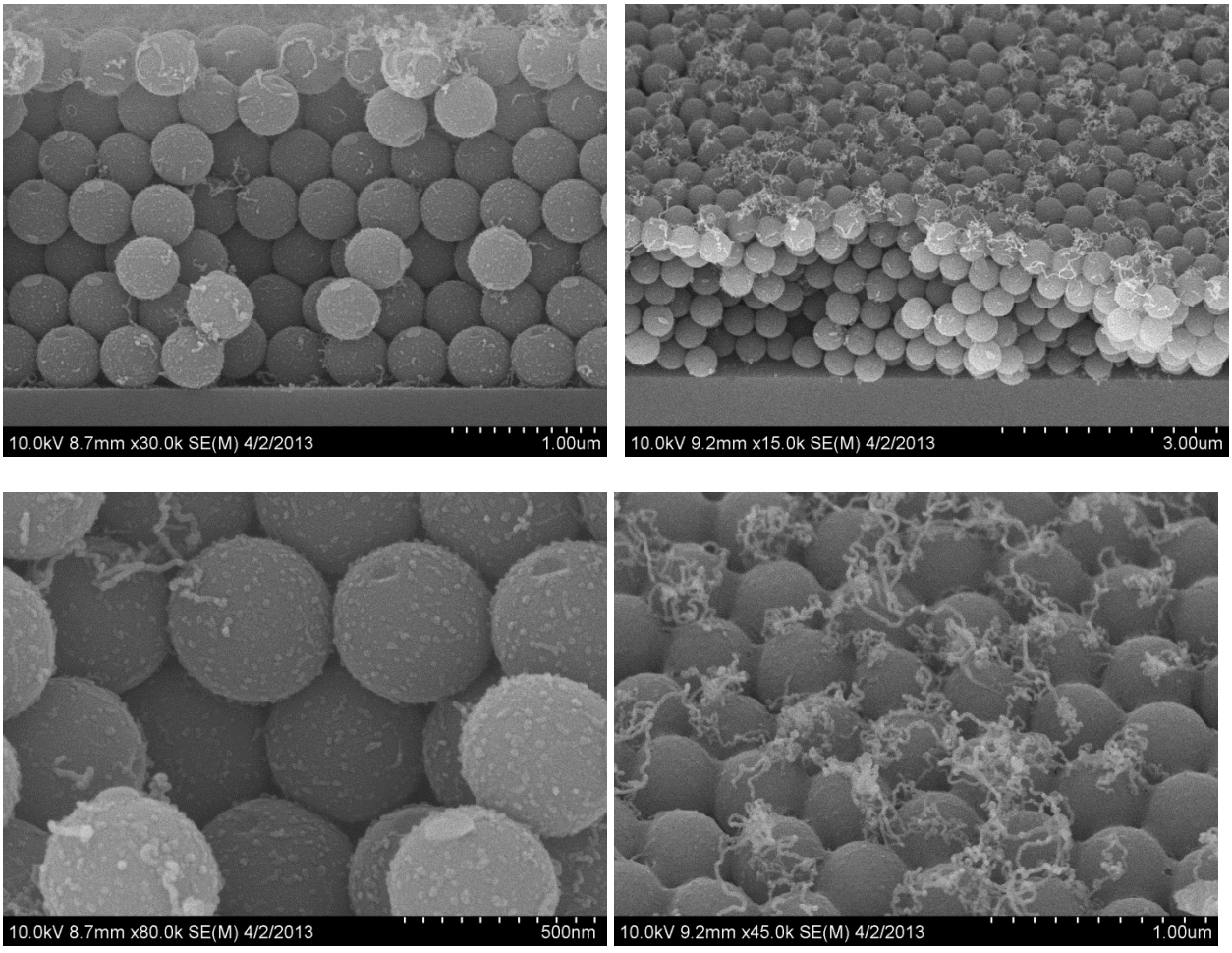

Figure 17. SEM micrographs after the subsequent oxidation of the silicon CVD. Left: cross-section views showing "dots" on the colloids. Right: 45° oblique view on the colloidal crystal showing nano-ribbons on the top-surface.

By improving the silicon crystallization process, new samples were fabricated without silicon oxidation. BLS experiments were performed on these samples; however, there was little to no response. It is believe that the lattice spacing provided by the 380 nm diameter silica was too large to effectively modulate the optical response in the detection regime. To improve the response, 270 nm diameter calcined silica colloids were synthesized and assembled into a colloidal crystal. These show excellent optical properties on quartz (**Figure 18**), with a main reflectance peak of 59% at 587 nm. Upon silicon CVD, two samples cracked and delaminated. This is assumed to be due to the excess silicon deposition. The pinch-off point for the colloidal crystals is 23 nm; the amount deposited was ~35 nm. Two new colloidal crystals were grown on silicon, with their reflectance measurements in **Figure 19**. After decreasing amount of silicon deposited during CVD, the colloidal crystal remained intact.

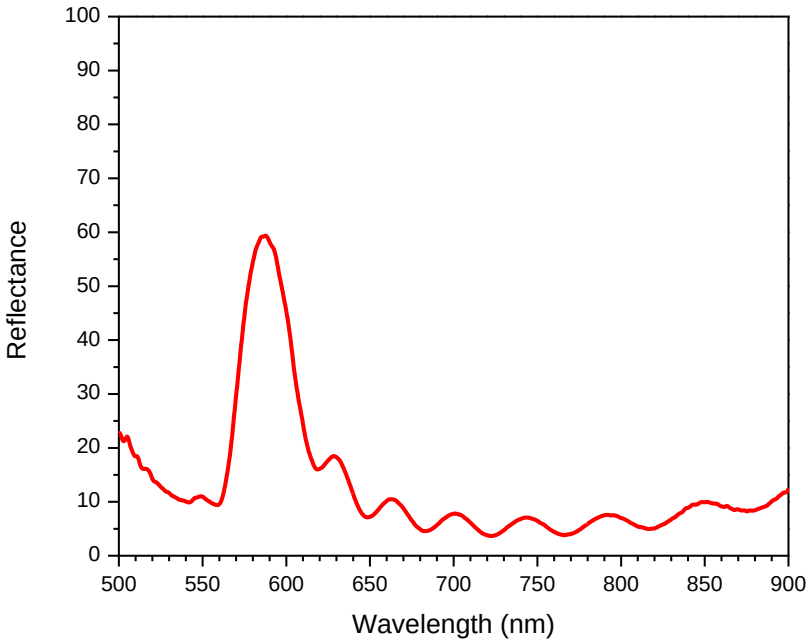

Figure 18. Optical response from a 270 nm diameter calcined silica colloidal crystal grown on quartz. The main reflection peak is at 587 nm and 59%.

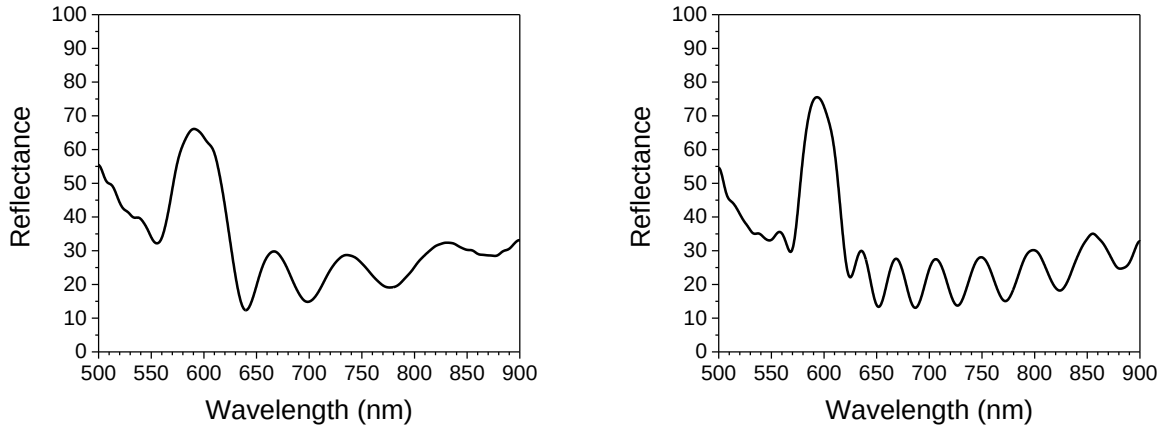

Figure 19. Silica colloidal crystals grown on silicon substrates. Left: 4 wt% silica having a reflection peak of 66.1% at 590 nm. Right: 4.5 wt% silica having a reflection peak of 75.5% at 593 nm.

After crystallizing at 1000°C, the samples grown on silicon were subjected to a masked RIE to expose the silica template, which was subjected to a hydrofluoric (HF) acid etch; however, it was determined that the hydrofluoric acid etching did not completely remove the silica template. After repeating the RIE and etching process, reflectance spectra were taken of both quartz and the etched silicon samples (**Figure 20**). After the HF etching, the silicon samples did not show the desired reflectance peak at ~770 nm, indicating the RIE or HF etch damaged the samples, confirmed by SEM in **Figure 21**. A new etching solution of 5% HF in ethanol was made to cleanly etch the silica template, preventing subsequent RIE treatments that damage the sample.

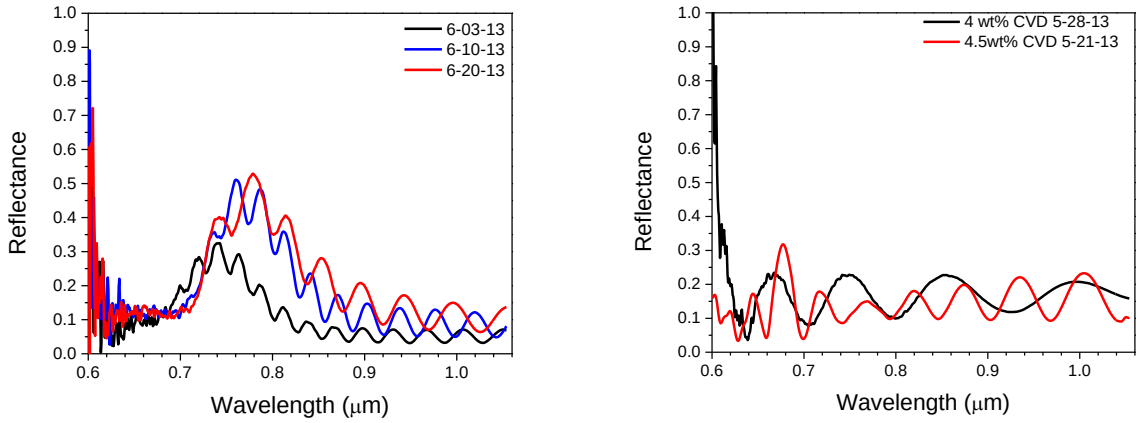

Figure 20. Reflectance spectra of silicon-coated silica on quartz (left) and silicon inverse opal on silicon (right).

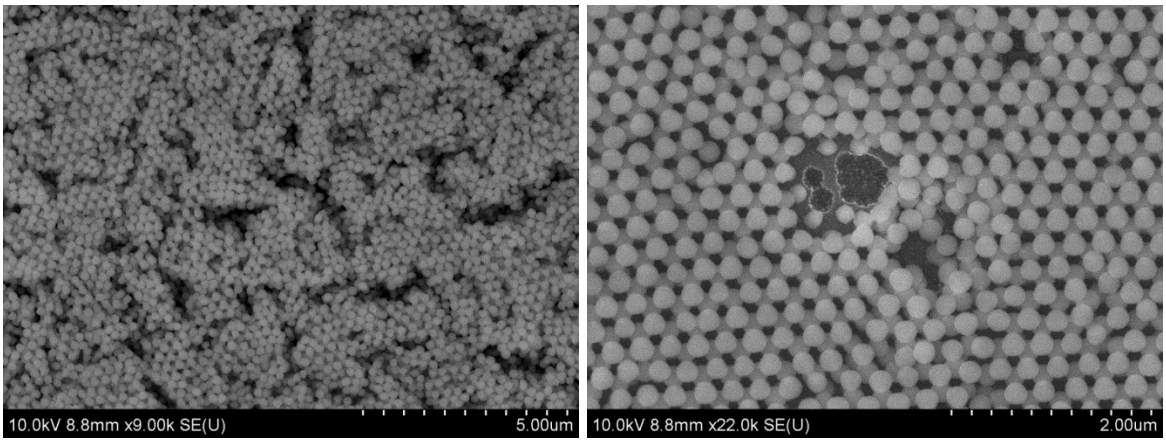

Figure 21. SEM of BLS sample, top surface after RIE and HF etching.

Through a strict, clean process, two sets of samples were created using 270 nm diameter silica colloidal crystals. The first was fabricated on quartz substrates, followed by silicon CVD; the second has a silicon substrate with, after silicon CVD, the silica template removed via hydrofluoric acid. Both sets were subjected to silicon crystallization at 1000 °C for 10 hr under argon gas, with a 2 hr purge prior to heating, after which the silicon substrate sample set underwent the RIE and HF etching process. The quartz substrate samples have excellent optical

properties and are shown in **Figure 22**. The different spectra are from different spots on the same sample, all showing a reflectance peak around 740 nm with a magnitude between 63% and 67%. The silicon substrate samples are shown in **Figure 23**, along with a quartz substrate sample as a comparison. To remove the silica template after silicon crystallization, an RIE etch was conducted to open the top surface coated with silicon: 20 sccm SF_6 and 20 sccm O_2 were flowed into the chamber, which was held at 50 mTorr; power was set to 70 W. One sample was subjected to a 2 min etch (black and red spectra in Figure 23) while the other was subjected to only 1 min. To prevent complete delamination during HF etching, a Kapton film was used as an etch mask, having a 2 x 5 mm window to expose the silicon-coated colloidal crystal. After etching, optical measurement in the center of the window had a lower reflectance magnitude than measurements off-center, i.e., where the silicon was protected by the Kapton film (black vs. red spectra in Figure 23).

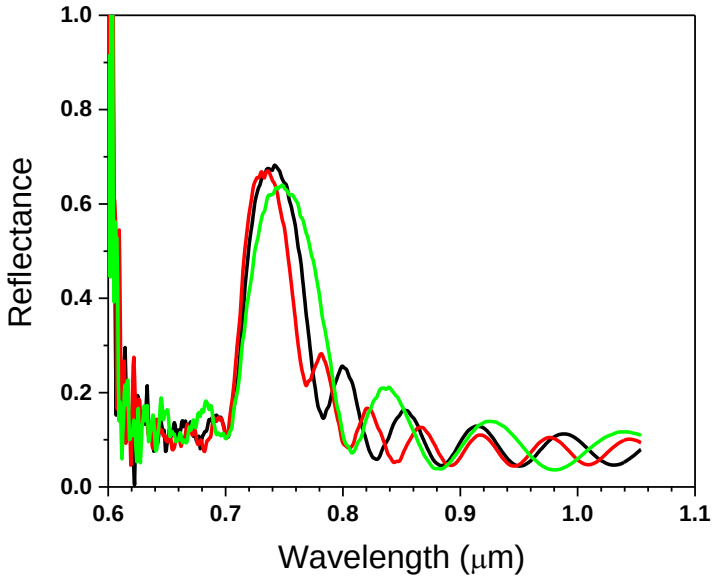

Figure 22. Optical reflection of Si CVD coated 270 nm diameter silica colloidal crystal on quartz.

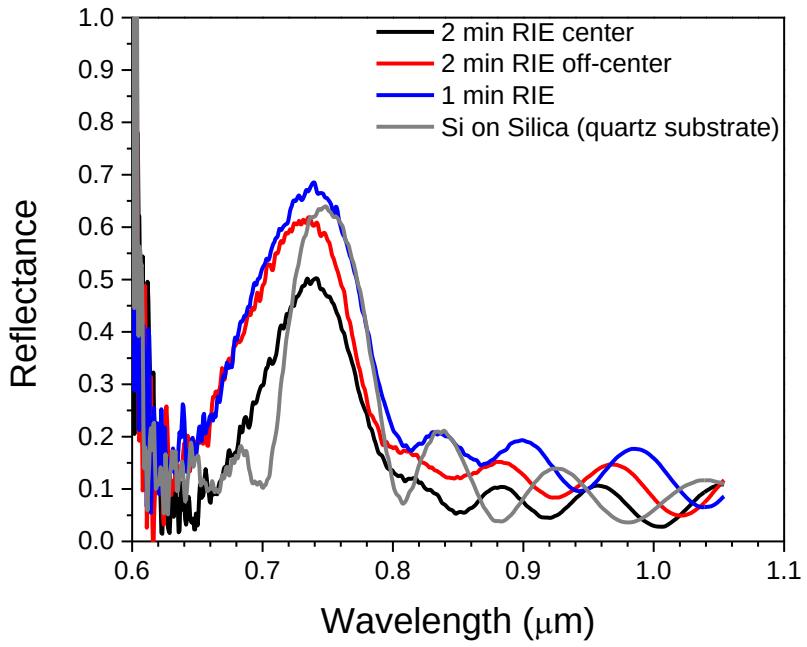

Figure 23. Optical data on silicon CVD BLS samples. Two samples were subjected to a 1 min or 2 min RIE to open the silicon overlayer prior to HF etching of the silica template. The 2 min RIE off-center spectrum is data collected where there is still a silicon overlayer, but within 2 mm of the opening so the silica could be etched out. For reference, a silicon-coated silica colloidal crystal, fabricated on quartz, is also shown. All silicon was successfully crystallized at 1000 °C for 10 hr.

2.3 BLS Measurements

BLS measurements were conducted on the samples using a backscattered system. A 514.5 nm diode-pump laser was shown incident on the sample with the backscattered light collected and analyzed, i.e., the laser and backscattered light traveled in the same optical path. The sample was placed at varying angles to the beam, between 12.5° and 62.5°; placing the sample at an angle less than 12.5° resulted in signal saturation due to the strong backscattering of the samples. Due

to conservation of momentum, any deviation of the wave vector from the scattered photon compared to the incident photon must be accounted by a phonon wave vector, namely

$$\boldsymbol{k_s = k_i \pm q} \quad \textbf{2}$$

where q is the phonon wave vector, k_s and k_i are the scattered and incident photon wave vectors, respectively [87]. The positive sign refers to the anti-Stokes event where a phonon is annihilated, whereas the negative sign refers to the Stokes event and the creation of a phonon [78]. Due to the phonon having several orders of magnitude less energy than the incident and scattered light, one can approximate the incident, k_i, and scattered, k_s, wave vectors to be the same, with the only variation due to the scattering angle. For the semiconductor samples, BLS investigates the propagating surface acoustic waves, and, for the 180° backscattered setup utilized, the surface phonon wave vector q_s can be determined by

$$\boldsymbol{q_s = \pm 2k \sin\theta = \pm \frac{4\pi}{\lambda_0} \sin\theta} \quad \textbf{3}$$

where k is the photon wave vector, θ is the angle between sample normal and the optical path, and λ_0 is the wavelength of the laser [78]. The frequency of the scattered phonons can be obtained through the recording of the Brillouin spectrum. Additionally, by changing the incident angle, the dispersion of the surface acoustic waves can be mapped.

A representative recorded BLS spectrum is shown in **Figure 24**; this spectrum was collected with the sample tilted at 37.5° to the incident photons. Very unusual is the asymmetric Stokes and anti-Stokes intensities, and these cannot yet be explained. However, the peaks can be easily extracted and plotted for different incident angles (i.e., phonon wave vectors), shown in **Figure 25**. No clear phononic band structures can be seen. This could be due to strong photon

resonances in the silica colloids, a symptom of the non-symmetric results, or simply that this system does not alter the phononic landscape.

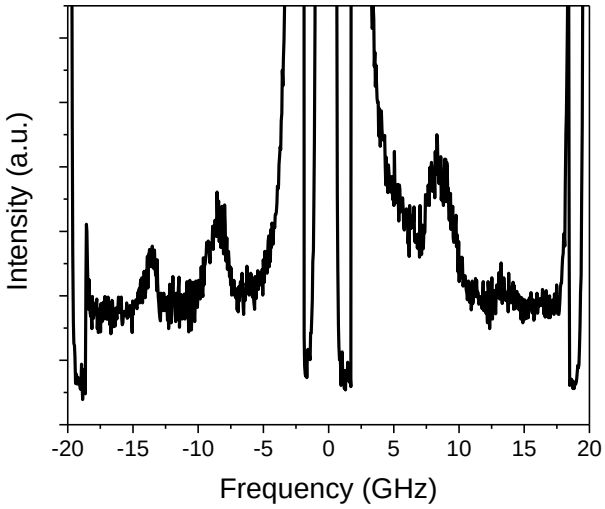

Figure 24. BLS data taken at a sample angle of 37.5° of the quartz substrate sample.

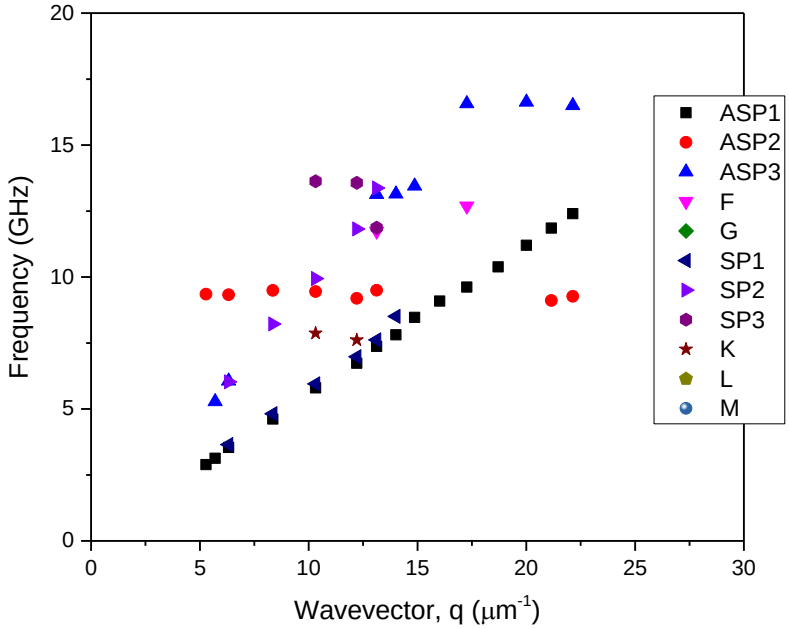

Figure 25. Dispersion relation between the phonon frequencies, extracted from the BLS spectra, and the phonon wave vector. ASP 1, 2, & 3 are the peak positions in the anti-Stokes region of the BLS spectrum; SP 1, 2, & 3 are from the Stokes region. Single letters indicate a unique peak that appeared in one or more measurements but could not be found in all.

2.4 Conclusions

Through varying the experimental conditions, silica colloidal crystals could be successfully fabricated on quartz and silicon substrates using colloids less than 300 nm in diameter. Additionally, by tailoring the silicon CVD reaction, the interstitial voids could be filled without significant over-deposition. Careful processing allowed the silica template, on the silicon substrate, to be removed via HF etching after a brief RIE to open the top silicon shell. These samples showed excellent optical properties and were given to collaborators for BLS measurements. However, the BLS spectra showed unusual behavior in that the Stokes and anti-

Stokes were not symmetrical, with no clear explanation. The dispersion relationship between the phonon frequencies and wave vectors did not show any phononic band structure, which may be due to the unusual spectra obtained.

CHAPTER 3

UTILIZING MESOPOROUS SILICA TEMPLATES:

PT LOADED PHOTONIC CRYSTAL AND HEAT TRANSPORT IN TEMPLATED SI

Two templating examples are presented in this chapter utilizing mesoporous silica. The first fabricates a colloidal crystal with the mesoporous silica spheres, followed by platinum deposition via atomic layer deposition (ALD). The second example shows preliminary work on thermal transport studies of silicon deposited in the mesopores. The thermal transport study originally used the mesoporous silica colloidal crystal; however, the template was changed to a mesoporous silica film for ease of sample measurements.

3.1 Mesoporous Silica for Pt template

Mesoporous silica spheres were fabricated into a colloidal crystal and used successfully as a template for platinum ALD; a Focused Ion Beam (FIB) cross-section is shown in **Figure 26**. The large crack near the substrate is presumably due to thermal expansion mismatch between the silica colloidal crystal and the substrate during ALD, as the deposition temperature is 270 °C. Due to the atomic number contrast, the platinum appears bright in the SEM image, infiltrating the silica colloids quite significantly. After creating a thinner colloidal crystal, the mesoporous silica colloidal crystal proved to be an effective template for platinum ALD. **Figure 27** shows the mesoporous platinum "shell" that is created after silica removal via hydrofluoric acid etching. The platinum infiltrated approximately 115 nm in the 622 nm diameter silica colloids, which had a pore diameter of 2.27 nm; deeper infiltration could be possible if larger mesopores were used. While this is a unique structure, mesoporous platinum has already been shown in literature to have catalytic activity [88, 89], so no further tests were performed.

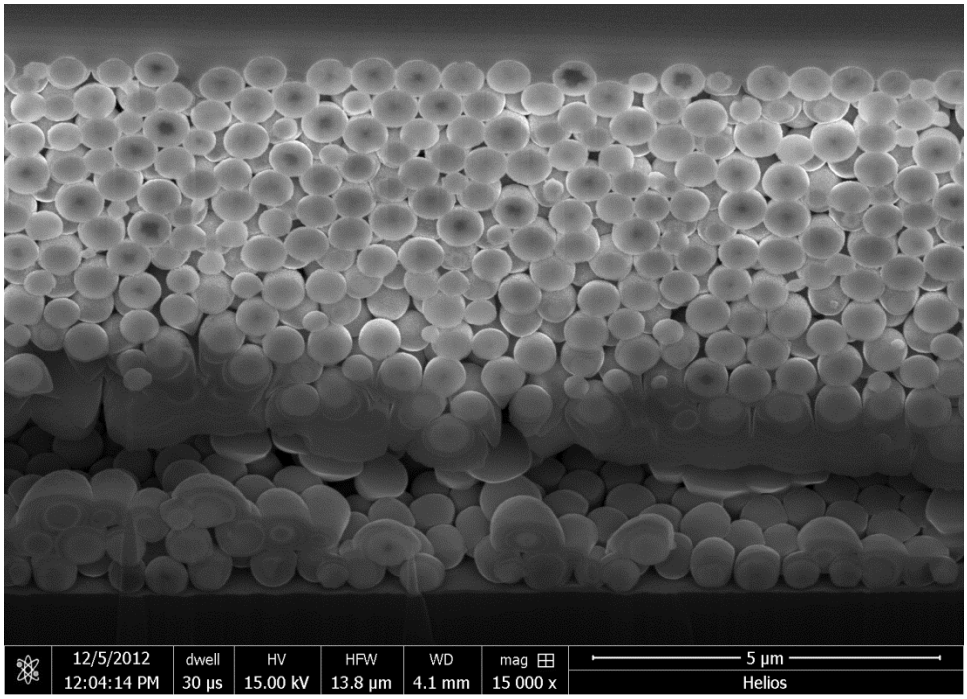

Figure 26 FIB cross-section of silica template coated with 500 cycle Pt ALD.

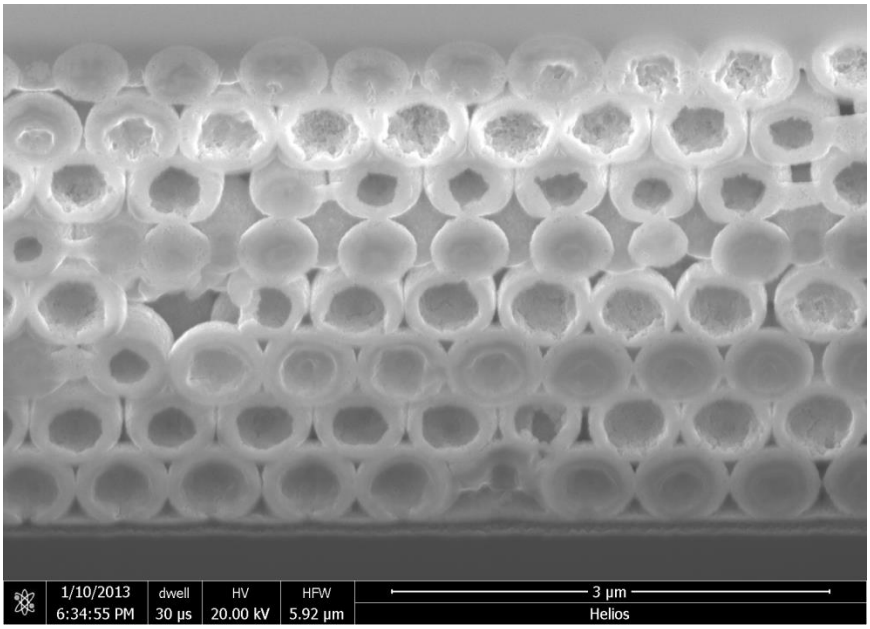

Figure 27 FIB cross-section of silica template coated with 500 cycle Pt ALD after HF etching of the silica.

3.2 Thermal Transport in Nanostructured Silicon

It has been recently shown that control of heat flow can be achieved by confining phonon waves in silicon inverse opals [90]. Using different size colloidal crystals as templates for silicon CVD, different silicon thickness will arise due to varying pinch-off points (e.g., 23 nm for 300 nm diameter colloids and 49 nm for 640 nm diameter colloids). Crystallizing these shells creates nano-crystalline silicon, where the grain size is approximately the shell thickness due to confinement. With thinner silicon shell, and therefore smaller grains, the thermal conductivity drops. This section describes the work done to extend these concepts to silicon CVD in mesoporous silica, broadening the understanding in thermal transport of nanostructured materials.

Several challenges present themselves by undertaking this study, the main two being as follows: (i) how to obtain meaningful thermal data, and (ii) whether this data can be correlated to sample parameters (e.g., silicon thickness, grain size, etc.). The recent paper employed the 3-ω method to measure the thermal conductance of the effective thin film. This is appropriate due to the inverse opal structure: heat will flow into the silicon "shell" and travel around the air voids. By modeling this system, the authors can extract quantitative thermal conductance of the effective film and, as a result, the silicon material. However, by studying the thermal conductance in the silicon nanowires deposited inside the mesopores, the model they used is no longer valid; a new, detailed model that takes into consideration the silicon shell and nanowires would have to be created, one where extracting the nanowire thermal conductance is not guaranteed. Another approach is using time-domain thermoreflectance (TDTR); TDTR is a surface measurement technique, measuring only ~50 nm into the sample [91]. TDTR measurements require that the

sample surface be smooth, much smoother than the opal contour. Fortunately, an area of ~20x20 μm is sufficient for the measurement, which may be possible with a FIB cut. Correlating the data to sample parameters requires forethought in what samples are tested and how the samples are prepared. To study the effect of the nanowire size, heat must travel through the nanowires, instead of simply around the shell. This is partially solved by switching to the TDTR technique; additionally, depositing only enough silicon to fill the mesopores will keep the shell thickness to a minimum. To gain a greater understanding of the thermal conductivity, the silicon nanowire diameter should be varied significantly, at least by a factor of two. Additionally, there may be correlations between the conductivity and surface area or pore volume. Finally, the best thermal conductance measurements will come from silicon nanowires surrounded by air, so the colloids will have to be removed prior to measurements.

As mentioned previously, the pore size of the silica can be easily controlled by the addition of alkyl chain surfactants during colloid growth, with silica colloids containing mesopores with diameters spanning 2 – 7.3 nm fabricated by Yano and coworkers [75, 76]. Additionally, another silica colloidal batch was synthesized to have pore diameter of 10 nm or greater, which is outside the range of the nitrogen adsorption tests; transmission electron micrographs were used to estimate the pore diameter to be approximately 18 nm. Mesoporous carbon spheres, while advantageous due to the ease of colloid removal, vary between only 1.5 and 4.3 nm in pore size. While using silica incorporates hydrofluoric acid etching, the mesopore range allows for better experiments. Using a dilute, ethanolic HF etch, or a glycerin/ethanolic one, should reduce or eliminate any etching of the silicon nanowires, especially after silicon crystallization.

For sample fabrication, a number of different options presented themselves, with two that appeared promising. In one case, a silica colloidal crystal would be fabricated as a template, followed by silicon CVD. After silicon crystallization and template removal, a spot ~10x10 or 20x20 μm needs to be polished using the FIB, allowing for TDTR measurements. The second method involves creating a mesoporous silica film that can be infiltrated via CVD. This eliminates the FIB polishing, as the film will not have the colloid curvature. For both of these, pore size should vary by at least a factor of two for meaningful results. As such, the silica colloids with 18 nm pores were initially used.

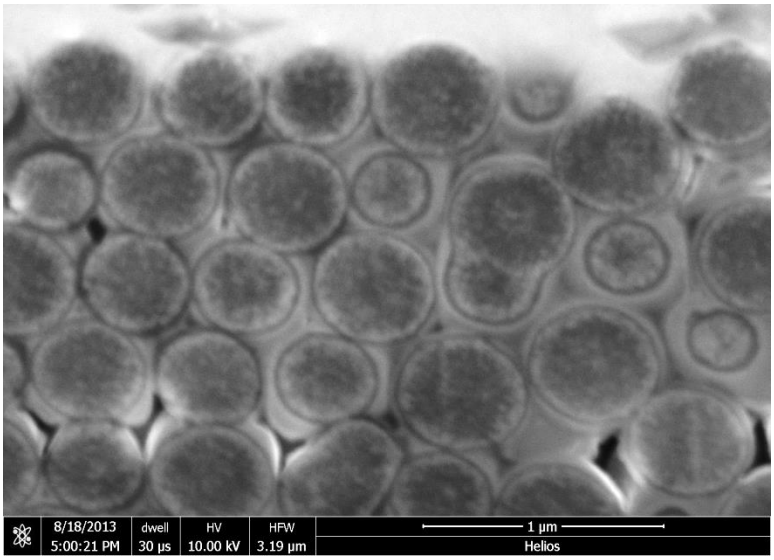

Figure 28. FIB cross-sectional image of the large-pore silica template used for silicon CVD.

Due to the synthesis conditions creating the large mesopores, the silica colloids are not as monodisperse compared to their smaller pore counterparts. However, a colloidal crystal with numerous defects still would allow adequate measurements, due to TDTR only probing the surface. A disordered colloidal crystal of the 18-nm pore silica was deposited on a silicon

substrate, followed by silicon CVD. The FIB cross-sectional image is shown in **Figure 28**, showing the silicon infiltrating the pores. The silica colloids, without silicon CVD, were imaged via transmission electron microscopy (TEM) (**Figure 29**).

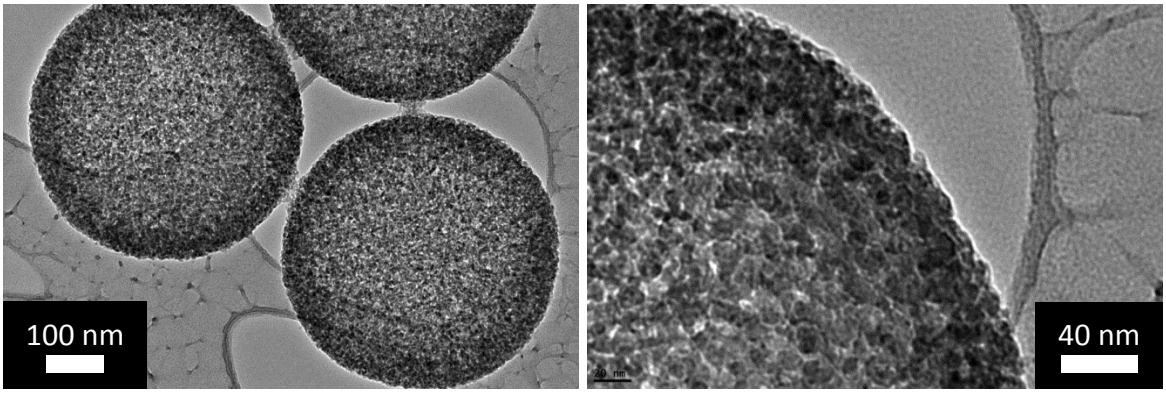

Figure 29. TEM images of the "large-pore" silica.

Prior to the extensive sample preparation needed to make a smooth top surface for TDTR measurements, four samples of mesoporous silica on silicon substrates were obtained, greatly simplifying the thermal measurement sample prep. These samples were fabricated by changing the synthesis time of the mesoporous silica, with times of 24, 48, and 72 hr. SEM analysis showed the 48 hr sample has a thickness of approximately 150 nm, which is significantly large enough to effectively ignore substrate effects during the thermal measurements, as TDTR samples approximately 50 nm into the surface. After silicon CVD and crystallization, aluminum was sputtered on the top surface of the 48 hr mesoporous silica film for TDTR measurements. Unfortunately, after the sputtering, the sample exhibited a diffuse reflectance, even though the silicon-silica composite reflectance was specular. SEM was done (**Figure 30**), and the images show large-scale roughness and inconsistent coverage. This may be due to the aluminum

sputtering process. As TDTR utilizes a reflected laser beam off the aluminum surface to detect the thermal change, the surface needs to have specular reflectance for accurate data.

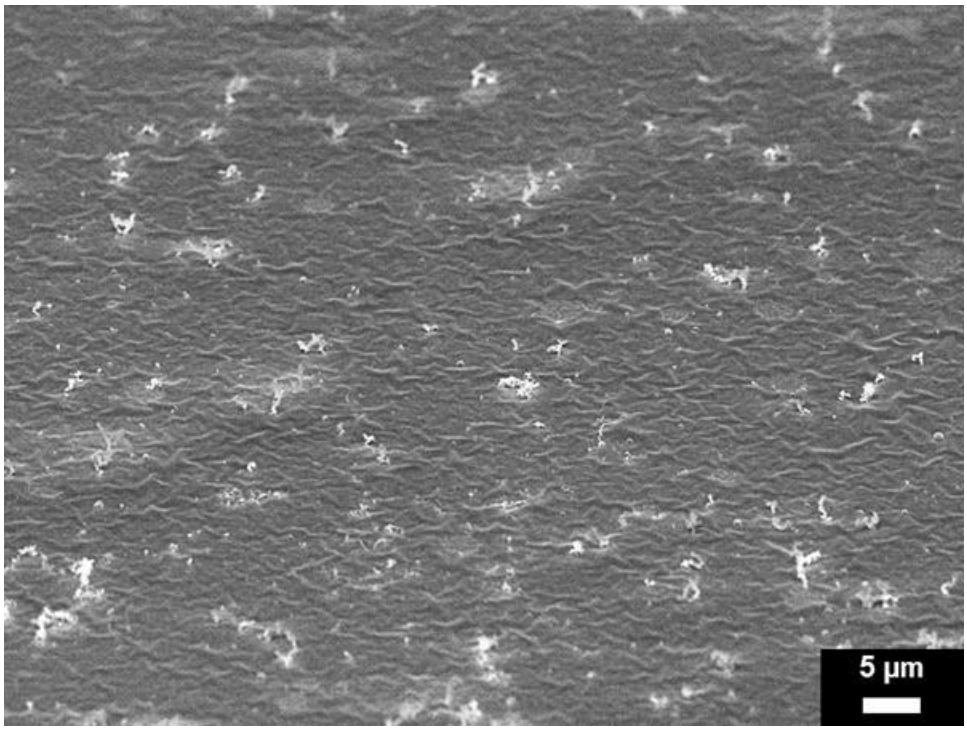

Figure 30. SEM of the aluminum-coated silicon-silica composite for TDTR measurements showing large-scale roughness that leads to the diffuse reflectance.

Another trial resulted in successful thermal measurements. A control sample of 200 nm of CVD silicon was deposited on a silicon wafer and crystallized. After sputtering aluminum, TDTR measurements were taken, with the data shown in **Figure 31**. By fitting the data to thermal conductance models, the thermal conductivity of the polycrystalline silicon was determined to be 38 W $m^{-1}K^{-1}$, which is in good agreement with published values between 22 and 65 W $m^{-1}K^{-1}$ [92, 93]; the full parameter set used in the modeling is listed in **Table 1**.

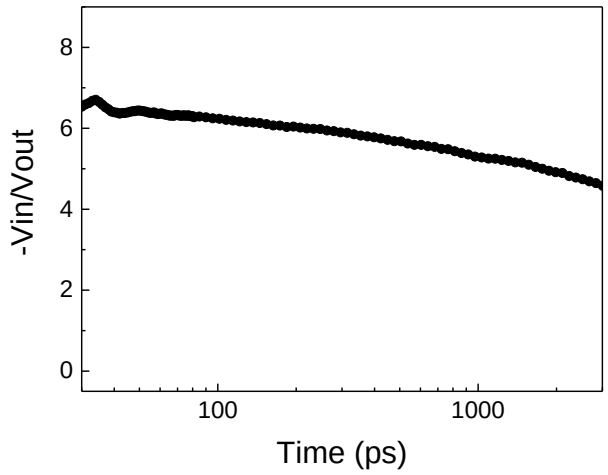

Figure 31. TDTR data from 200 nm polycrystalline silicon on a silicon wafer substrate.

Table 1. Parameters used in fitting the TDTR measurement data to determine the polycrystalline silicon thermal conductivity.

Material	Thermal Conductivity [W $m^{-1}K^{-1}$]	Heat Capacity [J $cm^{-3}K^{-1}$]	Thickness [nm]
Al (Absorption layer)	1840	24.2	1 (64.6 nm)
Al	184	2.42	57.6
Interface	0.1	0.1	1
Si (CVD)	38	1.64	200
Interface	0.1	0.1	1
Si	142	1.64	1.0×10^7

By using this value of 38 W $m^{-1}K^{-1}$ for the polycrystalline Si CVD thermal conductivity, the thermal conductivity of the composite can be determined, as there will be an overlayer of Si deposited on the mesoporous silica template, even with low-pressure Si CVD. Samples containing 150 nm of mesoporous silica were coated with Si via CVD under conditions that should have deposited approximately 20 nm nominally. However, the acoustic signal indicates

that the Si overlayer is approximately 40 nm (**Figure 32**). This thickness assumed the sound velocity in the Si overlayer was 8400 m s^{-1}, which is the longitudinal velocity for Si in the [001] direction and assumed to be single-crystal [94]. Unfortunately, there are no reports listing the sound velocity in polycrystalline Si. However, the thermal conductivity of the Si-mesoporous silica composite can still be calculated; **Figure 33** shows the experimental TDTR voltage ratio along with the model used [95]. From the model, the thermal conductivity of the Si-mesoporous silica was determined to be between 2.2 and 2.4 W $m^{-1}K^{-1}$, full model parameters are shown in **Table 2**. This model assumed a composite heat capacity of 1.63 J $cm^{-3}K^{-1}$, a 6:4 ratio of Si and SiO_2. This composite thermal conductivity is an order of magnitude lower than the polycrystalline Si and almost double the thermal conductivity of pure silica (1.3 W $m^{-1}K^{-1}$ for a thin film [96]). Additionally, it has been shown that microporous silica has a decreased thermal conductivity due to the phonon scattering by the micropore boundaries [97]. As this system utilizes mesoporous silica, the thermal conductivity should also be decreased.

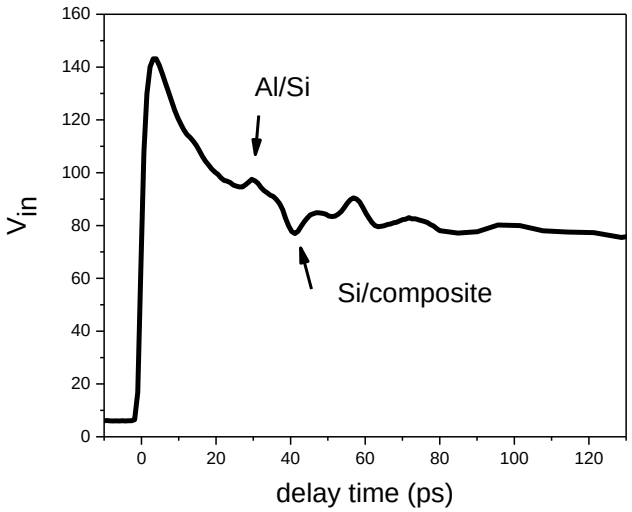

Figure 32. TDTR data of the Si-mesoporous silica composite, determining the aluminum and Si overlayer thicknesses.

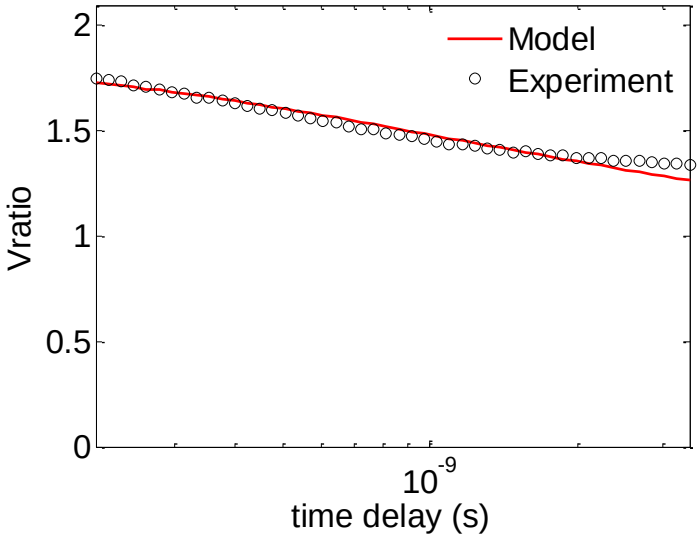

Figure 33. TDTR experimental data and model for the Si-mesoporous silica composite.

Table 2. Parameters used in modeling the TDTR measurement data for the Si-mesoporous silica composite thermal conductivity.

Material	Thermal Conductivity [W $m^{-1}K^{-1}$]	Heat Capacity [J $cm^{-3}K^{-1}$]	Thickness [nm]
Al (Absorption layer)	1840	24.2	1 (81.4 nm)
Al	184	2.42	74.4
Interface	0.1	0.1	1
Si (overlayer)	38	1.64	40
Interface	0.1	0.1	1
Si (CVD) / SiO_2	2.2-2.4	1.63	150
Interface	0.1	0.1	1
Si	142	1.64	1.0 x 10^7

To extract the exact thermal conductivity of each component of the Si-mesoporous silica, a detailed study would be required; at a minimum, the silica mesopores should be varied to allow for increased Si deposition. However, modeling of thermal conductivities of composites [98] can provide estimates. In this system, a simple parallel model can provide a first-order approximation:

$$\frac{\mathbf{1}}{\boldsymbol{k_c}} = \frac{\mathbf{1}-\boldsymbol{\varphi}}{\boldsymbol{k_{silica}}} + \frac{\boldsymbol{\varphi}}{\boldsymbol{k_{Si}}} \qquad \mathbf{4}$$

where k_c, k_{silica}, and k_{Si} are the thermal conductivities of the composite, mesoporous silica (continuous phase), and Si (discrete phase), respectively, and φ is the volume fraction of the Si. From the microporous silica study [97], the thermal conductivity range is between 0.85 and 1.1 W $m^{-1}K^{-1}$. From the mesoporous silica synthesis, the mesopore diameter is approximately 2.3 nm with 58% porosity. Due to the confinement of the silicon, the silicon grain size should be similar to the mesopore diameter [90]. Modeling the system by inputting the silica thermal conductivity in a range of 0.85 to 1.3 W $m^{-1}K^{-1}$, taking into the full range of the microporous study as well as the thin film silica, estimates of the Si thermal conductivity can be obtained and are shown in **Figure 34**. Clearly, the model deviates and sets a lower boundary of the silica thermal conductivity to 0.93 W $m^{-1}K^{-1}$. In Fang, et al., microporous silica study, their sample with porosity 58%, the same used in this study, had a room temperature thermal conductivity of approximately 1.05 W $m^{-1}K^{-1}$. Substituting this value into the parallel model provides a Si thermal conductivity of 10.6 W $m^{-1}K^{-1}$, less than a third of the polycrystalline Si film; however, this is still a factor of 2 higher than the reported polycrystalline inverse Si opal with a 20 nm crystallite size (approximately 5 W $m^{-1}K^{-1}$) [90]. Additionally, reports on the thermal conductivity of porous silicon have it as low as 0.1 W $m^{-1}K^{-1}$ at room temperature [99]. A more detailed study, with varying the mesopore diameter, is necessary for obtaining a clear result.

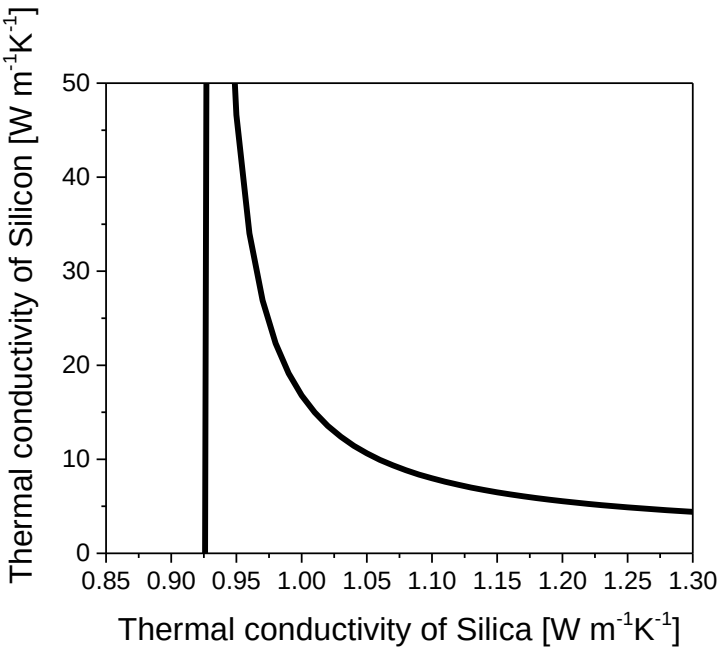

Figure 34. Modeled thermal conductivity of Si as a function of the thermal conductivity of silica, using the parallel thermal conductivity model [98].

3.3 Conclusions

Mesoporous silica was employed in two unique applications. A colloidal crystal, containing 622 nm diameter silica colloids with 2.27 nm diameter mesopores, was used to template platinum deposited via ALD. This created a mesoporous shell of platinum after the HF etching of the silica, due to the incomplete penetration of the platinum during the ALD. Additionally, silicon was infiltrated into the mesoporous silica for thermal conductivity measurements. These measurements were successful and showed polycrystalline silicon, deposited via CVD, has a thermal conductivity of 38 W $m^{-1}K^{-1}$, while the effective thermal conductivity of the Si-silica composite was an order of magnitude less, between 2.2 and 2.4 W $m^{-1}K^{-1}$. Simple modeling using a parallel thermal conductivity model attempted to extract the material thermal conductivity of the silicon; however, detailed investigations are needed for accurate results.

CHAPTER 4

CARBON COLLOIDAL CRYSTALS:

FABRICATION, TEMPLATING, AND OPTICAL PROPERTIES

The fabrication of high-quality colloidal crystals from mesoporous carbon colloids is first demonstrated by tailoring the surface charge on the mesoporous carbon colloids. This colloidal crystal is then used as a unique template, due to its high temperature stability, nanostructured and high surface area, and easy removal, with porous oxide and semiconductor inverse opals obtained through an orthogonal process. Through atomic layer deposition and static chemical vapor deposition, the templated materials penetrate deep into the ultra-high surface area colloids, generating the porous inverse opal after carbon removal processes that are not destructive to the deposited materials. This allows for the fabrication and preservation of unique, nanostructured materials that are inherently difficult to template with conventional techniques. Presented in this chapter is primarily work published in *Advanced Optical Materials* [1].

4.1 Fabricating Carbon Colloidal Crystal

As a first attempt to make a carbon colloidal crystal, Monodispersed Starburst Carbon Spheres (MSCS), synthesized as previously reported [77], were dispersed into ethanol and deposited on a substrate via convective deposition [48, 100, 101]. Even though the polydispersity of the MSCS was very low (only 1.038), the result was a disordered film, probably because the zeta-potential of the as synthesized MSCS was only -14 mV. This compares to a zeta-potential of -31 mV measured for typical opal-forming silica particles. It has been shown that partial oxidation of carbon fibers introduces ionizable oxygen species (e.g., carboxylic acid) [102]; these species would increase the surface charge. Heating the MSCS in air at 300 and 400 °C increased the

surface charge with no significant size change; see **Table 3** and **Figure 35** for zeta-potential and SEM analysis.

Table 3. MSCS surface properties after heat treatment for 30 min.

Heat treatment [°C]	Diameter [nm]	Zeta Potential [mV]	Pore volume [mL g^{-1}]	Pore size [nm]	Specific surface area [m^2 g^{-1}]
As prepared	484 ± 19	-14 ± 6	1.00	1.67	1670
300	475 ± 7	-26 ± 6	0.92	1.74	1490
400	473 ± 7	-46 ± 4	0.92	1.87	1360
500	244 ± 10	-34 ± 4	0.37	-	420
600	-	-	-	-	-

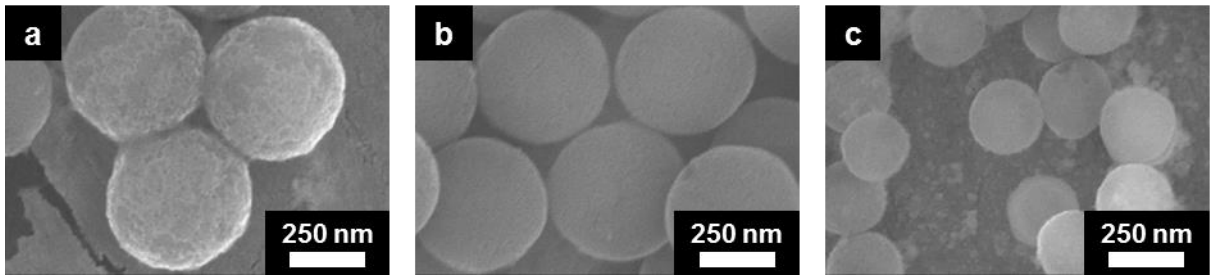

Figure 35. MSCS oxidized for 30 min. at (a) 300 °C, (b) 400 °C, and (c) 500 °C.

Significant size reduction occurred at 500 °C, and by 600 °C, the MSCS sample disappeared due to complete oxidation of the carbon [102]. To verify the porous structure of the MSCS remained through the oxidations, nitrogen adsorption measurements were conducted (**Figure 36**); the pore volume, size, and specific surface area are included in Table 3. The structural characteristics of the MSCS oxidized at 300 and 400 °C change very little. There is only a minor decrease in pore volume and a slight increase in pore size due to partial collapse of micropores, with the surface

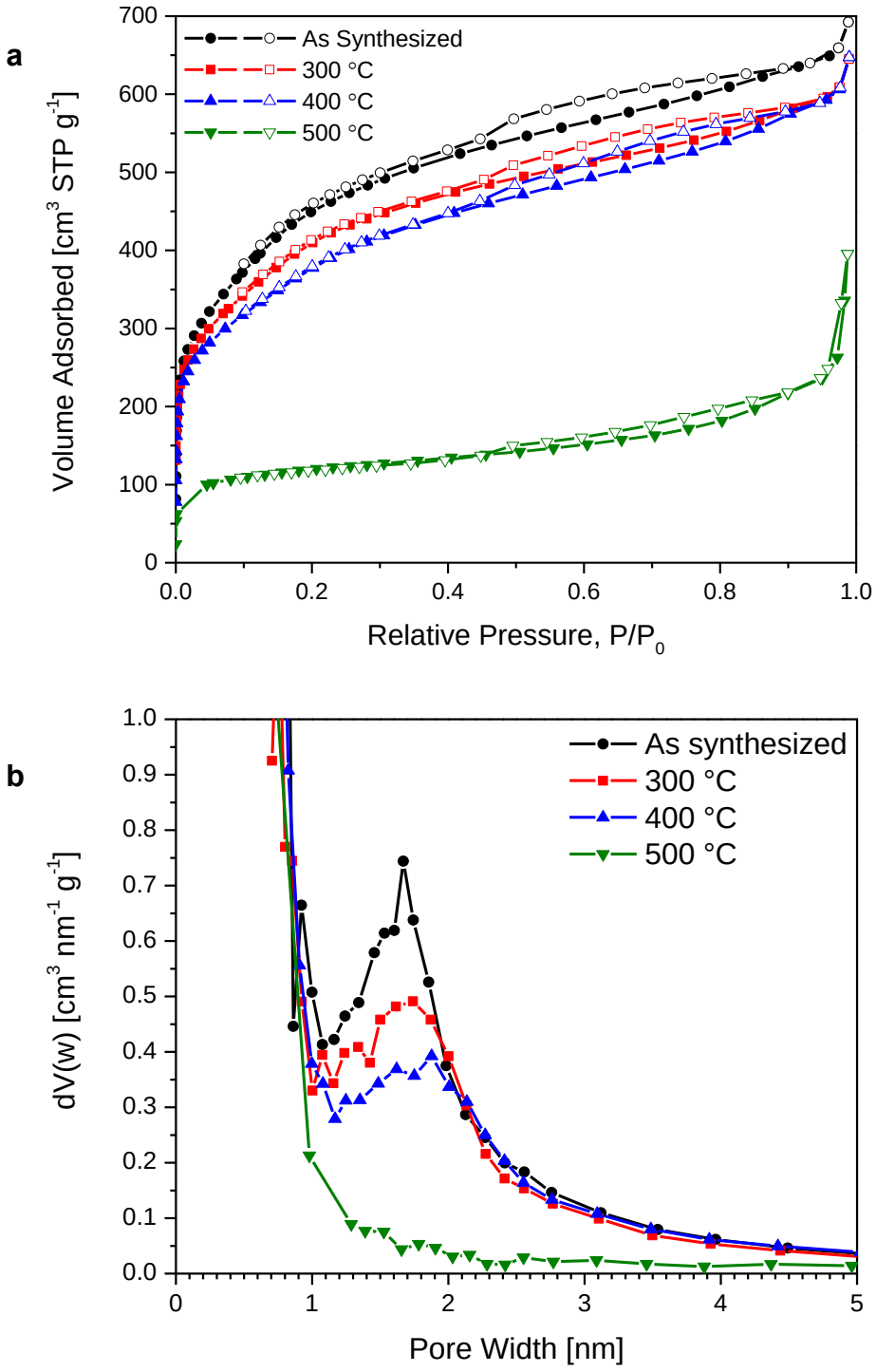

Figure 36. (a) Nitrogen adsorption (solid circles) and desorption (open circles) isotherms of as prepared MSCS (black curve), and MSCS oxidized at 300 °C (red), 400 °C (blue), and 500 °C (green). (b) Calculated pore size distribution from (a).

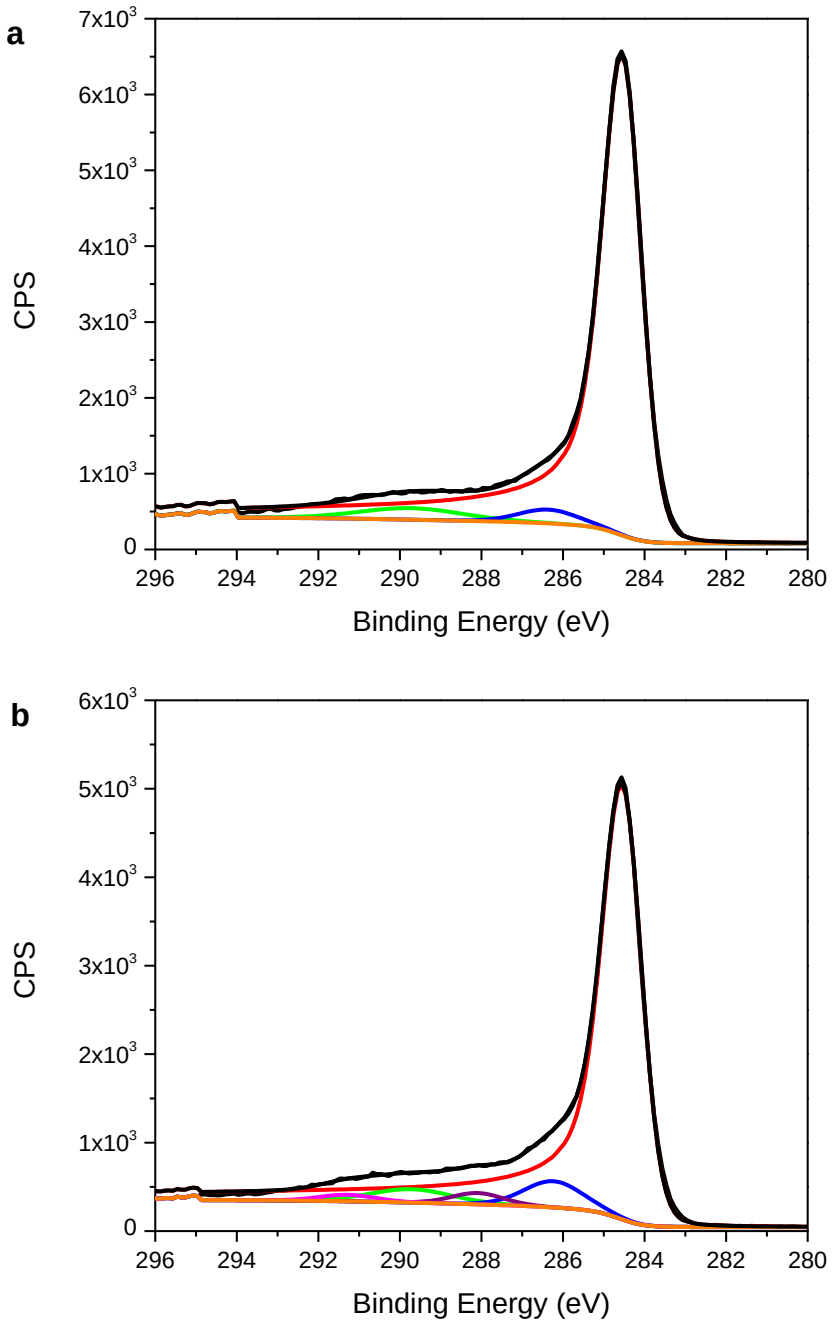

Figure 37. XPS C1s region for (a) as-synthesized MSCS and (b) oxidized MSCS at 400 °C. The main C-C was set to a binding energy of 284.5 eV.

Table 4. XPS data for virgin and 400 °C oxidized MSCS

		XPS atomic bonding [%]	
Bond	Binding Energy [eV]	As prepared	400 °C
C-C	284.5	97.5	92.0
C-OH	286.3	2.5	5.0
C=O	288.1	0	1.9
C-OOH	291.3	0	1.1

area remaining over 1300 m^2 g^{-1}. Oxidation at 500 °C resulted in significant decreases in both pore volume and surface area, and there is now no clear mesopore pore size distribution. To investigate the surface chemical effects of oxidation, X-ray Photoelectron Spectroscopy (XPS) was conducted on the as-synthesized and 400 °C treated samples (**Figure 37** & **Table 4**). In these, the main C 1s peak was set to a binding energy of 284.5 eV, with the pi-pi* shake-up shifted 5.231 eV to 289.731 eV. Table 4 lists the atomic binding percentages for the two samples. The surface of the oxidized carbon contained significantly more oxygen containing moieties, i.e., hydroxyls, quinones, and carboxylic acids (C-OH, C=O, C-OOH). The presence of these functional groups agree well with the increased surface charge measured for the oxidized MSCS and is consistent with other results [102]. Colloidal crystal formation was then attempted using the MSCS with the increased surface charge. Both the 300 °C and 400 °C oxidized samples formed colloidal crystals, with the sample oxidized at 400 °C producing the highest quality (shown in **Figure 38)**. The higher quality of the colloidal crystals fabricated using the 400 °C oxidized MSCS can be attributed to the increased stability of the suspension due to the higher surface charge compared to the as-synthesized and 300 °C oxidized (-46 mV vs. -14 & -26 mV, respectively). Although colloidal crystals produced this way show high degree of order

in the Scanning Electron Microscopy (SEM) micrographs, due to the strong absorption of carbon, a low optical reflectivity and transmission was observed (**Figure 39**).

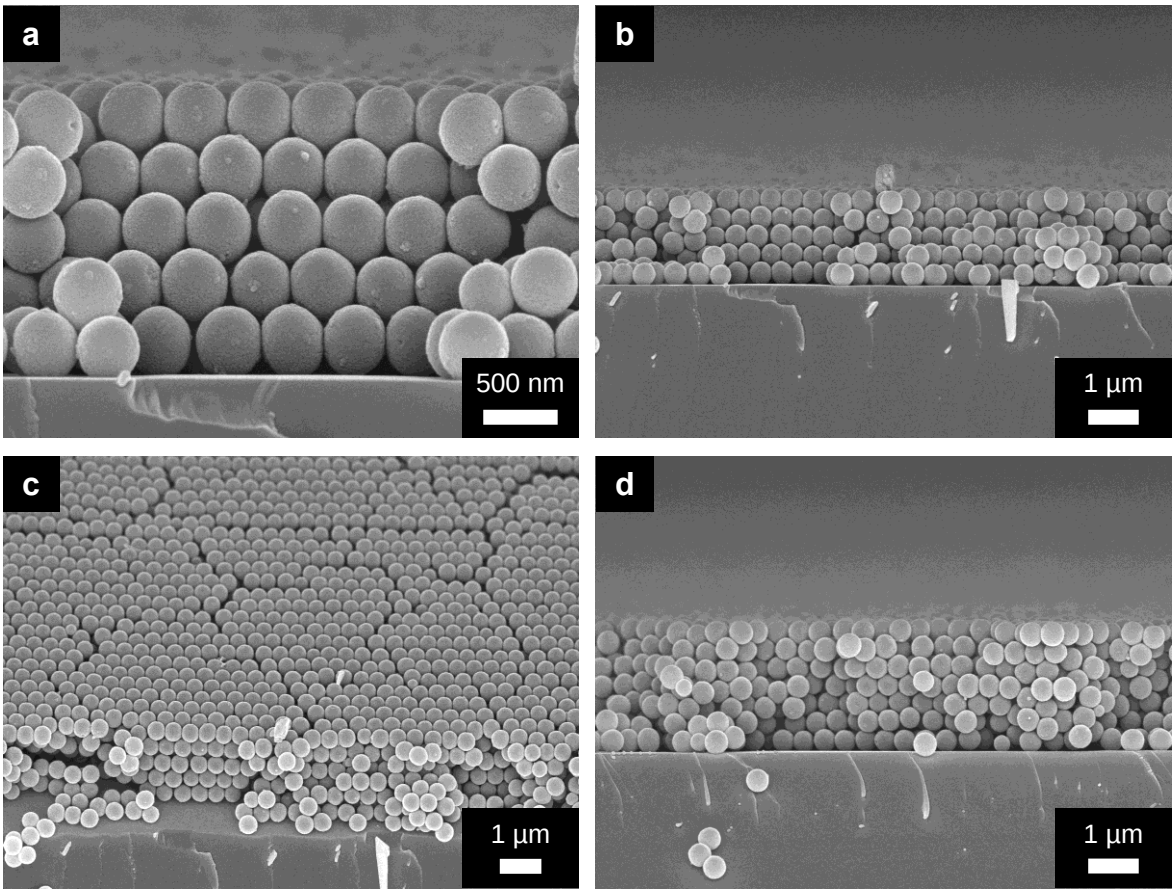

Figure 38. (a & b) SEM micrographs showing cross-section views of a 5-layer colloidal crystal. (c) Oblique view of (a & b). (d) Cross-section micrograph of 7-layer colloidal crystal. Colloidal crystal was fabricated from 400 °C oxidized MSCS.

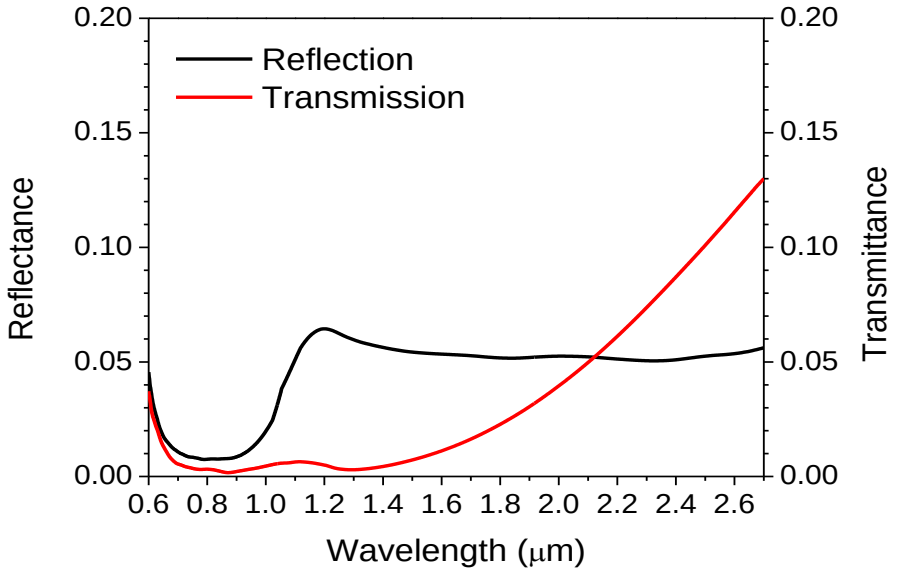

Figure 39. Optical measurements of MSCS colloidal crystal.

4.2 Mesoporous Starburst Carbon Spheres as Templates

Due to the MSCS porosity and potential for complete removal by oxidation in air, the carbon colloidal crystals are ideally suited as templates to create unique nanostructures after inversion. Employed here are two gas-phase deposition techniques that allow deep infilling of the mesopores: atomic layer deposition (ALD) of hafnia (HfO_2) and alumina (Al_2O_3) and static chemical vapor deposition (CVD) of silicon (Si). SEM micrographs after 100 cycles of ALD HfO_2, 10 nm nominally on a flat substrate, are shown in **Figure 40**. Verification of pore infiltration was done through a Focused Ion Beam (FIB) cut on a carbon/HfO_2 composite colloidal crystal, i.e., prior to carbon removal (Figure 40a). Transmission Electron Microscopy (TEM) was also conducted on the composite colloid (Figure 40a, top). The top of the colloidal crystal has a thick sputtered gold coating required for FIB milling; no gold was coated after milling on the exposed surface. Carbon, due to its low atomic number, appears darker than the

HfO_2 in the SEM micrograph. The micrograph shows a bright HfO_2 shell and spokes of HfO_2 penetrating the MSCS. Measurements reveal the HfO_2 infiltrates approximately 80 nm. ALD is known to fill deep vias and other high-aspect ratio structures, and thus deep infilling of the MSCS was not a surprise [103].

After a brief Reactive Ion Etch (RIE) to open the top HfO_2 surface, carbon was thermally removed at 600 °C for 1 hr. Unlike wet or deep RIE etching required for silica template removal,

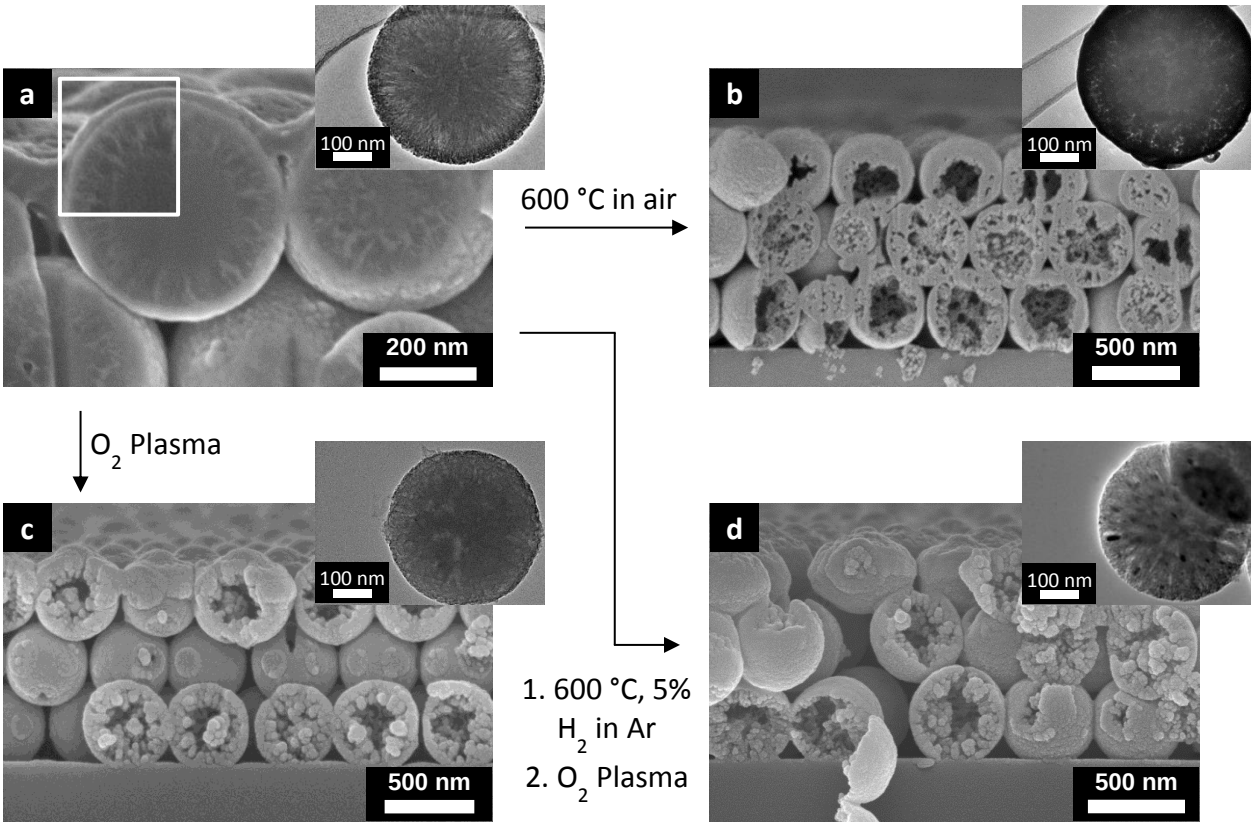

Figure 40. SEM and TEM (insets) micrographs of HfO_2-MSCS system. (a) FIB cross-section of a carbon opal with HfO_2 infiltrating mesopores (white inset: contrast enhanced). (b-d) Fracture surfaces (b) HfO_2 inverse opal created after carbon opal removal at 600 °C in air. (c) HfO_2 inverse opal fabricated through carbon removal via oxygen plasma. (d) HfO_2 inverse opal annealed at 600 °C with 5% H_2 in Ar, with the carbon removed via oxygen plasma.

this thermal removal process does not remove HfO_2, so all the deposited HfO_2 remains. Figure 40b shows the HfO_2 inverse opal SEM and TEM micrographs. In these, a granular HfO_2 structure exists, perhaps due to the HfO_2 crystallizing during the thermal MSCS removal. Since carbon can be readily removed through oxygen plasma at room temperature, it was possible to evaluate the structure of the HfO_2 in the as-deposited state. The top of the HfO_2-coated MSCS colloidal crystal was opened via RIE etching, followed by an oxygen plasma etch to remove the MSCS. The resulting inverse opal (Figure 40c) contrasts sharply with the thermally removed MSCS; a smooth, instead of granular, nanostructure is observed. It appears that during the MSCS thermal removal process, grain growth and sintering in the HfO_2 occur simultaneously with carbon removal. Once the MSCS support is removed, the HfO_2 is free to crystallize and coarsen, while the as-deposited HfO_2 better replicates the ultra-high surface area MSCS.

To verify these hypotheses, experiments were conducted to crystallize the HfO_2 prior to MSCS template removal. As deposited, the HfO_2 is amorphous. To crystallize the HfO_2 prior to carbon removal, the sample was annealed in forming gas (5% H_2 in Ar) at 600 °C for 1 hr. This replicates the thermal removal process time and temperature; however, the forming gas limits MSCS oxidation. Crystallization of the HfO_2 prior to template removal is only possible due to carbon's high thermal stability and inert nature with respect to HfO_2. After annealing, the MSCS was removed through oxygen plasma. Cross-sectional SEM (Figure 40d) of this sample is strikingly similar to the as-deposited, oxygen plasma removed samples (Figure 40c). It appears the MSCS provided a support and template during HfO_2 crystallization, limiting sintering and grain growth, preserving the templated nanostructure. X-ray diffraction (XRD) on the as-deposited and annealed samples was used to confirm the amorphous nature of the as deposited

HfO_2 and its crystalline nature after annealing. For this experiment, it is important that the majority of the HfO_2 is deposited in the pores of the MSCS and not on the MSCS surface (the x-ray experiment does not distinguish between HfO_2 on the surface of the MSCS surface and in the pores), and so the number of ALD cycles was reduced to 60, depositing nominally 6 nm of HfO_2. Most of the HfO_2 will be inside the MSCS, and only a few nm will be on the surface of the carbon colloids. XRD shows the as-deposited HfO_2 is amorphous, while the annealed sample is

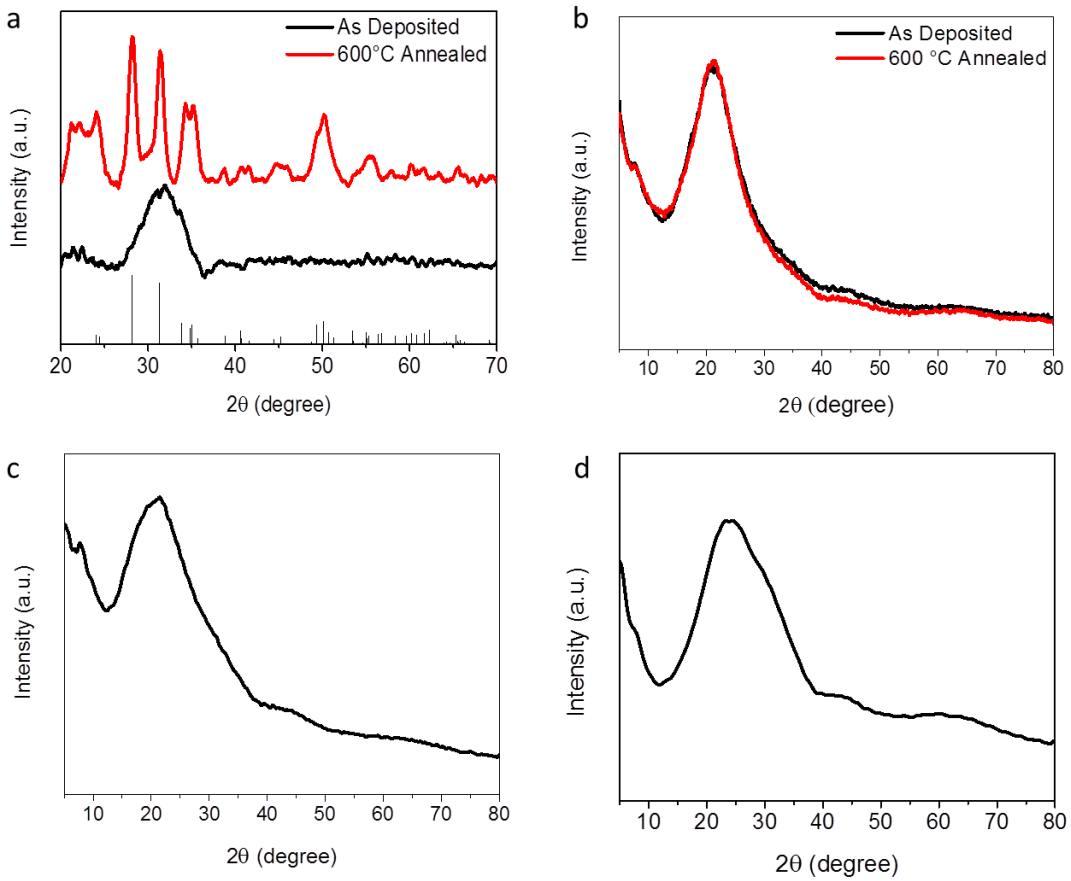

Figure 41. (a) XRD data of as-deposited (black) and annealed (red) HfO_2 ALD coated MSCS colloidal crystals. The HfO_2 JCPDS PDF file 04-004-7637 is shown for reference. (b) XRD data of the Al_2O_3 ALD coated MSCS opals. (c) XRD data of as-deposited Si static CVD. (d) XRD of the glass substrate used in these measurements.

crystalline (**Figure 41**). From the Scherrer Equation, the average crystallite was found to be 8.4 nm, substantially greater than the 1.87 nm MSCS pore size but significantly less than the total length infiltrated into the pores (~80 nm), indicating the HfO_2 crystallites may be rod-like. Transmission electron microscopy (TEM) (Figure 40d, top) and selected area electron diffraction (SAED, **Figure 42**) confirmed the crystalline nature of HfO_2.

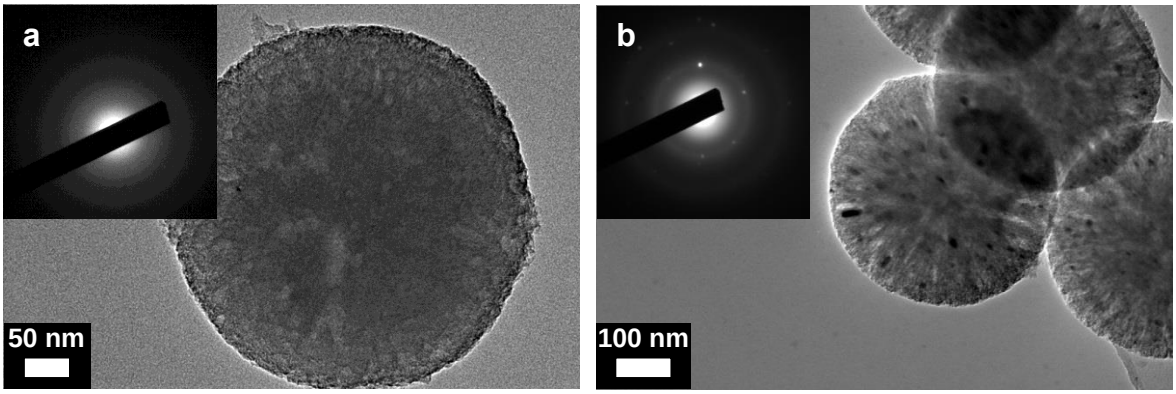

Figure 42. SAED and corresponding TEM images of the (a) as-deposited HfO_2 and (b) annealed HfO_2 on a MSCS.

100 cycles (10 nm nominally) of ALD Al_2O_3, with the MSCS thermally removed, is shown with a FIB cut in **Figure 43a**. As with the HfO_2, the thermal removal process is completely orthogonal to Al_2O_3 removal. In most of the MSCS, the Al_2O_3 infiltrates into the center; however, "defects" of partially unfilled MSCS occur (top right MSCS in Figure 43a). The TEM micrograph of the Al_2O_3 inverse colloid in Figure 43b shows the solid Al_2O_3 shell and porous center. Unlike for HfO_2, the Al_2O_3 inverse opal did not crystallize, and its mesostructure did not appear to Oswald ripen during thermal carbon removal at 600 °C (XRD in Figure 41). This may not be surprising, as 1100 °C is a typical crystallization temperature for alumina [104].

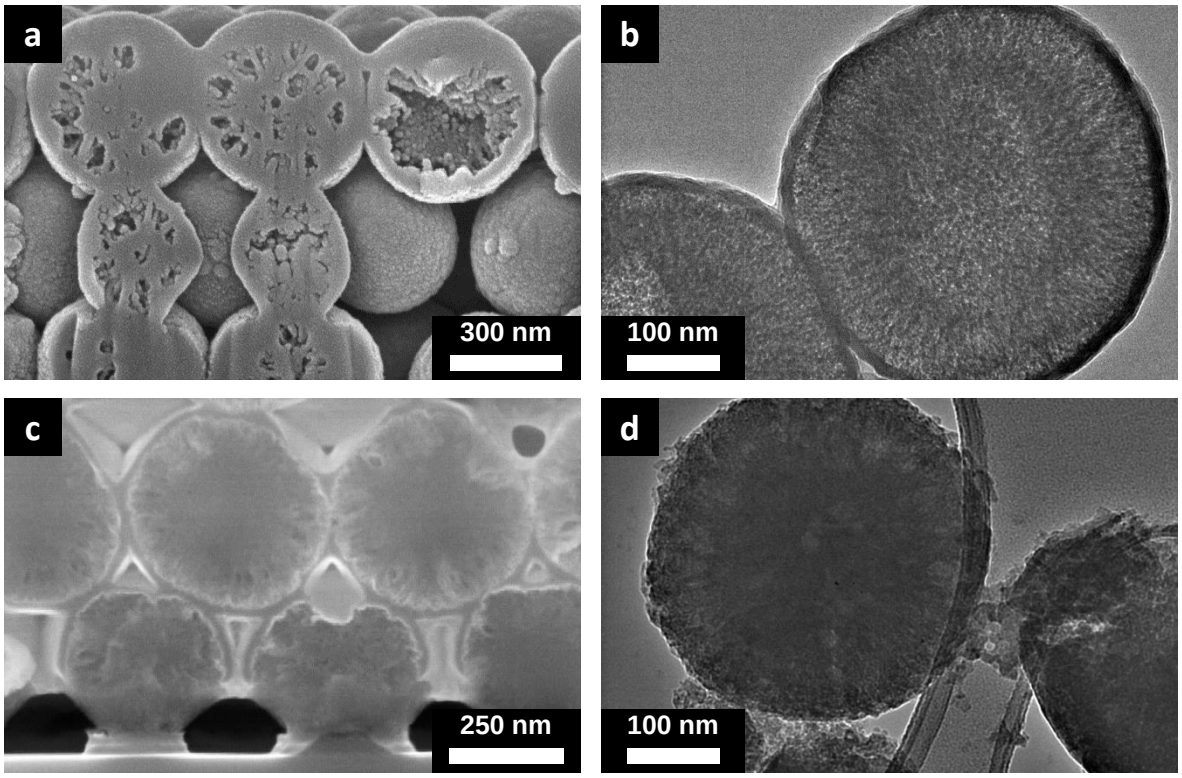

Figure 43. (a) FIB cross-section cut of ALD Al_2O_3 inverse opal with carbon template thermally removed. (b) TEM micrograph of Al_2O_3 structure in (a). (c) Silicon inverse opal fabricated via static CVD; carbon colloidal crystal template was removed via oxygen plasma. (d) TEM micrograph of silicon structures in (c).

The final successful material investigated for template inversion was Si, which is grown using static CVD. SEM and TEM micrographs are shown in Figure 43c & d. To prevent Si oxidation, MSCS were removed via room-temperature oxygen plasma after removing the top Si overlayer via RIE. The conformal Si static CVD deposition infiltrates the MSCS template, creating a porous-Si interior. As expected, XRD (Figure 41) reveals the as-grown Si is amorphous, as Si crystallization requires heating to 1000 °C for several hours. Platinum ALD in the MSCS was also attempted. However, due to oxygen being a reactant in the ALD growth, the MSCS colloidal crystal oxidizes and loses its well-defined order (**Figure 44**).

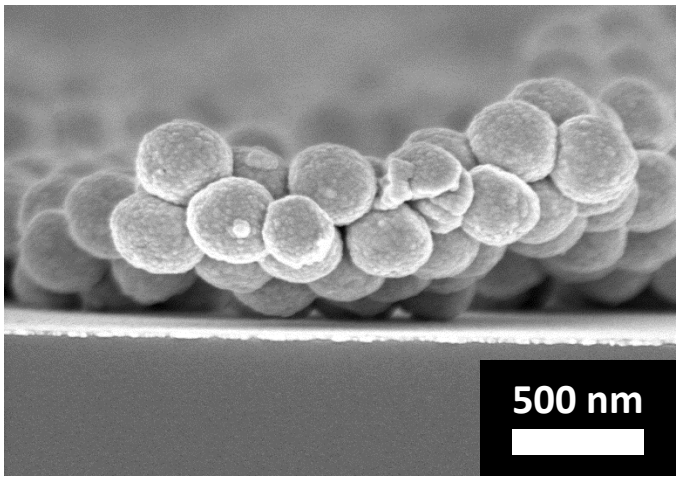

Figure 44. 500 cycle platinum ALD on carbon colloidal crystal.

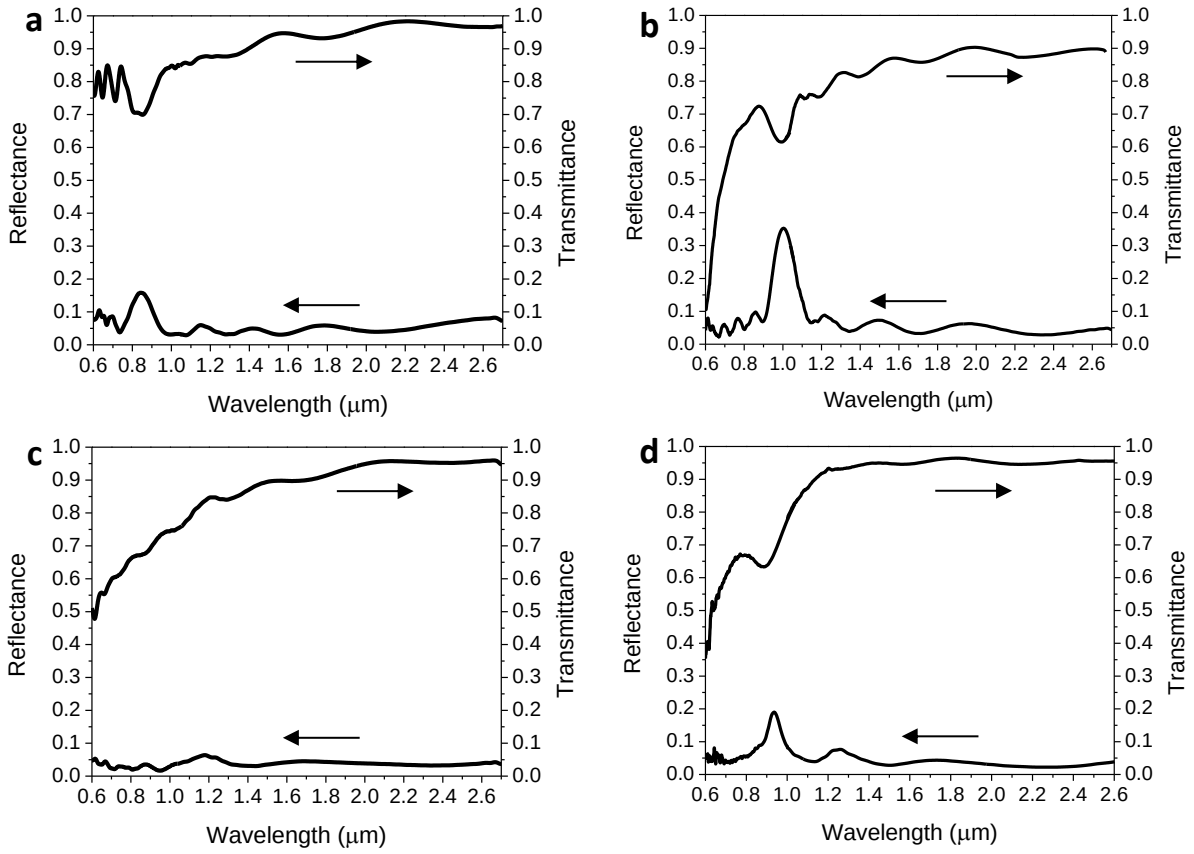

Figure 45. Optical measurements on inverse opals structures after carbon removal: (a) 100 cycle ALD HfO_2; (b) 300 cycle ALD HfO_2; (c) 100 cycle ALD Al_2O_3; (d) static CVD silicon.

Optical measurements were conducted on HfO_2, Al_2O_3, and Si inverted opals (**Figure 45**). Figure 45a shows the 100 cycle ALD HfO_2 inverse structure with a primary reflection peak of 16% at a wavelength of 840 nm. A MSCS colloidal crystal was also coated with 300 cycles HfO_2 (30 nm nominally). The optical measurements are shown in Figure 45b after the MSCS were removed. 30 nm of HfO_2 is below the pinch-off point (when the colloid interstitials fill and block further precursor deposition) of 37 nm for the 479 nm colloids. For the thicker HfO_2 deposition, the reflection peak red-shifts to 1.0 μm and increases to 35% with well-defined Fabry-Perot fringes. Since the mesopores are already full after 100 ALD cycles, the extra 200 cycles simply increase the thickness of solid HfO_2 shell around each MSCS particle, leading to the red-shift and increases in intensity of the reflection peak. The Al_2O_3 optical measurements are shown in Figure 45c. Interestingly, no reflection peak is observed; this could be the result of the infilling "defects," where a portion of the colloids have large voids in the center. These defects perhaps act as strong scattering centers. Optical measurements of the Si inverse structure are shown in Figure 45d; the main reflectance peak is at 940 nm with 19% reflectance. The transmittance measurement shows a primary dip of 63% corresponding with the reflectance peak; the remaining 18% of the light is either absorbed or scattered. Interestingly, the Si inverse structure has a transmittance of near 95% at longer wavelengths, compared to only ~55% for a typical Si inverse opal [105]. The high transmittance (low reflectance) is evidence that the effective refractive index of the porous Si structure is much lower than pure Si (~3.5).

4.3 Conclusions

In conclusion, by tailoring the surface charge of carbon colloids, high-quality carbon colloidal crystals can be fabricated and these high-surface area colloidal crystals can be used as templates

for a variety of materials, creating unique, high-surface area nanostructured inverse opals. These materials, HfO_2, Al_2O_3, and Si, penetrate deep into the mesopores of the MSCS. Importantly, the carbon removal process is completely orthogonal to the deposited material removal, preserving the fine-scale mesostructure of the MSCS in the templated materials. Because MSCS removal is orthogonal to the etching of many materials, MSCS provide a general approach for templating materials that currently cannot be templated by conventional colloidal crystals.

4.4 Experimental Procedures

Synthesis: Monodisperse Starburst Carbon Spheres (MSCS) were synthesized as previously reported [77]. The MSCS were oxidized in a Lindberg Furnace using a 30-min. ramp, 30-min. hold, and cooled to room temperature. For colloidal crystal fabrication, Piranha-cleaned substrates (glass or quartz) were placed at a 20° angle in a 20 mL scintillation vial with 0.7 g colloidal suspension (0.5-2 wt% in ethanol). The vials were placed in an incubator (Fisher, Isotemp 125D) and held at 40 °C overnight.

Infiltration and template removal: HfO_2 and Al_2O_3 ALD, using a Cambridge Nanotech ALD system, were done at 200 °C and 80 °C, respectively, on fabricated carbon colloidal crystals with both recipes having a growth rate of 1 Å $cycle^{-1}$. Si static CVD was done at 350 °C for 2 hr using Si_2H_6 [17]. A Reactive Ion Etch (RIE) using O_2 and CF_4 gasses (1 sccm each, 10 mTorr, 75 W, 1 nm min^{-1} HfO_2 removal) was done to expose the MSCS for thermal or oxygen plasma removal. Thermal removal was done at 600 °C for 1 hr with a 30-min. ramp. Oxygen plasma removal was done using 20 sccm O_2 at 400 mTorr, 200 W, for 2 hr.

Characterization: Nitrogen physisorption isotherms, BET specific surface area, and pore volume were measured and calculated as previously described [77]. Scanning Electron Microscopy

(SEM) was done on Hitachi S-4700 or S-4800. Transmission Electron Microscopy (TEM) was done on a JEOL 2010LAB_6 at an accelerating voltage of 200 kV. Focus Ion Beam (FIB) milling was done on a FEI Beam 235 FIB. Zeta-potential measurements were conducted in Millipore water on a NICOMP 380 ZLS Particle Sizer.

CHAPTER 5

ENERGY HARVESTING USING CARBON COLLOIDAL CRYSTALS

One of the most common energy-harvesting practices is through the absorption of photons and conversion into electrical energy; conventionally, this has been done with silicon solar cells. Dye-sensitized solar cells (DSSC), while not as efficient as conventional silicon solar cells, are attractive due to their low cost and thin film design, allowing a broad range of substrates and applications. By treating conductive surfaces appropriately, either through a thin oxide deposition or a self-assembly monolayer, monodispersed starburst carbon spheres could be assembled into colloidal crystals. When fabricated on a transparent conductive oxide, these colloidal crystals were used as a high-surface area template for dye-sensitized solar cells (DSSC). Through an atomic layer deposition, titania was deposited into the mesopores and was crystallized into the anatase phase without carbon oxidation and removal through an annealing process in an inert atmosphere. After crystallization, carbon was easily and orthogonally removed by simply changing from an inert to a non-inert atmosphere containing oxygen. Using a ruthenium dye and a standard iodine-iodide electrolyte, DSSC were fabricated from the templated titania and compared to another cell constructed using the standard, nanoparticle titania paste. While a number of experimental adjustments were made, ultimately the templated DSSC could not perform as well as the DSSC fabricated with the titania paste.

5.1 Carbon Colloidal Crystals on Conductive Substrates

For energy harvesting, as well as energy storage (see Chapter 6) devices, an electrical pathway is required to extract the charges from the device. For both applications, MSCS offer a unique, high-surface template. However, the adhesion between the carbon starburst spheres and

conductive substrates was found to be problematic, with most colloidal assemblies delaminating prior to final templating. This is presumably due to the inability of the substrate to maintain a surface charge, which is necessary for colloidal crystal formation [58]. MSCS assemblies on oxide substrates, including glass and quartz specimen slides, have resulted in well-arranged colloidal crystals due to the anionic surface charge of the substrate and the generation of oxidizable species on the MSCS surface [1].

Mentioned previously, Dye Sensitized Solar Cells (DSSCs) incorporate a wide-bad gap semiconductor, typically titania, to transport the electron to the back contact. Expanding upon the earlier success of oxide substrates, a thin layer of titania (8 nm) was deposited on the conductive, fluorine-doped tin oxide (FTO) substrate via ALD. Using the established procedure with this substrate, MSCS colloidal crystals were successfully fabricated. These assemblies were rather fragile; however, with careful handling and immediate processing, they were successfully templated.

5.2 Mesoporous Carbon for DSSC

DSSC, classified as a third-generation solar technology, consists of a wide-band gap semiconductor, a photosensitive dye, and an electrolyte. The photosensitive dye is adsorbed onto the mesoporous semiconductor; upon incident light, the dye absorbs the photon and charge separation occurs at the dye/semiconductor interface with the semiconductor providing a pathway for the electron [106]. This is in contrast to traditional silicon solar cells where the light absorption, charge separation, and the species transport all occur within the semiconductor. The mesoporous semiconductor provides high surface area for the dye adsorption; additionally, it

provides light scattering, increasing the optical path length, especially for high-frequency (short wavelength) photons [107]. Due to the dye's absorption properties, the long wavelength photons require multiple optical path lengths to be fully absorbed [45]. To improve the optical absorption of these long wavelengths, groups have incorporated larger particles that scatter longer wavelength (sacrificing surface area) [107], coupled the mesoporous semiconductor to a photonic crystal [41-45, 48], and used nanotubes [108] and hemispheres [46] in the semiconductor architecture. These techniques either sacrifice the surface area or require an additional processing step. Using a MSCS colloidal crystal as a template could allow for an improved optical response while keeping the high surface area. The colloid diameter could be tuned for optimal response in the red spectrum and the mesopores could be replicated in the templating process.

Prior to utilizing a titania oxide layer for colloidal crystal growth, a disordered MSCS film was deposited via drop-casting a colloidal solution onto a masked FTO substrate; titania was immediately deposited via ALD after solvent evaporation and mask removal. Future assemblies utilized the titania-coated FTO substrate and MSCS colloidal crystal as the template for titania ALD. As the anatase crystalline form of titania has improved electrical properties to the rutile crystal structure [109], the titania-MSCS composite was annealed at 500 °C for 2 hr under forming gas (5% H_2 in Ar). Annealing in forming gas prevented the MSCS oxidation, allowing the MSCS to act as a structural support during the titania crystallization. To remove the MSCS, the composite was heated for an additional 2 hr in air, also at 500 °C. The ruthenium dye and photovoltaic (PV) cell fabrication followed a similar procedure set by Wang, et al. [106]. The ruthenium dye (N-719) was dissolved as a 0.5 mM solution in 1:1 volume ratio of acetonitrile

and *tert*-butyl alcohol. To prevent water condensation, the titania substrates were placed in the dye solution once they cooled to 80 °C after the crystallization and MSCS removal process; the titania substrates were removed after 48 hr and assembled. For a reference electrode, a standard 20 nm titania particle paste was deposited on the FTO substrates after a titanium chloride treatment; the crystallization and subsequent processes were kept the same.

The initial, disordered MSCS template PV performance is shown in **Figure 46** against a standard reference cell made with the titania paste also fabricated at the same time. Of important note is all values reported here are externally measured on a broadband solar simulator; Quantum Efficiency (QE) and Incident Photon to Current Efficiency (IPCE) have not been measured. The reference cell has a Power Conversion Efficiency (PCE) of 3.6% under AM 1.5 illumination (100 mW cm^{-2}), while the templated cell only has a PCE of 0.9%. The majority of this efficiency loss is due to the decreased short-circuit current (I_{SC}), which corresponds to the magnitude of photons absorbed and successfully separated into charge carriers. This indicates that the templated cell absorbed less photons, possibility due to lack of adsorbed dye, or did not effectively separate the charges at the dye/titania interface. The open circuit voltage (V_{OC}) of the templated cell is 50 mV less than the reference (0.65 vs. 0.70 V) and the fill factor (FF) is also reduced from 0.61 to 0.52. These suggest internal resistances due to poor device fabrication.

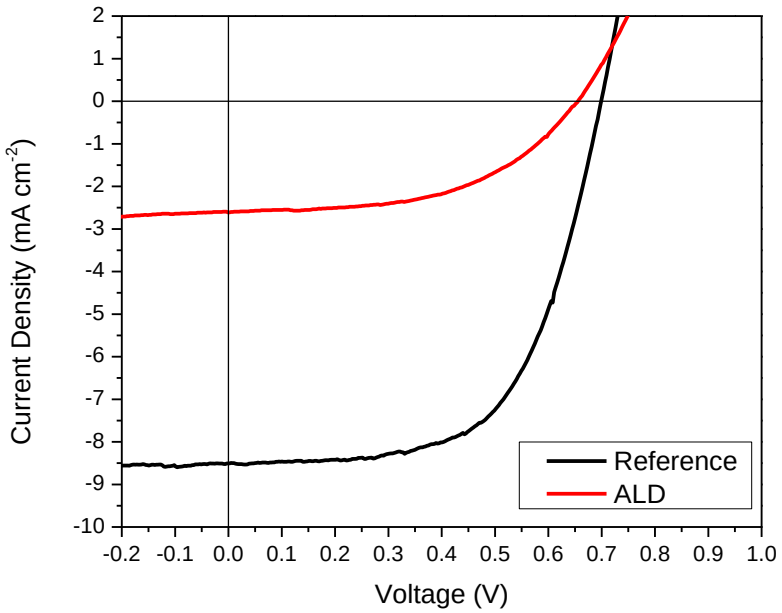

Figure 46. PV performance of reference DSSC fabricated via standard techniques (black) and DSSC using mesoporous titania via ALD (red). Standard DSSC: PCE = 3.6%, FF = 0.61, I_{sc} = 8.50 mA cm^{-2}, V_{oc} = 0.70 V; Mesoporous DSSC: PCE = 0.9%, FF = 0.52, I_{sc} = 2.61 mA cm^{-2}, V_{oc} = 0.65 V.

To investigate the titania electrodes, the cells were dismantled and imaged with the FIB (**Figure 47**). The ALD titania had a polymeric impurity coating the colloids, perhaps from the tape used to mask the FTO. This impurity would drastically alter the PV performance, increasing the internal resistance, limiting the light absorbed, and even affecting the charge separation. Switching from the drop-casting and masking process to the use of a MSCS colloidal crystal template on the titania-coated FTO should eliminate this impurity. The SEM of the titania paste electrode shows a clean film, consisting of the 20 nm titania nanoparticles, approximately 3 μm thick.

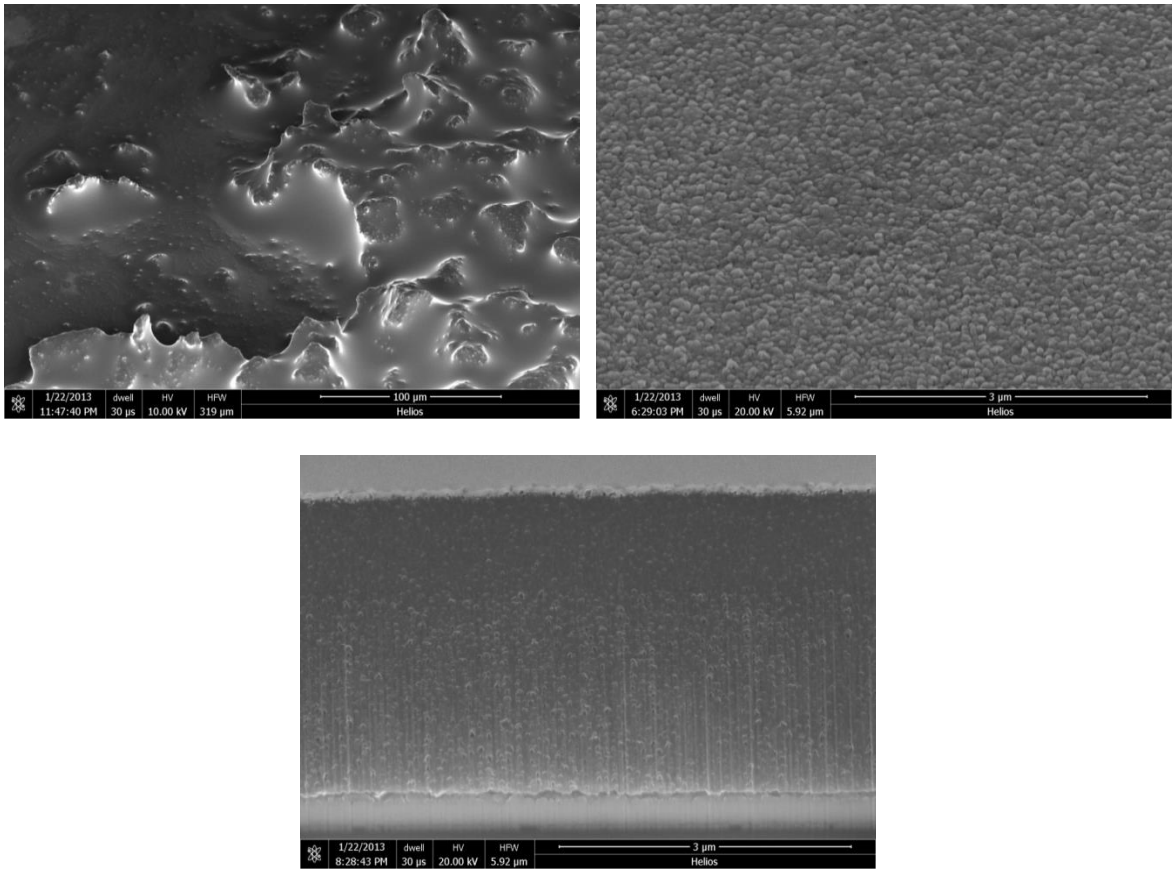

Figure 47. (Top) SEM micrographs of the top surface of ALD titania (left) and titania paste (right) electrodes. The ALD titania had a polymeric impurity present, coating the colloids. (Bottom) FIB cross-section cut on the titania paste electrode. Thickness is approximately 3 µm.

MSCS colloidal crystals were fabricated on the titania-coated FTO substrates using 480 nm diameter spheres with a pore size of 1.87 nm, followed by titania ALD, crystallization, and carbon removal. To confirm the annealed titania crystallized into the anatase phase, X-Ray Diffraction (XRD) was conducted on the annealed ALD titania (**Figure 48**). The amount deposited was 27 nm, as measured through ellipsometry on a flat, reference silicon wafer placed in the ALD chamber with the MSCS colloidal crystal. The as-deposited titania is confirmed to be amorphous (data not shown). The XRD in Figure 48 verifies that the titania does crystallize into

the anatase phase; through peak analysis, the crystallite size was found to be 16.6 nm. Additionally, the titania unit cell has dimensions of 3.7698 x 9.2678 Å, slightly smaller than the theoretical, unstrained unit cell of 3.784 x 9.515 Å. Interestingly, this corresponds to a 0.3% strain in the a direction, while a 2.6% strain along the c-axis.

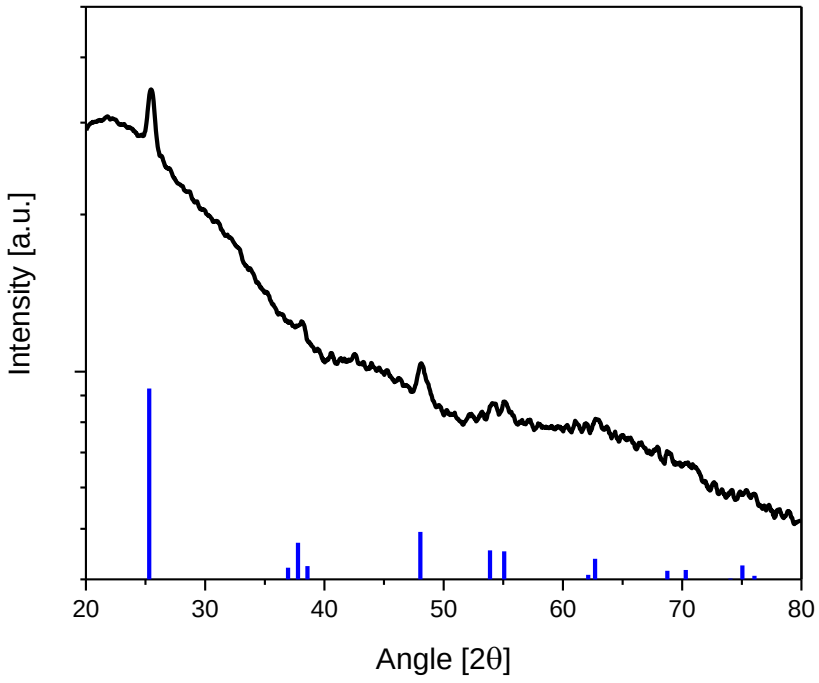

Figure 48. XRD spectra of ALD titania grown on carbon colloidal crystal after titania crystallization. The peaks correspond to the anatase crystal structure, with the PDF file shown in blue (PDF#04-002-2750).

The titania electrode templated via the MSCS colloidal crystal was assembled into a DSSC and the PV performance tested. However, the performance, especially the short circuit current (I_{SC}), was still extremely poor. To investigate this, FIB cuts and SEM imaging were done on the carbon-removed titania, shown in **Figure 49**. These show the titania infiltrates partway into the

carbon but do not fully replicate the mesoporous structure. Additionally, these micrographs show a thick shell of titania; this would prevent dye infiltration, which limits the number of photons absorbed, and thus severely decreases cell performance.

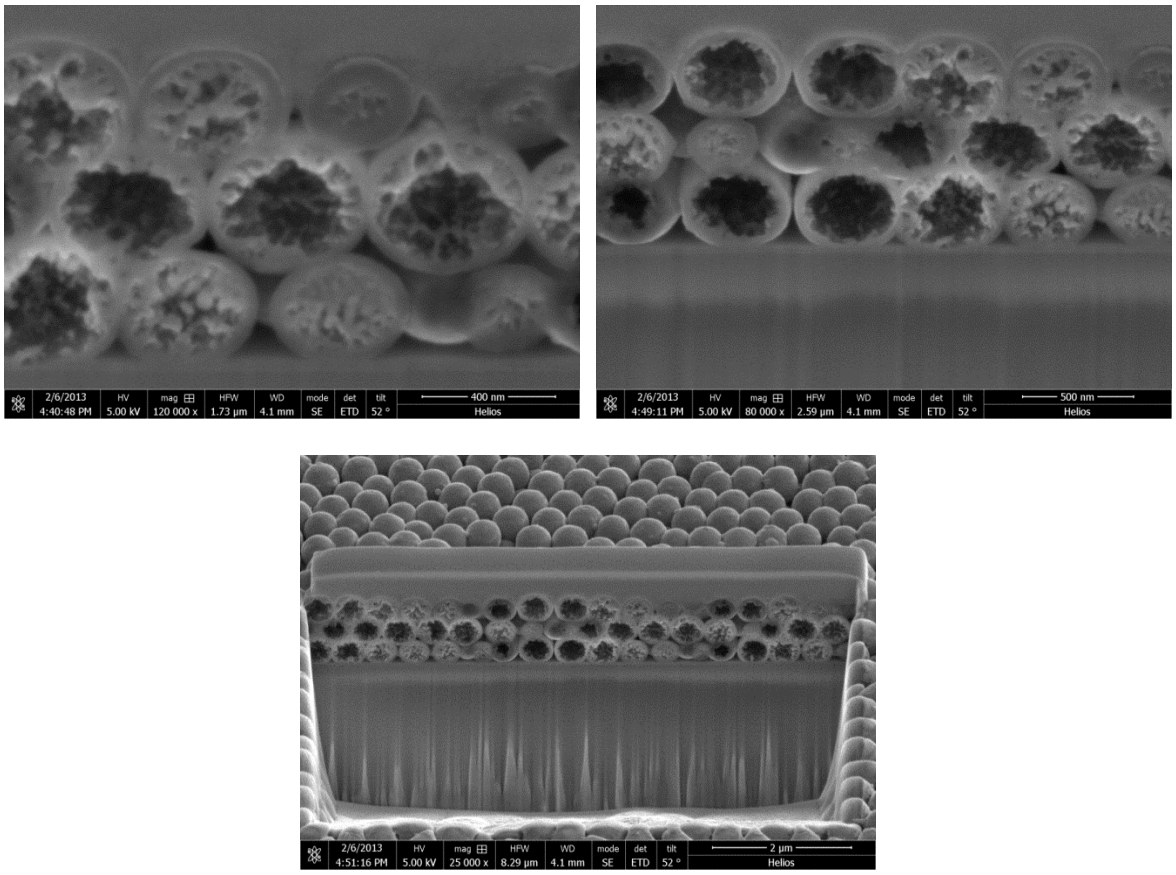

Figure 49. FIB cuts on carbon-removed titania. The titania infiltrates partway into the pore network of the carbon.

To test whether the dye is being adsorbed onto the titania electrode, UV-Vis measurements were conducted on the titania paste, used as a reference, and the ALD titania, both before and after 3-day immersion in dye solution (**Figure 50**). The titania paste shows a clear dip in the transmission where the dye absorbs (~550 nm). The ALD titania, however, does not show this

dip. Instead, the entire spectrum is suppressed due to scattering of the light. While scattering is preferred in the PV cell to increase the optical path length, dye must be present to absorb these. In the templated titania, there is no strong absorption from the dye, indicating low dye loading. FTIR measurements were also conducted on the templated titania (**Figure 51**) and show a main reflectance peak at ~1.0 μm with a magnitude of ~40%. Due to the increased density of states near the stop band edge [15, 44], this should improve the absorption of the red photons. This could be tailored through the use of differing diameters of MSCS.

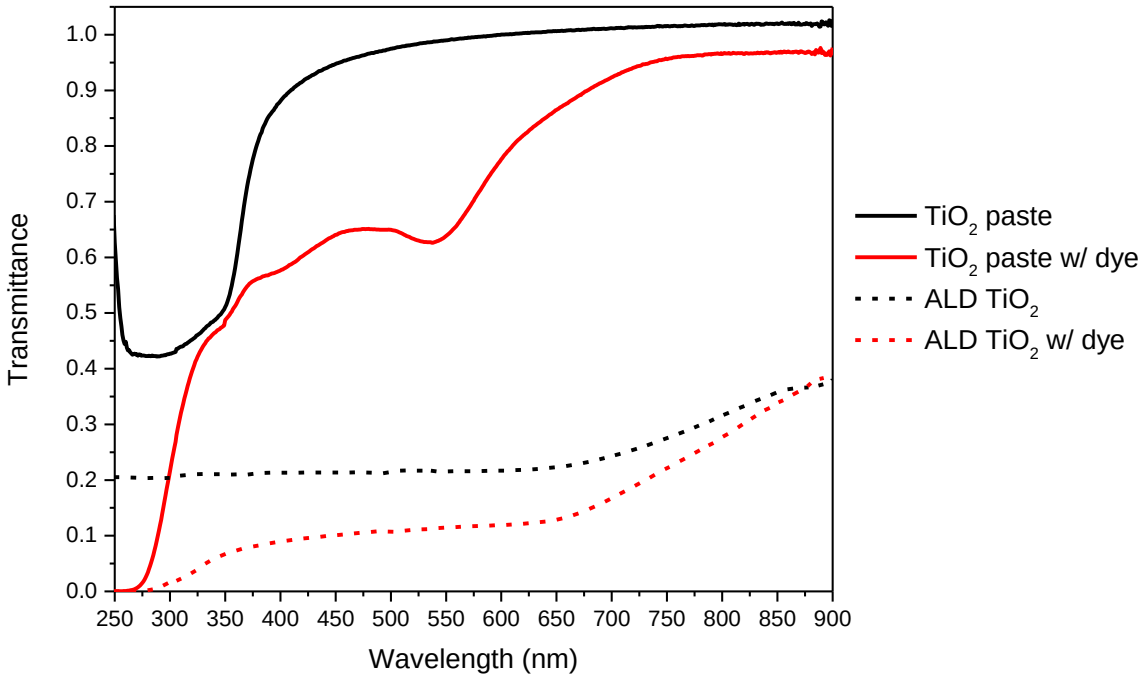

Figure 50. UV-Vis spectra of titania paste (solid lines) and ALD titania (dotted). The black indicates neat titania and red is the same sample after 3 days of immersion in dye solution.

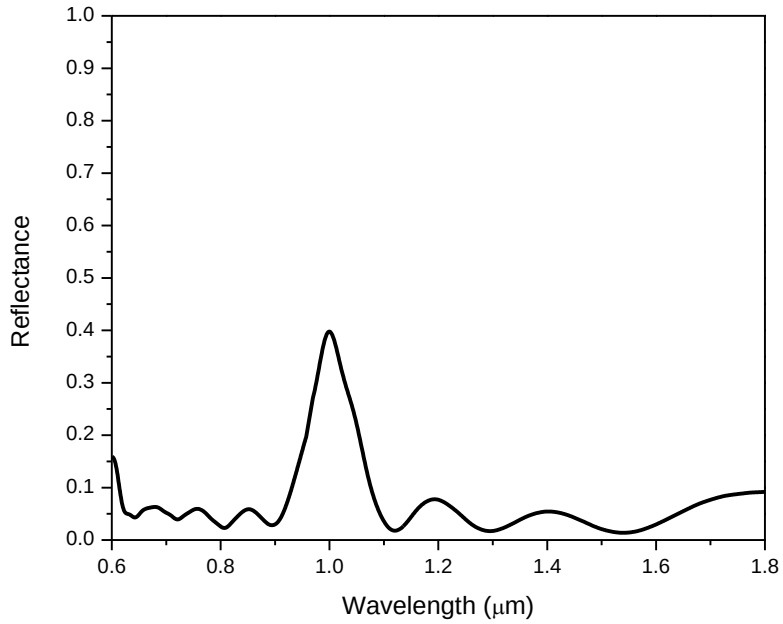

Figure 51. FTIR measurements of titania inverse opal. Main peak has a reflectance of ~40%.

5.3 Increasing Dye Adsorption in DSSC

It is believed that the poor PV cell performance is due to the lack of dye adsorption in the titania electrodes. By using larger pore carbon and decreasing the amount of titania deposited, higher surface area titania should be fabricated, allowing better dye adsorption. Additionally, conducting a brief reactive ion etch (RIE) to open the top titania should also allow better infiltration of the dye and electrolyte.

To increase dye adsorption in DSSC, a series of experiments were conducted to open the top surface (through RIE) of the titania while simultaneously decreasing the titania thickness. With a 17 nm titania thickness, opening the top surface did not show increased dye adsorption through UV-Vis measurements. Depositing thinner titania (approximately 10 nm, nominally) on the

larger pore MSCS (pore diameter = 4.3 nm) resulted in a titania inverse structure that had its integrity compromised through the RIE process, both before and after titania crystallization and MSCS removal. While the 10 nm titania deposited would overfill the pores, the experiment assumed the RIE process would allow the dye and electrolyte to penetrate where the MSCS colloids had vacated, and thus be able to infiltrate other shells through the packing of the MSCS template. RIE before titania crystallization and MSCS removal resulted in titania powder (after subsequent MSCS removal) with no clear structure, probably due to the ease of etching the amorphous titania; however, decreasing the RIE settings (e.g., power, time, etc.) had little effect. Conducting RIE after crystallization resulted in delamination, presumably from undercutting at the titania-FTO surface.

Decreasing the amount of titania deposited via ALD, approaching 1-2 nm, would allow a full replica of the mesopores. Additionally, the large pore MSCS could provide a large enough mesoporous template where, after the thin titania deposition, there exist mesopores within the titania shell. The requirements for this, however, are quite daunting: the largest mesoporous carbon used in this study had a diameter of 4.3 nm; the deposited titania would need to be less than 2 nm, as the titania deposits conformally, coating the walls of the mesopores evenly. If this is successful, however, the dye should be able to infiltration through inherent cracks in the inverse opal, removing the need for the RIE process. After numerous attempts, decreasing the titania thickness to only a few nanometers compromises the structure during and after carbon removal. All samples made with the extremely thin titania failed prior to cell fabrication. There does not appear to be an experiment window that allows effective use of the surface area provided by the mesoporous carbon.

5.4 Conclusions

High-quality colloidal crystals were able to be formed on the conductive FTO substrate after an initial coating of titania. Through ALD, titania was deposited onto the colloidal crystals, infiltrating the pores. After crystallization into the anatase crystal phase, the MSCS template was removed through a simple oxidation process. The PV characteristics showed a low short circuit current indicating low absorption of the incident photons. Low dye loading in the templated titania was revealed to be the source of the low photon absorption. Attempts to increase the dye adsorption by opening the top colloid surface through RIE or by depositing only a very thin coating of titania were unsuccessful. As such, MSCS colloidal crystals are not suitable as a template for DSSC applications.

CHAPTER 6

ENERGY STORAGE UTILIZING CARBON COLLOIDS AS TEMPLATES

In this chapter, the MSCS colloidal crystals are used as unique templates for energy storage, namely lithium battery anodes. CVD is done to deposit Si as the active material and, through an extension of recent work in the Abelson group, Fe (which is converted into Fe_3O_4 as the active material) into the mesoporous template. The Si-MSCS is immediately assembled into a half-cell for battery testing to minimize oxidation. The newly deposited Fe is fully characterized to ensure deep infilling and then oxidized to Fe_3O_4. By controlling the partial pressure, the Fe-MSCS can be oxidized to Fe_3O_4-MSCS without significant oxidation of the MSCS template. The MSCS template provides a conductive pathway with the active materials, Si and Fe_3O_4, confined in the mesopores, preventing any loss of material through pulverization. When cycled using an electrolyte that contains vinylene carbonate, the Si-MSCS anode could be cycled over 85 cycles. The Fe_3O_4-MSCS anode showed remarkable coulombic efficiency and revealed that the MSCS template decreased the charge hysteresis from 0.90 V for a conventional system, to 0.60 V at a rate of 0.2 C. Preliminary magnetic measurements were done on the Fe-MSCS composite, and a unique, dual superparamagnetic and ferromagnetic behavior was observed.

6.1 Introduction and Anode Fabrication

Secondary lithium-based batteries, due to the ever-increasing demand from numerous applications, including consumer electronics, space applications, and electric vehicles, have received considerable attention for a number of years [65, 110, 111]. Battery applications have a number of requirements, chief among these are long-term stability [112], high cycling rate [56, 110], and high capacity [113-116]. For good cycle life and long-term stability, the active

electrode material and its interface with the electrolyte (the solid-electrolyte interface, SEI) must be stabilized [117]. As cycling rate is typically limited by either electron extraction or Li-ion diffusion, higher cycling rate can be achieved via electrode design [56]. One such example is a conductive, and porous, electrode that can improve these limitations [56, 118]. To address issues of increased capacity, new active materials are necessary.

Typical commercial batteries utilize graphitic carbon as the anode, which has reasonable stability and cycling rate performance. The theoretical capacity of graphite is around 370 mA g^{-1} and stores Li ions via intercalation, up to the nominal formula LiC_6 [111, 119]. Other anode materials, due to their high theoretical capacities, have been investigated, including those based on Si [58, 120, 121], Sn [114, 122], and metal oxides [123-125]. Si, with a theoretical capacity of ~4,200 mA hr g^{-1}, is an exceptional high-capacity anode material. However, during lithium insertion, the Si expands significantly, up to 400% volumetrically, with a corresponding contraction upon lithium extraction. The stress associated with this large volumetric change causes cracking and pulverization, leading to rapid capacity decay [120]. To alleviate the induced strain, electrode designs have utilized Si in the nanometer range with sufficient space to accommodate the expansion. Electrode design can also improve the electron extraction, typically employing a porous, conductive scaffold [58, 113], a carbon coating [126, 127], or the addition of carbon black [128]. The solid-electrolyte interface (SEI) stability is another challenge in the silicon anode and has not been effectively addressed; however, mechanical clamping via a SiO_x protective layer [129] and the addition of vinylene carbonate (VC) to the electrolyte [130, 131] have promise. Interestingly, not all reports indicate the VC additive improves performance; one report, with an electrode containing nano-Si, carbon black, and cellulose binder, obtained

optimal cyclability with a VC-free electrolyte [117]. This suggests that Si-electrolyte SEI stabilization using VC is dependent upon the numerous possible chemistries, of which the polymer binder-electrolyte reaction plays a pivotal role.

Another promising anode candidate is iron oxide, Fe_3O_4, due to its high theoretical capacity (upwards of 1000 mA hr g^{-1}), low cost, and low toxicity, in addition to it being environmentally benign [110, 132]. Unlike the Si-Li intercalation reaction, Fe_3O_4 stores energy primarily through a conversion reaction of $Fe_3O_4 + 8Li^+ + 8e^- \rightarrow 3Fe + 4Li_2O$. Challenges with Fe_3O_4 include its low conductivity, resulting in capacity fade and poor calendar life, and the large charge hysteresis, resulting in energy and coulombic efficiency loss [110]. Similar strategies employed with Si active materials can be utilized to improve conductivity: addition of carbon [133], utilization of a conductive scaffold [110, 123, 124] and carbon nanotubes [132], and "coating" by graphene encapsulation [125, 134]. Due to the conversion reaction, charge-discharge hysteresis remains a challenge. Prominently, this hysteresis is due to an activation barrier for the reduction and oxidation reactions, directly linked to the size and uniformity of the Fe_3O_4 active materials formed after the first discharge [110]. Several groups have exploited Fe_3O_4 nanoparticles to decrease this barrier; however, particle aggregation is still a challenge [123, 125, 132, 134, 135]. One group in particular had success in hysteresis reduction: an anode comprising of Fe_3O_4 nanoparticles decorated on graphene sheets was compared to an anode with only Fe_3O_4 nanoparticles [135]. The average reduced hysteresis, reported as the voltage difference between the charge and discharge curves, is approximated to be 0.7 V, with the average hysteresis of the pure Fe_3O_4 anode approximately 0.9 V.

Reported here is a novel anode system utilizing monodisperse starburst carbon spheres (MSCS) as a scaffold for active materials, namely Si and Fe_3O_4, in lithium ion battery anodes. The MSCS can be fabricated into a colloidal crystal structure, allowing electrolyte and ion diffusion between the spheres. With their mesoporous nature, the MSCS offer unique templating opportunities, as active materials can be deposited into the mesopores via static chemical vapor deposition (sCVD); the carbon structure then acts as a confining layer and individual current collectors. By utilizing an electrolyte containing VC, Si anodes show excellent coulombic efficiency while retaining over 1000 mA hr g^{-1} capacity over 85 cycles at a cycling rate of 0.33 C. The Fe_3O_4 anodes were synthesized in a two-step process where, after sCVD of Fe, a partial oxidation occurred. The anode showed good performance over 40 cycles and maintained a capacity of ~700 mA hr g^{-1}. Importantly, by confining Fe_3O_4 only in the mesopores, the charge hysteresis dropped significantly to 0.60 V; increasing the amount of active material so that the Fe_3O_4 is no longer confined in the mesopores raised the hysteresis to 0.75 V. This low hysteresis decreases the energy loss, resulting in the high coulombic efficiency.

Monodisperse starburst carbon spheres (MSCS) were synthesized [77] and oxidized [1] as previously reported. The MSCS structure is a wheel-like arrangement of carbon "spokes" due to the templated synthesis. The specific MSCS used in the final anode have a diameter of 480 nm, a polydispersity index (PDI) of 1.039, a pore volume of 1.47 mL g^{-1}, and a specific surface area of 1190 m^2 g^{-1}. Most importantly, the average pore size, measured and calculated via nitrogen isotherms, was 4.29 nm, with a distribution between 2 and 8 nm. By utilizing the large pore MSCS, sCVD of active materials can easily infiltrate deep into the mesopores, increasing the volumetric density of the anodes. After cleaning and modification, substrates were placed in an

ethanolic solution of MSCS for scaffold fabrication. Of note, unlike the previous work on the MSCS colloidal crystal optics [1], the MSCS here are solely utilized as an anode scaffold, so perfect order is not necessary. The MSCS-coated substrates were then put into a reaction chamber and heated under vacuum to drive off any residual moisture in the mesopores. After cooling to room temperature, the precursor, either disilane (Si_2H_4) or iron pentacarbonyl ($Fe(CO)_5$), was introduced into the reaction chamber, sealed, and heated to drive the reaction. The Fe-MSCS was then oxidized to Fe_3O_4-MSCS by heating under partial vacuum (10 mbar). Both the Si-MSCS and the Fe_3O_4-MSCS were then tested as anodes in a half-cell (coin cell configuration) with lithium metal as the counter electrode.

For MSCS adhesion on the conductive substrates, a new approach is need as, unlike the DSSC work, a layer of semiconductor oxide will increase the voltage drop in the electrode, making an inferior device, or preventing charge collection altogether. By using a gold-coated substrate, a self-assembled monolayer (SAM) of sodium 3-mercapto-1-propanesulfonate was deposited (5 mM solution in H_2O, overnight). The sulfur group binds strongly to the gold surface while the sulfonate group provides the necessary, negative charge. This allows for a possible salt bridge between the carbon and the sulfonate to form. Another option that was ultimately employed was switching to tungsten substrates, as this provides the necessary surface charge [58]. Both the SAM treatment of the gold substrates and using tungsten films allowed MSCS colloidal crystal growth.

6.2 Silicon CVD for Battery Applications

While there are numerous studies on silicon for Li-ion anodes, several advantages exist for using CVD grown silicon with the MSCS colloidal crystal as a template. The MSCS create a nanostructured electrode that will allow efficient charge collection, assuming the carbon is conductive enough. 4-point probe measurements and an order of magnitude calculation show the voltage drop through the MSCS template will be only ~25 mV for a 10 μm film. Of note, the 4-point probe measurements were conducted on a drop-cast MSCS film on a glass substrate. Due to the fragile nature of the MSCS structure, the probe points broke through and made contact with the underlying substrate, even with diligent and careful lowering of the probe. As such, it is believed that the resistivity measured is erroneously high due to the substrate. Regardless, this voltage drop, even the high estimation, is sufficiently low for battery applications. By using carbon as the current pathway, significant weight reduction can be realized compared to conventional metal foils. With the nanostructure of the MSCS, any nanoparticle of silicon that does break off during cycling has a high probability of striking and attaching to another carbon colloid. Thus, capacity fade due to pulverization of the silicon and loss of electrical contact is diminished. A drawback, however, manifests in the fragility of the carbon colloidal crystal. Unlike silica colloidal crystals where the colloids have covalent bonds binding them together and to the substrate, the MSCS have only weak van der Waals attraction. Conventional anode construction uses a slurry of graphitic carbon, carbon black, and a polymer binder (typically polyvinylidene difluoride, PVDF) cast onto the substrate current collector. Due to the processing conditions required, i.e., silicon CVD occurs after MSCS colloidal crystal formation, the polymer binder cannot be used during MSCS colloidal crystal fabrication.

Initially, a MSCS colloidal crystal was fabricated on a sulfonated thiol-treated gold-chrome coated glass substrate with low-pressure silicon CVD conducted to deposit only a thin layer into the MSCS mesopores. Placing the anode in a jar cell, it was cycled against lithium metal in organic electrolyte (ethylene carbonate, dimethyl carbonate, & lithium perchlorate, EC:DMC:$LiClO_4$). However, due to its fragility and lack of binder, the MSCS colloidal crystal anode severely delaminated. With the anode set perpendicular in the jar, any colloid that delaminates falls into the electrolyte, eliminating any chance of electrical reconnection. Instead, by switching to a coin cell configuration, the MSCS colloidal crystal can be clamped by the spacer, allowing electrical reconnection if colloids delaminate. To determine the capacity and round-trip efficiency, coin cells containing the Si-MSCS anode were cycled at 0.05 C in the voltage window of 0.1 to 2 V, shown in **Figure 52**. Of note, the voltage window for typical silicon anodes drops to 0.05 or 0.01 V [58, 120]; however, due to using gold-coated slides as the electrodes, 0.1 V was chosen to limit the lithium-gold alloying processes that occur at 0.130 and 0.075 V [136]. The MSCS used had a pore size of 4.29 nm, which allows easy infiltration by the silicon CVD. The silicon-based capacity is similar to reported values at 3450 mAh g^{-1} for coin cell 1 and 3140 mAh g^{-1} for coin cell 2, and, after the first cycle, the round-trip efficiency is above 90%. The sharp drops in the capacity during testing are assumed to be instrument error, as the raw data shows a charge/discharge switch before reaching the voltage set points. Samples were also cycled against lithium metal at approximately 1 C. Unfortunately, the capacity dropped significantly after each cycle, with evidence that the carbon was delaminating from the substrate. To combat this, Si anodes can be cycled at much slower rates while delivering significant power due to their high capacity [58].

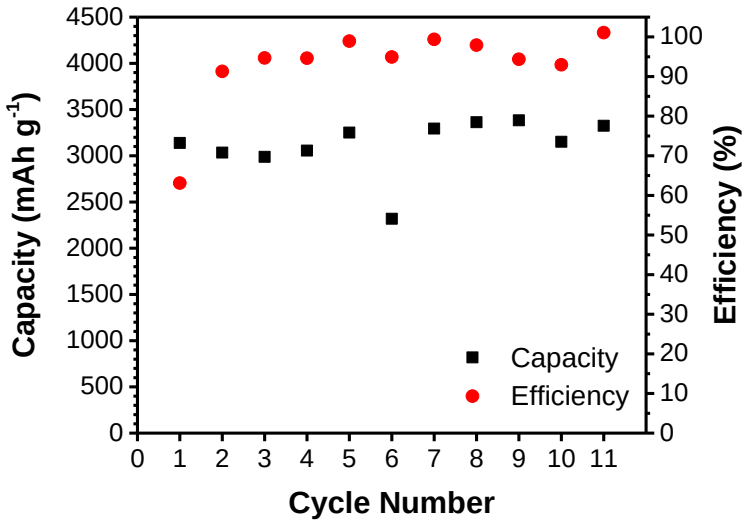

Figure 52. Si-MSCS anode coin cell cycled at 0.05 C on gold-coated substrates.

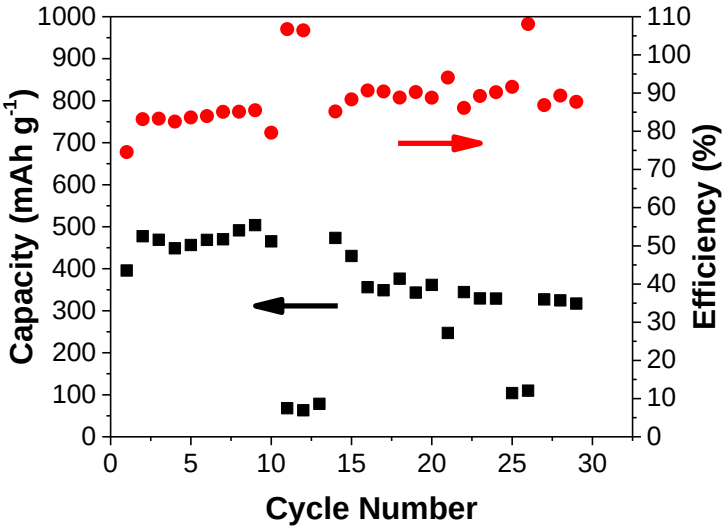

Figure 53. Anode cycled at 0.125 C consisting of only MSCS (i.e., no silicon deposition).

Additionally, cycling a carbon anode will provide a baseline capacity as well as determine if the silicon expansion is the cause of delamination. The carbon anode was cycled at 0.125 C for 30 times (**Figure 53**). The capacity is fairly constant, aside from a drop around cycle 16 (extreme

low points are most likely experimental or equipment error). Unfortunately, the roundtrip efficiency reached only 90% after 30 cycles. However, this shows that the MSCS template can withstand numerous cycles, allowing further use in the Si-MSCS anode.

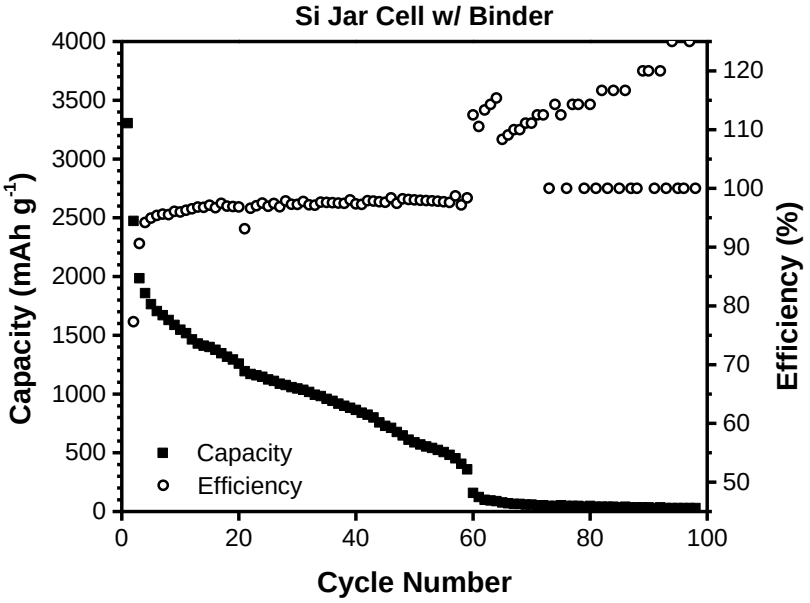

Figure 54. Cycle performance on Si-MSCS jar cell with binder at 0.6C.

To determine the cycle capability, a new setup was attempted using the jar cell. In this, PVDF binder in N-Methyl-2-pyrrolidone (NMP) was drop-casted onto the silicon-MSCS anode; as the silicon has already been deposited, blocking the MSCS pores is no longer a concern. The number average molecular weight of the PVDF is 71,000 g mol^{-1} (PDI of 2.5), with a radius of gyration approximately 4.2 nm, assuming theta solvent conditions. With this, the polymer should slightly infiltrate into the mesopores (vp = 4.29 nm, pore distribution between 2-8 nm). 100 cycles at 0.6C on this anode configuration shows a steady and significant capacity drop, even though the round-trip efficiency was over 90% after two cycles and maintained 97-98% through 60 cycles

(**Figure 54**). A 0.6 C rate was chosen to obtain data in a timely fashion; however, decreasing the C rate may improve the capacity retention during cycling as other cycle performance studies have been conducted at 0.1C [120, 137], and 0.3C [58]. Post-cycling, top-view SEM was conducted (**Figure 55**); these show a film, be it SEI or binder, covering the colloidal crystal anode with large, 10 μm diameter holes surrounded by nano- and micro-particles. These may be silicon-coated MSCS that have pulverized, PVDF binder, or even SEI formation on one or both; without elemental analysis, confirmation is impossible.

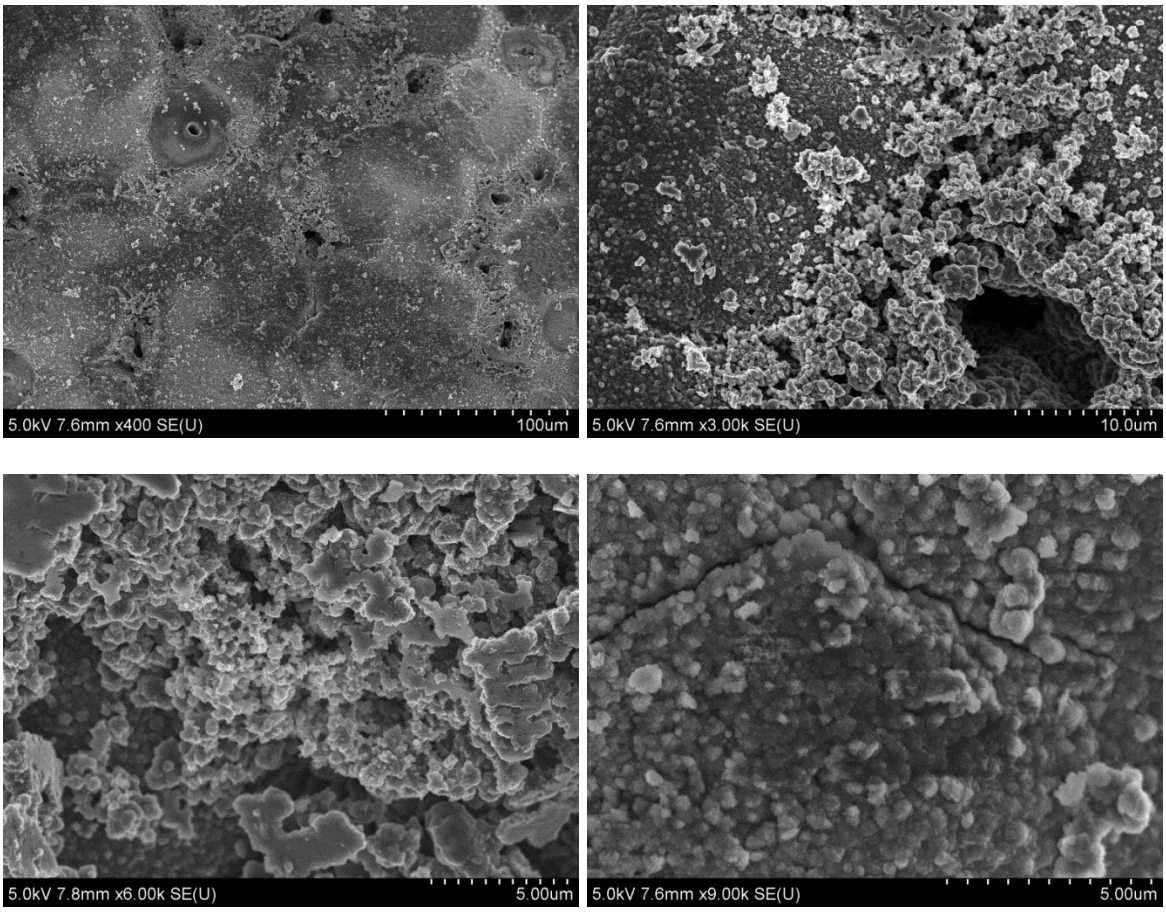

Figure 55. Post-cycling SEM (top-view) of silicon-MSCS coated with binder. Anode was cycled 100 times at 0.6 C.

To improve performance and understand this unique system, three routes were taken: (i) decreasing silicon loading, (ii) determining if the PVDF binder is appropriate, and (iii) switching from gold-coated substrates. Decreasing the silicon loading will allow for silicon to be deposited inside the mesopores but not create a shell around the colloids. A cross-sectional FIB image on a virgin anode shows faint outlines of a silicon shell, indicating that the performance may be due to a silicon film (which is easily pulverized), rather than discrete particles inside the mesopores (**Figure 56**). If a silicon shell has formed, decreasing the deposited silicon can be done by changing the CVD reaction conditions. While PVDF binder is commonly used, researchers have had mixed success; one study with an anode consisting of a silicon nanowire array showed poor stability with PVDF but respectable stability with sodium alginate binder [137]. Even in the preliminary studies above, coin cells without the binder show adequate capacity, at least in the first 10 cycles. Longer cycling by the coin cell may determine that the binder is not needed, due to the clamped configuration. If the binder is necessary, an increase in the molecular weight of the binder will prevent infiltration into the mesopores, allowing silicon to expand unhindered. Unstable SEI formation, as some papers suggest the anode failure mechanism [120, 121, 137], could be potentially solved with the correct electrolyte and binder combination; if not, the most promising technique is a thin oxide shell deposited via ALD [138]. As stated earlier, gold alloys with lithium at low potentials, proving difficult to use in anodes. Studies have shown that gold interferes with silicon anode performance (loss of capacity, rate, and fade) [137] as well as potentially delaminating when used in thicknesses of 10 nm or greater [136]. Eliminating gold from the anode will undoubtedly improve performance. A promising candidate is a tungsten foil substrate, as they showed promise in previous studies [58].

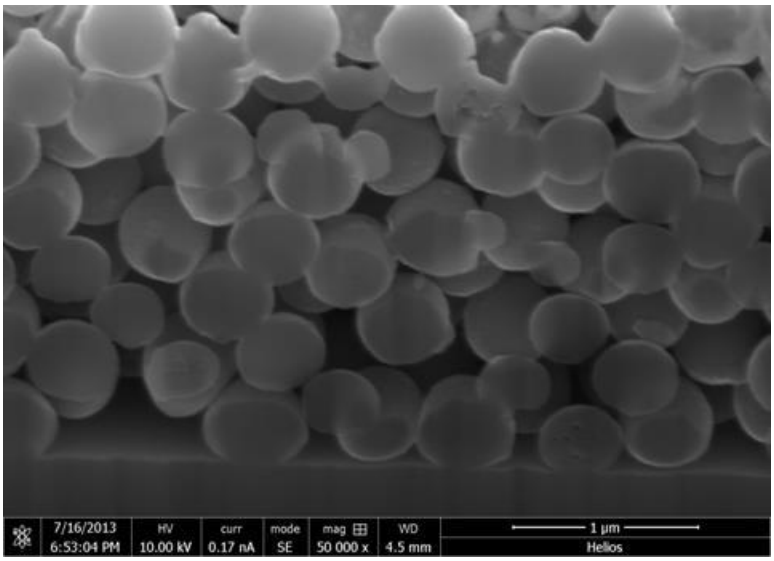

Figure 56. FIB cut on virgin silicon-MSCS anode.

TEM imaging was also conducted on the low-pressure silicon CVD on carbon for Li-ion batteries (**Figure 57**). Due to the colloid contrast, i.e., darker in the center than the edges, one can deduce that there is silicon deposited inside the mesopores, rather than just the shell. This is expected, as the results from the 1.87 nm pore MSCS templating also showed Si infiltration [1]; these MSCS colloids for battery applications had mesopores with a diameter of 4.3 nm. Thicker electrodes, for more practical applications, were attempted by first depositing silicon on a carbon colloidal crystal, then redispersing the colloids in a binder solution. However, the small quantity of carbon-silicon sample does not allow this. Instead, thicker electrodes would need to be created via a Xia Cell or similar method.

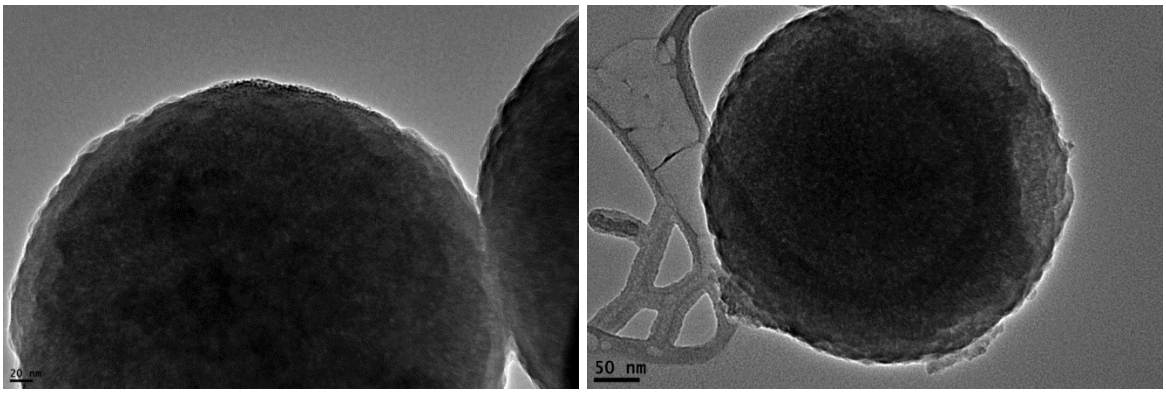

Figure 57. TEM images of the low-pressure silicon CVD on mesoporous carbon colloids.

To combat the gold delamination, tungsten substrates were utilized, providing the necessary anionic surface charge for colloidal crystal formation [58]; and cut to fit into the coin cell configuration. A cleaning process using concentrated KOH in ethanol makes the tungsten substrate suitable for high-quality carbon colloidal crystal growth, followed by a low-pressure silicon CVD. These were made into coin cells with a standard electrolyte (1.0 M $LiPF_6$ in EC/DEC/DMC (1:1:1 by vol)) and cycled at different C rates (**Figure 58**). While the efficiency is good (99% at greater than 1 C rates), the capacity fade is significant; returning to the initial 0.065 C rate after 40 cycles resulted in a capacity loss of nearly 50%. To improve this, additional processing of the Si CVD samples can be employed. As the Si CVD is non-selective, Si will be deposited on the back and exposed top of the tungsten substrate. This Si will not be confined in the carbon pores and, as such, will be more subjected to the pulverization due to volume expansion. In order to remove this Si, RIE has been conducted with a Kapton film as a mask. Additionally, incorporating incorporate vinylene carbonate (VC) as an additive into the electrolyte has been shown to improve performance in a number of studies [130, 131].

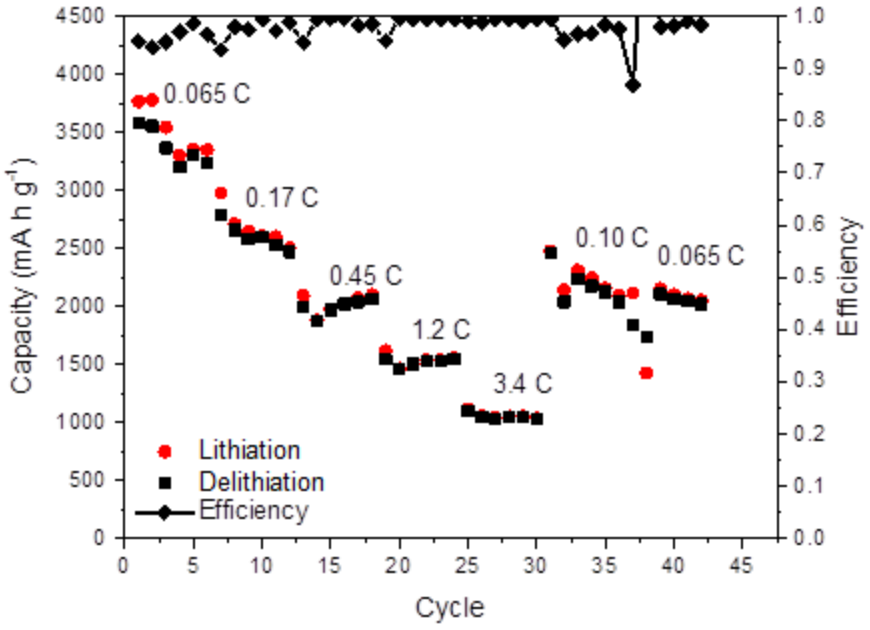

Figure 58. Si-MSCS coin cell fabricated with the standard electrolyte (1.0 M $LiPF_6$ in EC/DEC/DMC (1:1:1 by vol)).

By modifying the electrolyte with the addition of VC, totaling approximately 5 wt%, the performance was significantly improved. **Figure 59** shows the rate performance of the Si-MSCS with the VC electrolyte. The Si-MSCS anode was fabricated using experimental conditions to underfill the structure, allowing the Si to deposit into the mesopores but not creating a thick overlayer on the MSCS. This is a two-fold imperative: the mesoporous structure of the MSCS allows for the volumetric expansion of the Si during lithiation through the rearrangement of the MSCS "spokes." Additionally, keeping the Si within the mesopores provides an intimate connection and allows easy electron extraction and transport. Due to the large surface area and pore volume of the MSCS, the mass ratio of the Si to MSCS was 5:1, signifying the majority of the capacity obtained was provided by the Si. During the first 10 cycles, when the cycling rate

was 0.07 C, there is a steady decline in capacity with the coulombic efficiency between 90 and 95%. However, after the tenth cycle, the cycling rate was increased to 0.25 C with the coulombic efficiency increasing to 99%, which was maintained throughout 85 cycles, even when the rate was further increased to 0.33 C. Also of importance is that the Si-MSCS anode, after rapidly losing capacity in the first 10 cycles, stabilizes its specific capacity at approximately 1680 mA hr g^{-1} during the cycling at 0.25 C. At 0.33 C, the capacity drops slightly but again stabilizes through 85 cycles, ending with a capacity of 1090 mA hr g^{-1}. In this Si-MSCS system, the anode design allows for volumetric expansion and, even if partially pulverized, an extended mesoporous network allows efficient electron extraction and transportation. Since there is no binder in the Si-MSCS anode system, the SEI stability could be easily addressed through the addition of VC to the electrolyte without concern of secondary reactions.

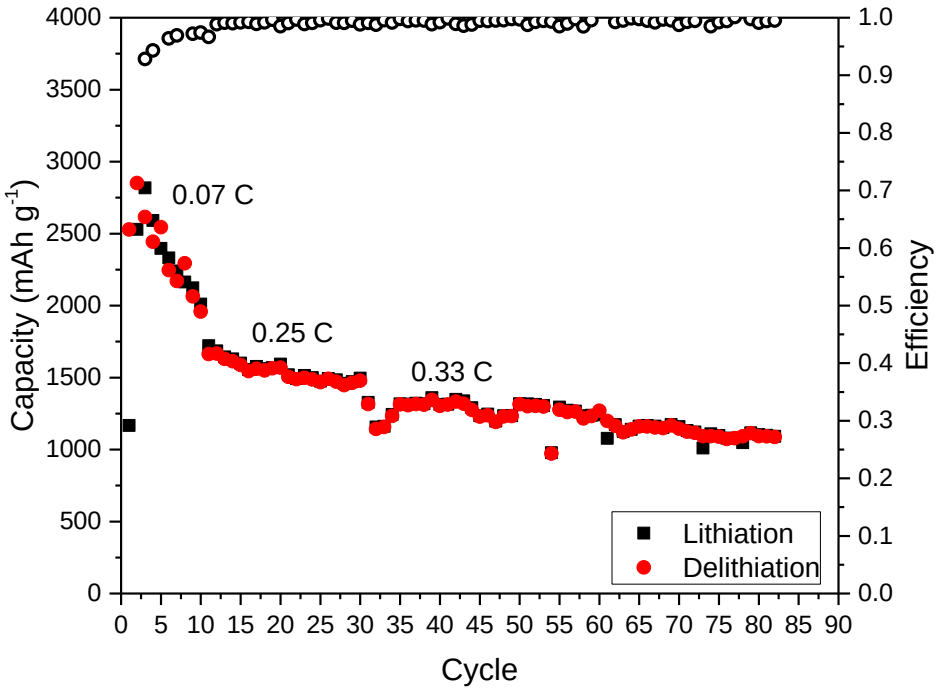

Figure 59. Cycle performance of Si-MSCS anode vs. Li using VC containing electrolyte.

6.3 Iron CVD for Battery Applications

While the Braun group has extensively utilized sCVD of Si with conformal deposition [139], only a few reports show Fe deposition with $Fe(CO)_5$ as a precursor; these are fabricated using the traditional flow CVD and are analogous with rough and/or discontinuous films [140-142]. This work takes advantage of the recent advancement in sCVD of Fe, where a conformal, continuous Fe film can be deposited [143]. Unlike Si sCVD where the precursor is a gas that can be charged to a given pressure, $Fe(CO)_5$ is a liquid at room temperature with a high vapor pressure of ~33 mbar. As such, a sCVD system pumps to vacuum, seals off the vacuum line, and allows the chambers to reach equilibrium, which introduces the precursor. Much to the advantage of this system, it has been shown that there is strong selectivity of the Fe deposited between silicon dioxide (SiO_2) and tungsten, with a 100% selectivity to the SiO_2 [141]. As the reaction chamber is glass, the tungsten substrate should remain Fe free, allowing investigation into the role of the mesoporous MSCS. Initially, a MSCS colloidal crystal, 479 nm diameter MSCS, pore diameter of 1.87 nm, was used as the iron template. After diffusion of the $Fe(CO)_5$ vapor, the samples were heated at 150 °C for 10 hr, depositing iron that reached the pinch-off point of 37 nm (**Figure 60**).

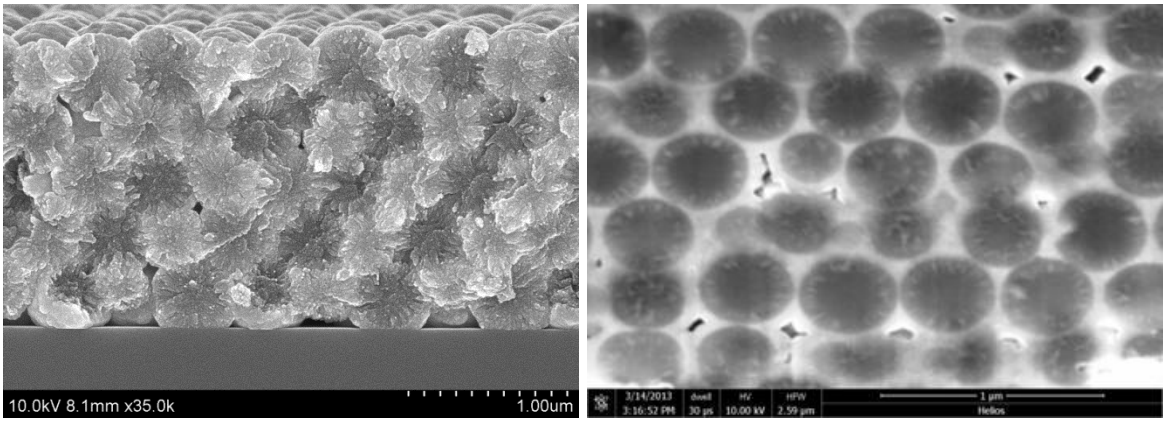

Figure 60. Fe static CVD on MSCS colloidal crystal. Left: fracture surface, right: FIB cross-sectional cut.

Preliminary work done by a collaborator has shown that depositing iron on silica results in a composition of 96 at% Fe, 2.5 at% O, and 1.5 at% C, as measured by XPS [143], eliminating concerns of oxidation during deposition. The fracture surface and FIB cut in Figure 60 show the deep infilling of the iron, even in the 1.87 nm pores. Additionally, XRD has been conducted on the Fe-deposited MSCS colloidal crystal (**Figure 61**), with the peaks corresponding only to metallic Fe. Analyzing the peaks, the crystallite size was determined to be 11.4 nm; the large crystallite size compared to the pore diameter is similar to the phenomenon shown by the hafnia. Additionally, as the iron is not confined to the pores, the interstitial sites in the colloidal crystal can support large iron crystallites. Fe CVD was then conducted on larger pore diameter carbon (4.3 nm) to allow a thin shell to be deposited in the pore. XRD on the larger pore (4.3 nm) shows crystallite size to be slightly larger at 12.9 nm. Additionally, the XRD data on iron-coated 4.3 nm mesopore carbon showed an additional peak at 43° 2θ (**Figure 62**).

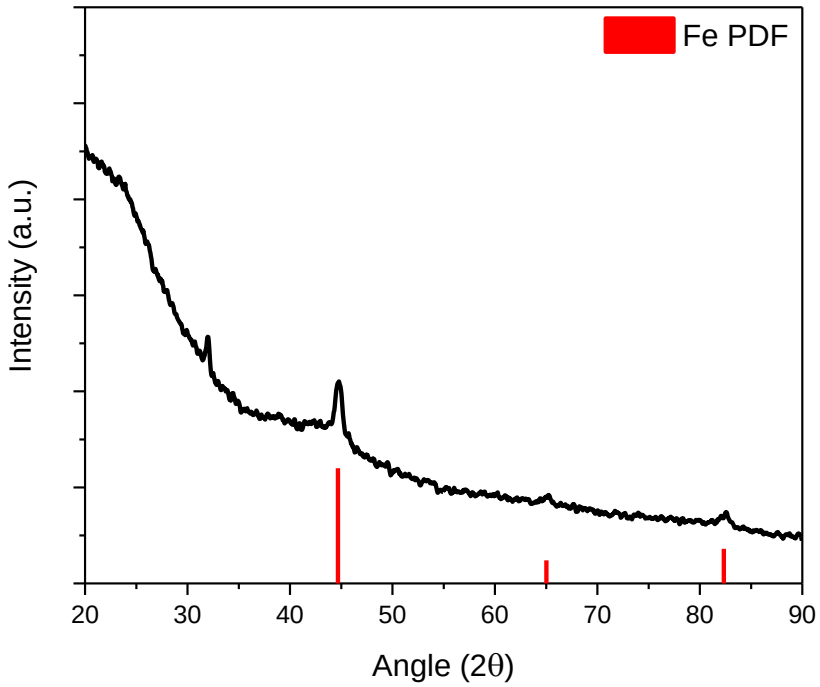

Figure 61. XRD on Fe deposited carbon colloidal crystal. Peaks correspond to α-iron, BCC symmetry (PDF#00-006-0696).

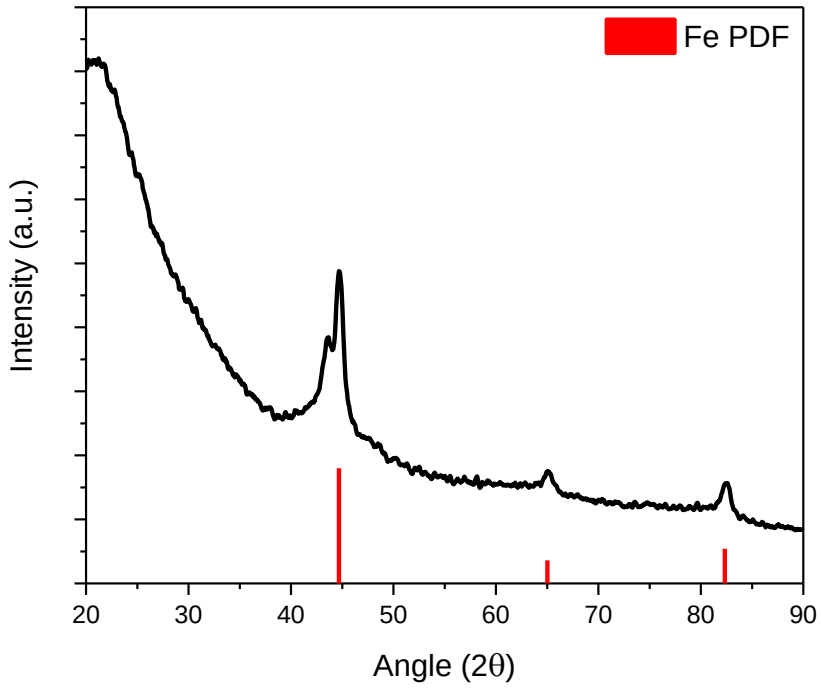

Figure 62. XRD data on CVD-grown iron on carbon colloidal crystal with 4.3 nm mesopores. Bottom shows the PDF card file for iron (PDF#00-006-0696).

Interestingly, the Fe CVD has shown near-100% deposition selectivity by depositing on the MSCS colloidal crystal, but not on the glass sidewalls of the reaction chamber. To investigate this, two colloidal crystal samples, one carbon and one silica, were placed in the reaction chamber. After the 10 hr CVD run was complete, the silica colloidal crystal had sparse Fe nanoparticles decorating the silica colloids (**Figure 63**). However, Fe deposited readily on the carbon colloidal crystal, infilling the colloidal crystal over 20 μm thick, presumably due to Fe-MSCS surface reactions.

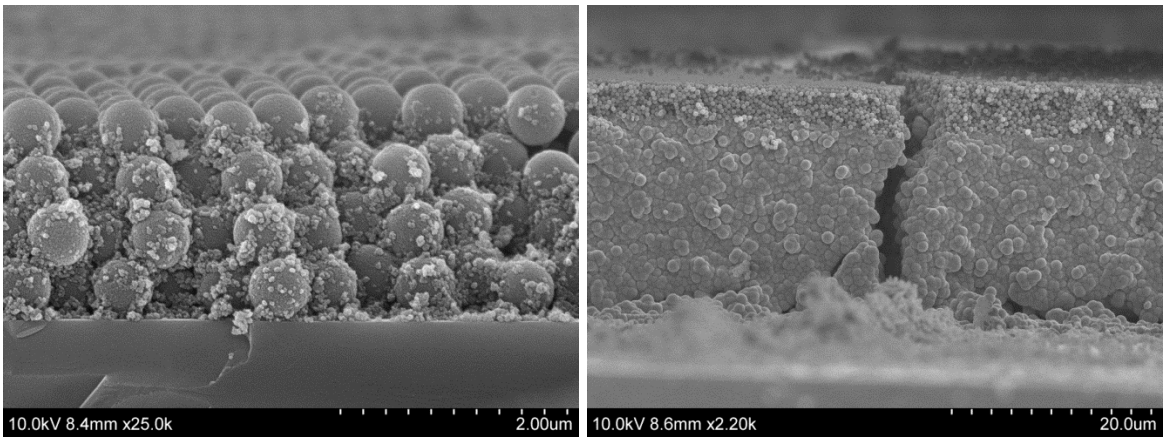

Figure 63. SEM of the silica colloidal crystal (left) and the carbon colloidal crystal (right) after Fe CVD for 10 hours at 150 °C.

To combat the thick iron deposition, the selectivity shown between glass and carbon was utilized. Increasing the carbon content would allow for thinner deposition (more area to deposit onto, similar starting precursor content). This is in direct contrast to the silicon CVD, as the silicon deposits more uniformly across numerous materials. By introducing a second sample in the reaction chamber, effectively doubling the surface area for the Fe deposition, and having a two-minute diffusion, thin iron deposits in "island" configurations were observed (**Figure 64**). To determine the infilling of iron inside the carbon mesopores, a FIB cut was conducted on the Fe-C composite. To deposit iron, a shorter (30 sec.) precursor ($Fe(CO)_5$) diffusion was utilized after pumping down to 10^{-6} mbar; two carbon colloidal crystal samples were in the reactor. After sealing, the reactor was placed in a furnace having a heating process of 1 °C/min ramp to 150 °C, hold for 1 hour, and a 0.3 °C/min cool. The fracture cross-section was similar to Figure 64; however, **Figure 65** shows the FIB cut, along with a contrast-enhanced portion. Due to the two-toned contrast on the cut, one can conclude the iron deposits through the pores.

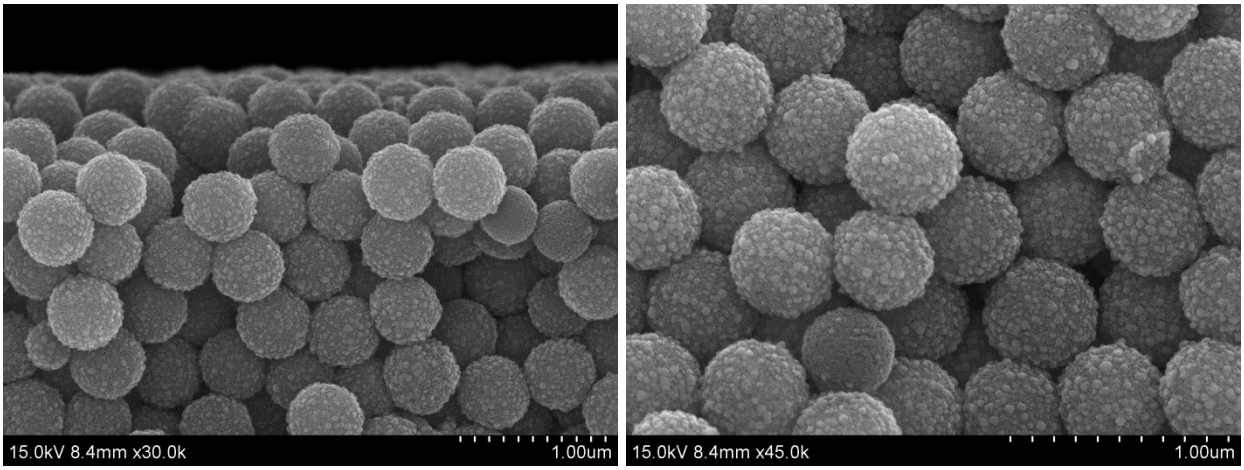

Figure 64. Thin "islands" of iron deposited on carbon opal utilizing two samples in the reactor and a 2-minute precursor diffusion (150 °C, 1 hr, heating).

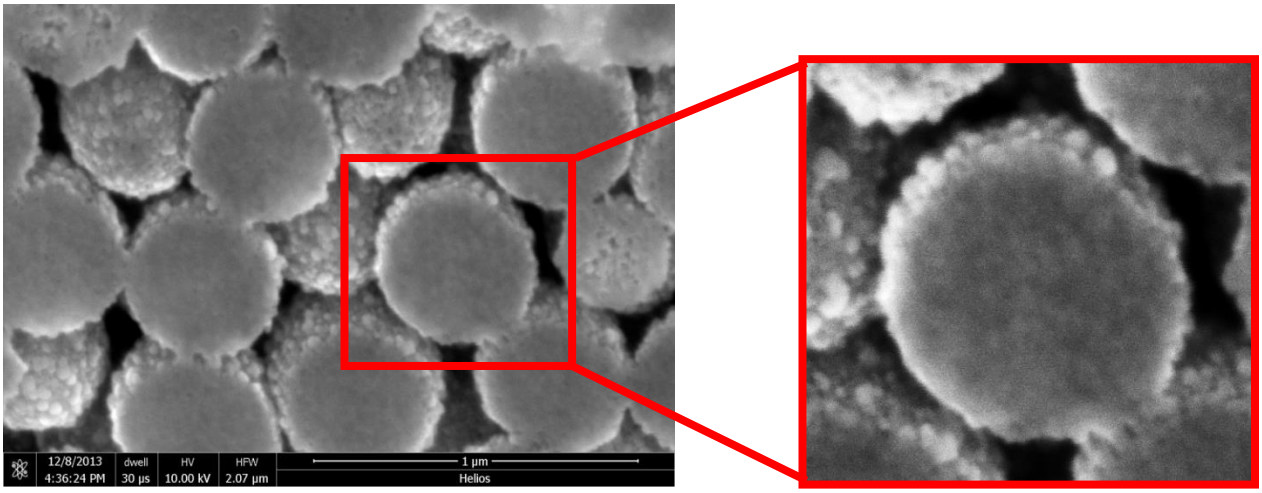

Figure 65. FIB cut of the Fe-C composite; two samples were placed in the reactor with a 30-second precursor diffusion (150 °C, 1 hr, heating). Inset is a contrast-enhance portion, showing the two-toned iron-carbon composite.

To further verify Fe infiltration, a focused ion beam (FIB) lift-out was performed; **Figure 66**(a) shows the scanning electron microscopy (SEM) image of the Fe-MSCS composite, Figure 66(b) and (c) are transmission electron microscopy (TEM) and scanning transmission electron

microscopy (STEM) images, respectively. An electron energy loss spectrum (EELS) was taken on the inset of Figure 66(c) and shown in Figure 66(d); the peaks at 700 and 713 eV correspond to the Fe-L_3 and Fe-L_2 lines (i.e., excitation of Fe $2p^{3/2}$ and $2p^{1/2}$ electrons) [144, 145], verifying Fe deposition into the center of the MSCS. By changing the diffusion and heating time, along with the amount of MSCS templates, the thickness of the Fe can be controlled. For this sample, a precursor diffusion time of 30 seconds and heating at 150 °C for 1 hour were used.

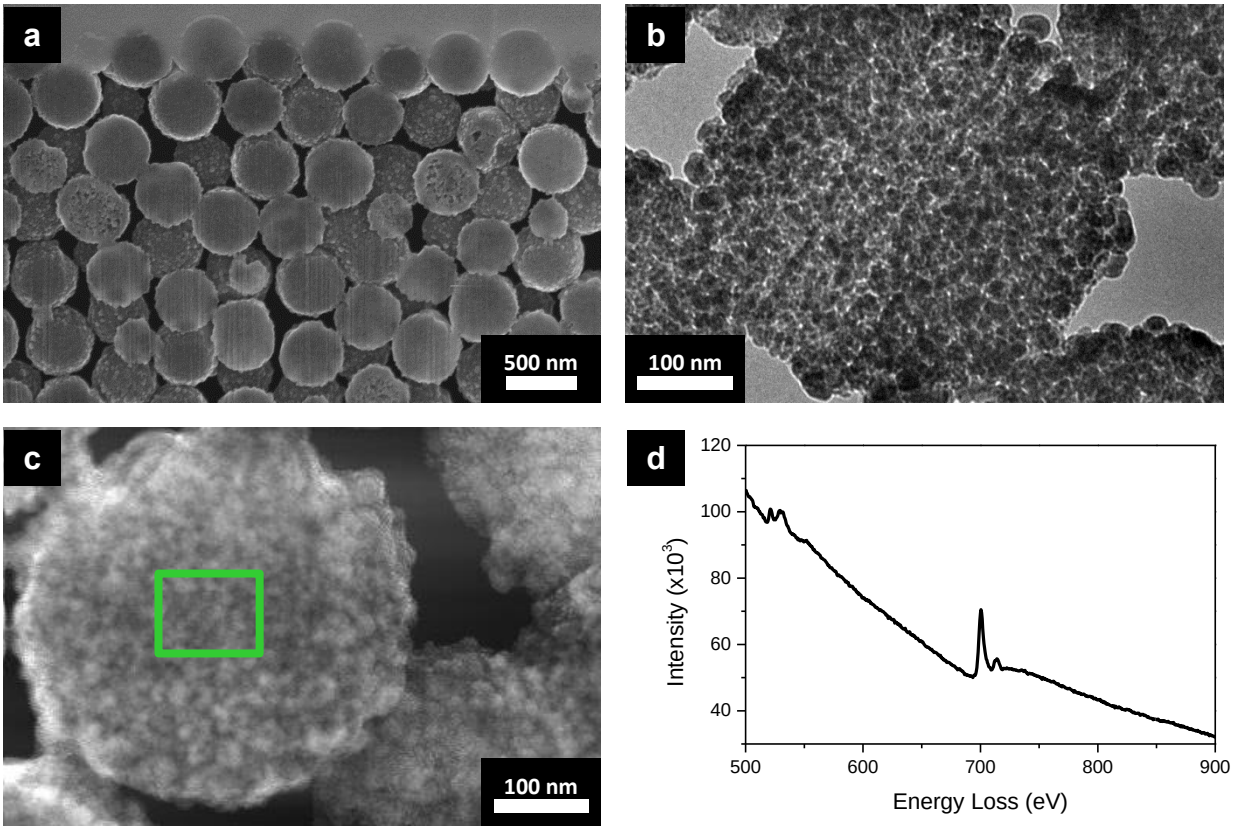

Figure 66. (a) SEM image of Monodispersed Starburst Carbon Spheres (MSCS) after Fe CVD deposition (incomplete infilling) and subsequent FIB liftout. (b) TEM and (c) STEM of the Fe-MSCS. (d) EELS spectrum taken from the inset in (c); the O and Fe peaks can be seen at ~520 and ~700 eV, respectively.

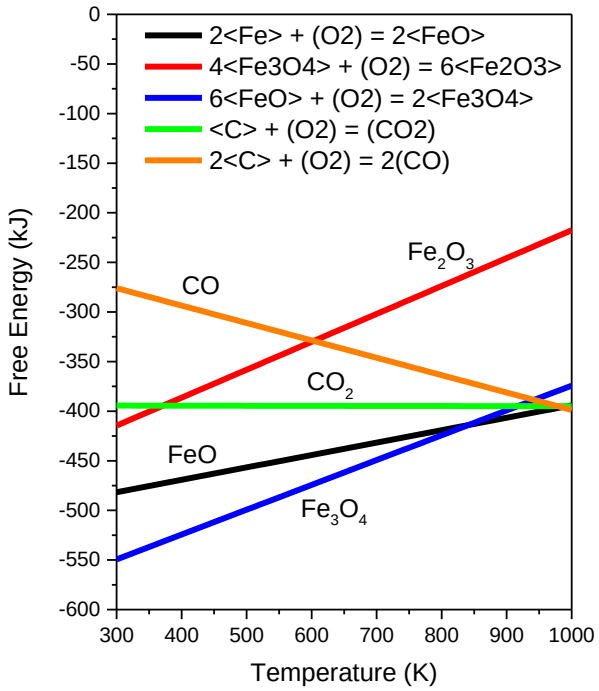

Figure 67. Ellingham diagram showing possible reactions of Fe and C during oxidation. Fe_3O_4 is favored at low temperatures and low oxygen partial pressure.

A main advantage of using MSCS for Fe CVD template is the possible lithium-ion battery anode fabrication by converting the Fe to Fe_3O_4. Fe_3O_4 has attracted considerable attention for anodes due to its relatively high capacity (~1000 mAh g^{-1}), high abundance, and low-cost [123, 125, 133, 134]. In these, Fe_3O_4 is prepared by the reduction of Fe ions from solution and attaching to a carbon support (graphene or carbon foam). By using the MSCS colloidal crystal template, the deposited Fe can be directly converted to Fe_3O_4. This will allow better control over the conformality and amount deposited. Additionally, the MSCS template should provide a conductive pathway and, assuming the Fe deposited is well below the pinch-off point, allow for the volume expansion of the Fe_3O_4 during cycling. To convert the Fe-MSCS to Fe_3O_4-MSCS, a

partial oxidation is needed, while maintaining the MSCS scaffold, i.e., little to no carbon oxidation. **Figure 67** shows the calculated Ellingham diagram of the possible C and Fe oxidation reactions [146]. At temperatures below 843 K (570 °C), Fe_3O_4 is thermodynamically favored. An initial attempt at converting the Fe to Fe_3O_4 was made by oxidizing the sample in air at 400 °C for 3 hr. This resulted in a reddish sample, indicating conversion to Fe_2O_3 instead of Fe_3O_4. While Fe_3O_4 is energetically favored, an excess of oxygen will drive the reaction to Fe_2O_3, with XRD confirmation in **Figure 68**. Additionally, when Fe_2O_3 is formed, the thermodynamic energy landscape dictates that the carbon template should be oxidized and removed; a FIB cut (**Figure 69**) confirms this. By reducing the time and/or temperature for oxidation, conversion to Fe_3O_4 should be possible.

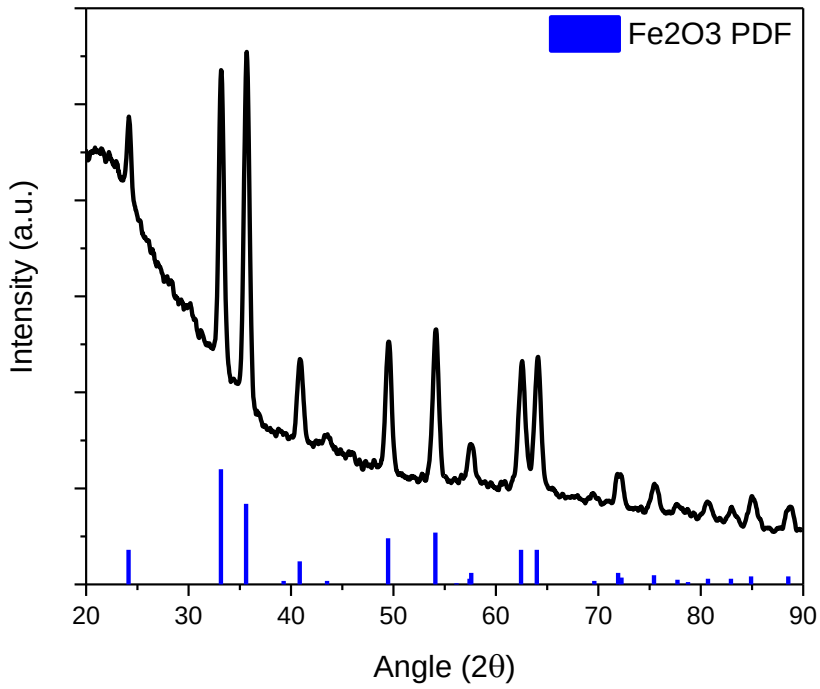

Figure 68. XRD of oxidized iron at 400°C for 3 hours. The sharp peaks line up perfectly with the Fe_2O_3 PDF file (PDF#00-033-0664).

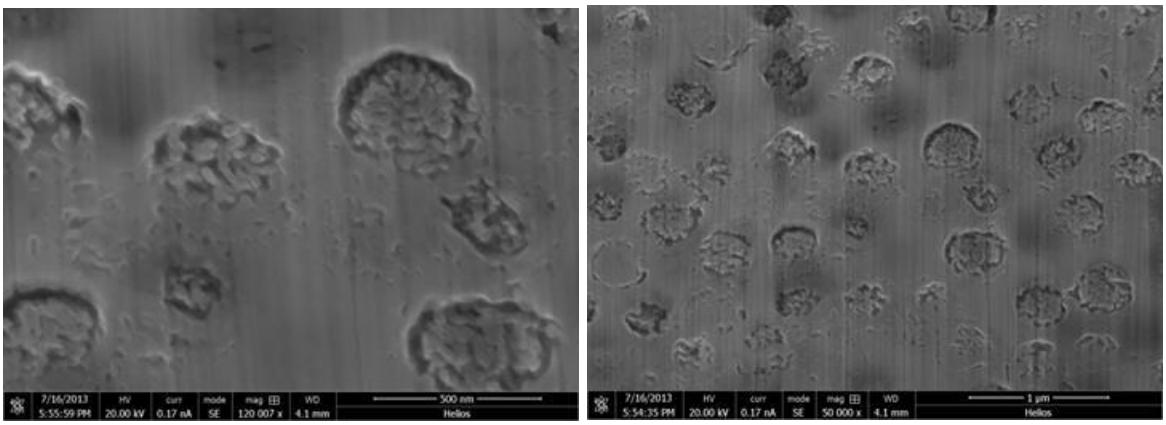

Figure 69. FIB cut on the MSCS template, coated via Fe CVD, and oxidized at 400 °C in air for 3 hr.

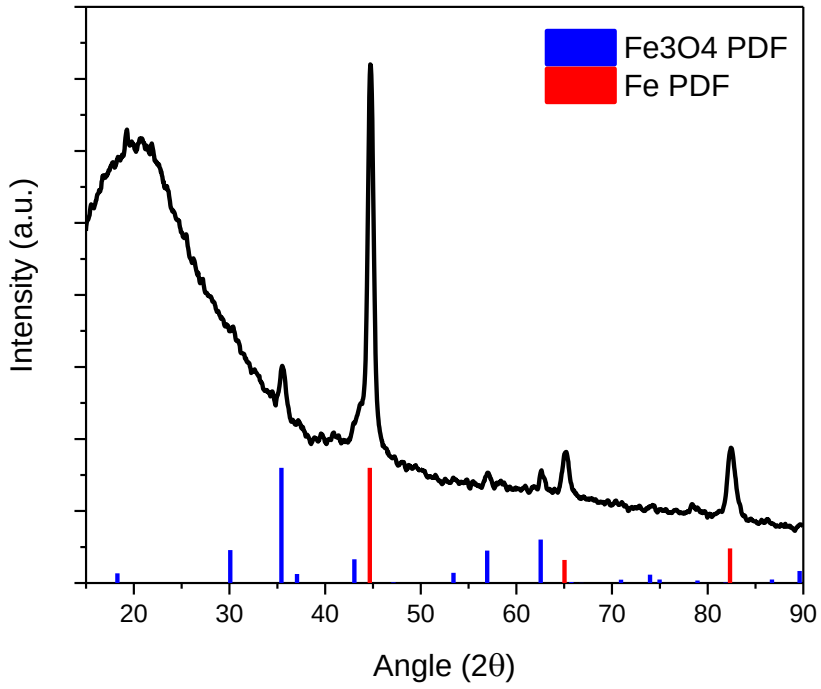

Figure 70. XRD of oxidized Fe-C under 7.4 E-6 mbar vacuum. The Fe partially oxidized to Fe_3O_4; PDF files are Fe PDF#00-006-0696 and Fe_3O_4 PDF#04-005-4319.

To reduce the oxygen content and obtain Fe_3O_4, a Fe-C colloidal crystal sample was placed in a reactor vessel under vacuum (7.4 E-6 mbar), sealed, and placed in a furnace for 4 hours at 400°C (1 hour ramp). There should be a small amount of oxygen in the reactor vessel, allowing the iron to convert to magnetite and preserve the carbon colloids, as well as preventing full oxidation to Fe_2O_3. XRD analysis (**Figure 70**) shows the iron was partially oxidized with some Fe_3O_4 peaks; however, the majority remained in the zero-valence iron. Experimentally, it was determined that heating at 400 °C under a partial pressure of 10 mbar fully oxidized the Fe to Fe_3O_4 while maintaining the MSCS scaffold. **Figure 71** shows the XRD plot of the Fe_3O_4-MSCS on a tungsten substrate. The peaks are indexed to both tungsten and Fe_3O_4 with no residual Fe peaks or fully oxidized Fe_2O_3 peaks. The crystallite size of the Fe_3O_4 was calculated to be 18.4 nm. While this is larger than the pore size, it is similar to the previous results where the crystallites

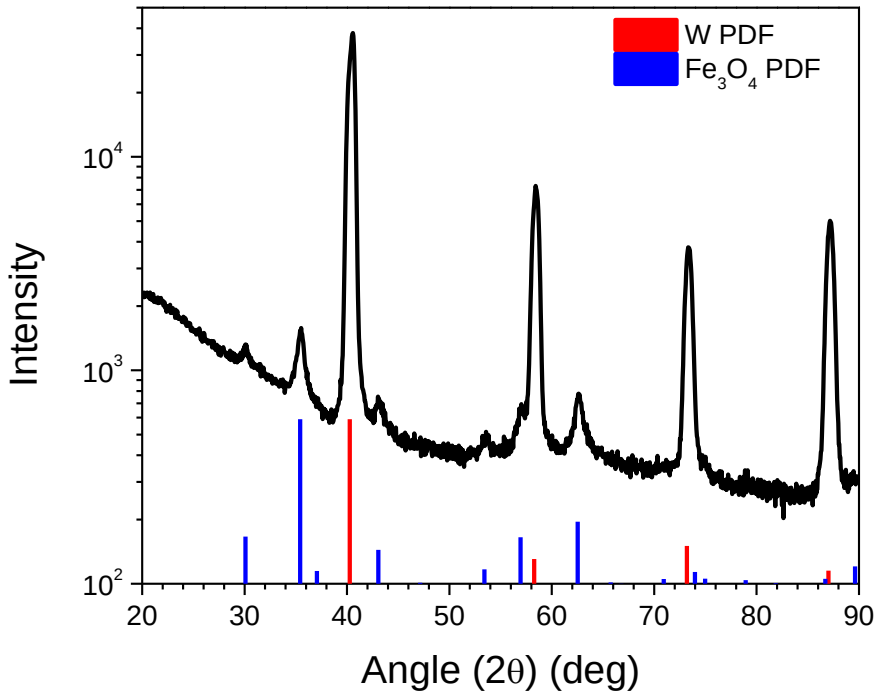

Figure 71. XRD plot showing complete conversion from Fe to Fe_3O_4. Crystallite size is 18.4 nm.

are aligned in the pores [1]. This same oxidation condition was then conducted to the sample in Figure 66 and similarly investigated, shown in **Figure 72**. The SEM, TEM, and STEM images (Figure 72(a-c)) show no degradation due to the oxidation. Figure 72(d) and (e) are the reconstructed images from the inset of Figure 72(c); Figure 72(d) is the reconstruction of only the oxygen EELS signal with Figure 72(e) from only the iron EELS signal. These show the oxidation and Fe infiltration is complete through the entire MSCS colloids.

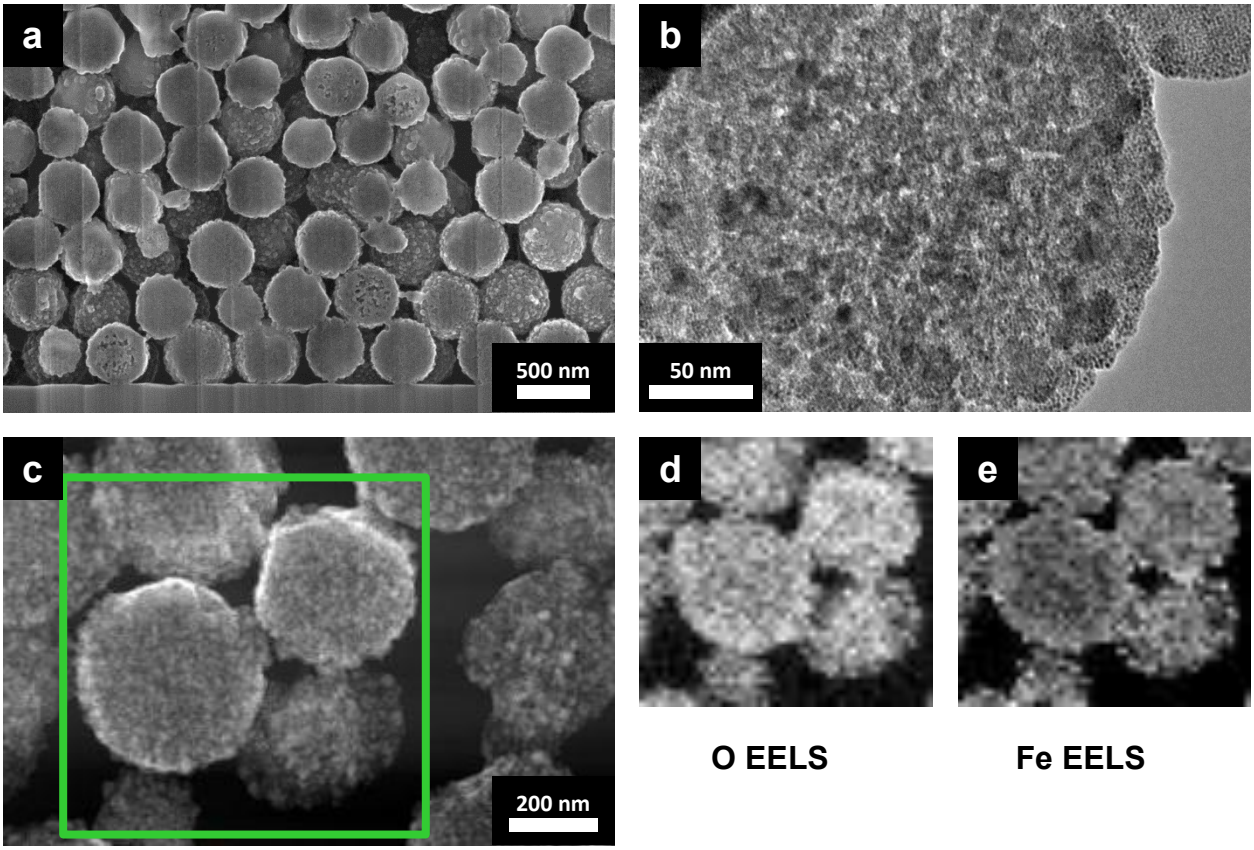

Figure 72. (a) SEM image of Fe-MSCS after partial oxidation of the Fe to Fe_3O_4. (b) TEM and (c) STEM of the Fe_3O_4-MSCS from (a). EELS reconstructed imaging using the (d) O signal and the (e) Fe signal from the inset of (c).

The Fe_3O_4-MSCS anode system utilizes the same electrode design and its advantages as the Si-MSCS anode with intriguing results. **Figure 73** shows the rate performance of an underfilled Fe_3O_4-MSCS, i.e., the Fe_3O_4 is confined in the mesopores (mass ration of Fe_3O_4 to C is 4:1). Similar to the Si-MSCS system, the initial 10 cycles at 0.15 C rate results in a sharp capacity fade, with the coulombic efficiency under 95%. The coulombic efficiency, however, continues to improve during cycling, aside from the one-cycle drop when C rates were changed. After 40 cycles, the coulombic efficiency improved to over 99%, quite significant in conversion reaction electrodes. Correspondingly, the capacity stabilizes after the initial drop with only mild loss during cycling at 0.5 and 1.2 C rates. After the initial 10 cycles, the rate was increased to 0.5 C for cycles 11-20 and further increased to 1.2 C for cycles 21-30. With higher cycling rates, more power can be delivered if the capacity does not drop significantly. At a rate of 1.2 C, the Fe_3O_4-MSCS anode still provides a capacity of 600 mA hr g^{-1}, 80% of the capacity at 0.5 C in cycles 11-20 (750 mA hr g^{-1}). By dropping the rate back to 0.5 C, the capacity improved to 700 mA hr g^{-1}, signifying little or no permanent damage was done to the anode through faster cycling. During fast charging, the rapid expansion conformational change of the active materials typically leads to aggregation and loss of electrical contact. Through the electrode design where the Fe_3O_4 active material is confined in MSCS mesopores, this loss of electrical contact is severely limited. Only through migration out of the mesopores could active material be lost and result in capacity fade.

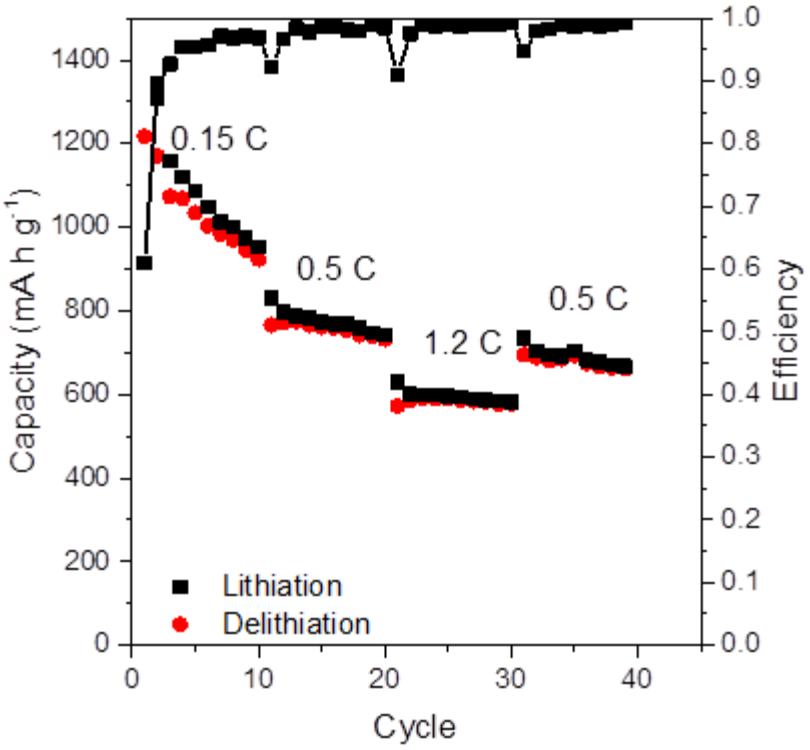

Figure 73. Cycle performance of Fe_3O_4-MSCS anode vs. Li.

With the high coulombic efficiency, the charge hysteresis was investigated. In this study, Fe_3O_4-MSCS anodes were fabricated with varying initial deposition amounts of Fe; providing insight are the two extremes, namely an underfilled anode similar to the anode cycled in Figure 73 and an overfilled Fe (and subsequent Fe_3O_4) anode, creating a shell on the MSCS. The charge hysteresis was determined by taking the differential charge with respect to voltage ($dQ\ dV^{-1}$) and analyzing the peaks. These were taken at the second charge/discharge cycle with a cycling rate of 0.2 C and 5 C. These $dQ\ dV^{-1}$ plots are shown in **Figure 74**, with the underfilled anode in Figure 74(a & c) and overfilled in Figure 74(b & d). The peak near 1.0 V (1.0 V for the underfilled anode and 0.95 V for the overfilled) is the major contributor of the derived capacity and is

generated by the reduction reaction $Li_xFe_3O_4 + (8-x) = 3Fe + 4Li_2O$ [147]. Due to the nanoparticle size, the structural transformation of Fe_3O_4 to a Li-Fe-O complex ($Li_xFe_3O_4$) can easily occur. Indeed, due to the mesopores confinement, there is little likelihood of large Fe particle formation that could suppress this transformation; this complex is responsible for the broad shoulder-peak from 1.0 to 1.6 V [147]. For the 0.2 C cycling test, the hysteresis was taken as the difference between the reduction peak and the lower voltage of the two oxidation peaks (1.6 V for the underfilled and 1.7 V for the overfilled anode), which corresponds to the oxidation of Fe^0 to Fe^{2+} [148]. In the case of the underfilled Fe_3O_4-MSCS anode, the hysteresis is quite low at 0.60 V while the overfilled hysteresis is increased to 0.75 V. The confinement of the Fe_3O_4 active material in the mesopores imposes the nanoparticle size and reduces, perhaps eliminates, particle aggregation, and provides an intimate current collector. For cycling at 5 C, the two oxidation peaks merge, with both the underfilled and overfilled samples having similar hysteresis: 1.1 V and 1.05 V, respectively.

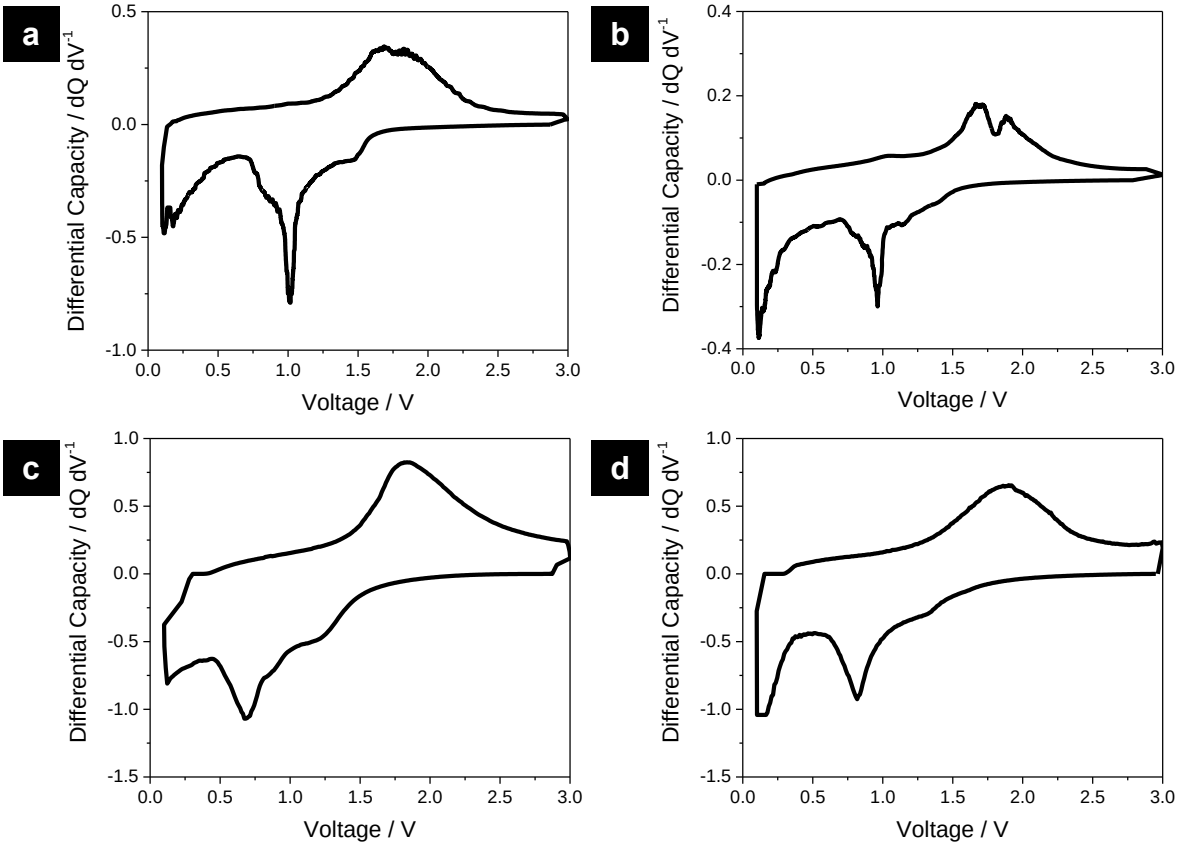

Figure 74. Differential capacity (dQ dV^{-1}) plots of the Fe_3O_4-MSCS anode cycled at (a & c) 0.2 C and (c & d) 5 C: (a & c) low-filled Fe_3O_4 with a hysteresis of 0.60 V at 0.2 C and 1.1 V at 5 C; (b & d) overfilled Fe_3O_4 with a hysteresis of 0.75 V at 0.2 C and 1.05 V at 5 C.

6.4 Magnetic Investigation of Iron CVD

An interesting experiment with the Fe-MSCS composites presented itself when a collaborator indicated a new vibrating sample magnetometer (VSM) was available for testing. As such, a MSCS colloidal crystal was fabricated (480 nm diameter, 1.79 nm pore diameter) and Fe CVD was performed, fabricating a sample similar to Figure 60. The Fe infiltrated the mesopores and also completely filled the interstitials between the colloids. Preliminary magnetic measurements on the Fe-MSCS colloidal crystal composite show a coercivity of 68 Oe at 300 K (**Figure 75**);

this is similar to 7 nm particles [149], even though a nanostructured, 3-dimensional inverse colloidal crystal was used. Room-temperature (300 K) superparamagnetism has been observed in 5 nm iron particles embedded in alumina matrix [149], particles consisting of 5 nm or less core Fe surrounded by a shell of iron oxides [150], and larger 20-40 nm Fe_3O_4 particles-on-graphene composites [124]. The current hypothesis is the Fe inside the pores behaves superparamagnetic, due to the small diameter (pore size of 1.87 nm), while the outer shell of Fe is large enough to support ferromagnetic behavior. This could be tested by varying the deposition thickness of the Fe layer through different static CVD times. XRD was taken on a Fe-coated carbon colloidal crystal grown on glass and was confirmed to have the Fe crystalline structure, with the crystallite size determined to be 11.4 nm

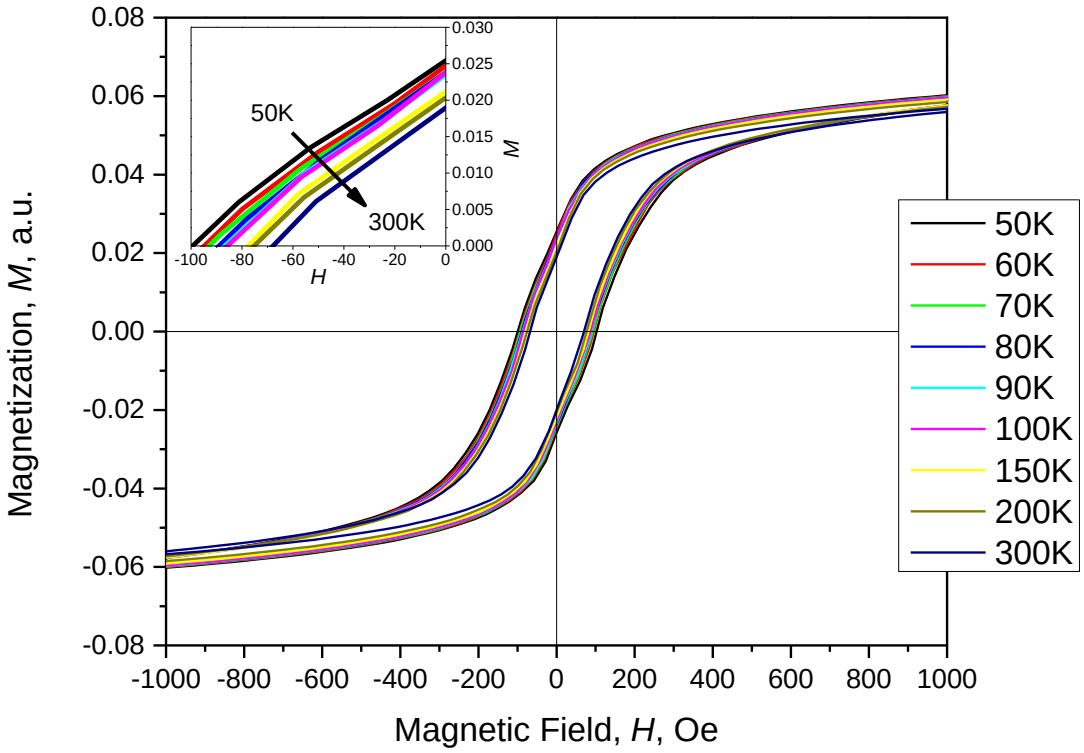

Figure 75. Magnetic measurements on Fe-MSCS as a function of temperature. Inset shows the upper-left quadrant.

6.5 Conclusions

In conclusion, anode systems that take advantage of a unique scaffold structure, namely the mesoporous MSCS, were developed. These carbon scaffolds provide a conductive network where the active materials, Si and Fe_3O_4, are confined in mesopores with short electron diffusion lengths, due to the pore diameter of 4.29 nm, allowing facile electron extraction. Additionally, by confining the active material in the pores, any pulverization or migration is suppressed and loss of capacity through material loss (electrical isolation) is minimized. The Si-MSCS anode showed stability through 85 cycles with the addition of VC to the electrolyte for SEI stabilization.

Confining the Fe_3O_4 active material into the mesopores resulted in high coulombic efficiency, and most intriguingly, a decrease in the charge hysteresis to 0.60 V at a cycling rate of 0.2 C. This decrease is attributed to the unique electrode design (i.e., confinement in the mesopores); increasing the Fe_3O_4 active material content overfills the mesopores and results in an increase in the hysteresis. Additionally, preliminary magnetic measurements on the Fe-MSCS composite show unique performance, a combination of superparamagnetic and ferromagnetic behavior.

6.6 Experimental Procedures

Formation of Carbon Template: Monodisperse starburst carbon spheres (MSCS) were synthesized [77] and oxidized [1] as previously reported. Tungsten substrates were sonicated for 1 hr in concentrated ethanolic KOH, rinsed, dried, and placed in a solution of known concentration (typically 0.75 wt%) of well-dispersed MSCS in ethanol at 40 °C overnight.

Material Deposition: Iron pentacarbonyl ($Fe(CO)_5$ from Sigma) was used as the iron source during Fe static CVD. Using standard air-free techniques, ~5 mL of $Fe(CO)_5$ was placed in a flask purged with nitrogen. MSCS-coated substrates were heated to 150 °C for 2 hr under a vacuum of 10^{-5} mbar. After cooling and sealing the vacuum line, the precursor valve was opened for equilibrated $Fe(CO)_5$ vapors to enter the sample chamber, typically less than 2 minutes. The reactor was sealed and placed into a furnace at 150 °C (1 °C/min ramp) for 1 hr (underfilled) or 5 hr (overfilled). Si CVD was conducted by decreasing the Si_2H_6 precursor amount from previous reports [1]. To oxidize the Fe to Fe_3O_4, a Fe-coated sample was heated under 10 mbar partial pressure to 400 °C for 3 hr (16 °C/min ramp). Oxidizing in air converted the Fe to Fe_2O_3 while completely oxidizing (i.e., removing) the carbon template.

Coin Cell Fabrication and Testing: Li-ion half cells were fabricated in the standard coin cell configuration using Celgard spacer, Novolyte electrolyte (1.0 M $LiPF_6$ in EC/DEC/DMC (1:1:1 by vol.)), and Li metal as the counter electrode. Electrolyte modification was conducted by the addition of vinylene carbonate (VC) to the Novolyte, resulting in ~5wt% VC. The half cells were cycled at room temperature under constant current at varying rates. The Si-MSCS anode was cycled between 0.1 and 2.0 V while the Fe_3O_4-MSCS anode was cycled between 0.1 and 3.0 V.

CHAPTER 7

CONCLUSIONS

Colloidal crystals, and specifically, mesoporous silica and carbon colloids, were used in templating a variety of materials and a number of applications investigated. The first investigation (Chapter 2) used nonporous silica colloids less than 300 nm in diameter to fabricate a colloidal crystal for Brillouin Light Scattering (BLS) experiments. By varying the experimental conditions, colloidal crystals, with the small diameter silica, could be successfully fabricated on quartz and silicon substrates, which has previously been a challenge. Over-deposition in the silicon chemical vapor deposition (CVD) process was eliminated by modifying the precursor concentration while still filling the interstitial voids. Through careful processing, the silica template was removed via hydrofluoric acid (HF) etching after a brief reactive ion etch (RIE) to open the top silicon shell; the silicon inverse opal maintained excellent optical properties after the etching. However, the BLS spectra showed unusual behavior in that the Stokes and anti-Stokes were not symmetrical, with no clear explanation. The dispersion relationship between the phonon frequencies and wave vectors did not show any phononic band structure, which may be due to the unusual spectra obtained.

Mesoporous silica, with a mesopore diameter of approximately 2.3 nm, was used as templates for platinum and silicon deposition (Chapter 3). A colloidal crystal of the mesoporous silica (622 nm diameter) was fabricated, and platinum was deposited via atomic layer deposition (ALD). After HF etching of the silica, a mesoporous platinum shell was revealed due to the incomplete infilling during the ALD process. Silicon was deposited via CVD, again modifying the reaction condition to infiltrate the mesopores with thermal conductivity measurements taken on the

silicon-silica composite. The results show that a polycrystalline silicon film, deposited via CVD, has a thermal conductivity of 38 W $m^{-1}K^{-1}$, while the effective thermal conductivity of the silicon-silica composite was an order of magnitude less, between 2.2 and 2.4 W $m^{-1}K^{-1}$. Simple modeling, using a parallel thermal conductivity model, attempted to extract the material thermal conductivity of the silicon; however, more detailed investigations are needed for accurate results.

Tailoring the surface charge of mesoporous starburst carbon spheres (MSCS) through a partial oxidation allowed the first high-quality carbon colloidal crystals to be fabricated (Chapter 4). Templating a variety of materials, i.e., hafnia, alumina, and silicon, on these high-surface area colloidal crystals resulted in deep penetration of the mesopores, creating unique, high-surface area, nanostructured inverse opals. Importantly, the MSCS removal process is completely orthogonal to the deposited material removal, preserving the fine-scale mesostructure of the MSCS in the templated materials. Because MSCS removal is orthogonal to the etching of many materials, MSCS provide a general approach for templating materials that currently cannot be templated by conventional colloidal crystals.

For improvement in dye-sensitized solar cells (DSSC), further templating of the MSCS colloidal crystal was done with titania (Chapter 5). By depositing a few nanometers of titania on the conductive substrate, high-quality MSCS colloidal crystals were fabricated, followed by a titania ALD to infiltrate the mesopores. The MSCS template was removed orthogonally: a simple oxidation process after the crystallization of the titania into the anatase crystal phase. After assembling the nanostructured titania into a DSSC, the photovoltaic characteristics indicated low absorption of the incident photons, with low dye loading in the titania nanostructure revealed to

be the cause. Attempts to increase the dye adsorption by opening the top colloid surface through RIE or by depositing only a very thin coating of titania were unsuccessful. As such, MSCS colloidal crystals are not suitable as a template for DSSC applications.

Anode systems that take advantage of the MSCS unique scaffold structure were developed for lithium batteries (Chapter 6). Silicon and Fe_3O_4 active materials are confined in the mesopores, and the MSCS template provides a porous, conductive network allowing both electrolyte diffusion and electron extraction. Confinement of the active materials suppresses any pulverization or migration and also minimizes capacity loss through electrical isolation of active materials. Through the addition of vinylene carbonate to the electrolyte, the silicon-MSCS anode was cycled 85 times, indicating that the solid-electrolyte interface was stabilized. Through the active material confinement, high coulombic efficiency was achieved in the Fe_3O_4-MSCS anode, with a decrease in the charge hysteresis, from 0.90 V in conventional systems to 0.60 V in the confined Fe_3O_4-MSCS anode. This decrease is attributed to the unique electrode design; increasing the Fe_3O_4 active material content overfills the mesopores and results in an increase in the hysteresis. Preliminary magnetic measurements on the Fe-MSCS composite show unique performance, a combination of superparamagnetic and ferromagnetic behavior.

These results demonstrate the unique structures that can be fabricated through the use of colloidal crystals and mesoporous templates. Fundamental studies of the phononic band structure and thermal conductivity were investigated. Carbon colloids, for the first time, self-assembled into a high-quality colloidal crystal, changing the templating paradigm due to the orthogonal removal of the carbon. Additionally, the mesoporous structure allowed for applications that

previously were inaccessible, specifically the DSSC and lithium battery anodes. While the mesoporous DSSC structure was ultimately inferior, the mesoporous carbon colloidal crystal provided an excellent scaffold for the lithium battery anodes, with some exceptional properties directly enabled by the mesoporous colloids.

REFERENCES

1. Goodman, M.D., et al., *Enabling New Classes of Templated Materials through Mesoporous Carbon Colloidal Crystals.* Advanced Optical Materials, 2013. **1**(4): p. 300-304.
2. Norris, D.J., et al., *Opaline photonic crystals: How does self-assembly work?* Advanced Materials, 2004. **16**(16): p. 1393-1399.
3. Jiang, P., et al., *Single-crystal colloidal multilayers of controlled thickness.* Chemistry of Materials, 1999. **11**(8): p. 2132-2140.
4. Dimitrov, A.S. and K. Nagayama, *Continuous convective assembling of fine particles into two-dimensional arrays on solid surfaces.* Langmuir, 1996. **12**(5): p. 1303-1311.
5. Xu, X.L. and S.A. Asher, *Synthesis and utilization of monodisperse hollow polymeric particles in photonic crystals.* Journal of the American Chemical Society, 2004. **126**(25): p. 7940-7945.
6. Park, S.H. and Y.N. Xia, *Assembly of mesoscale particles over large areas and its application in fabricating tunable optical filters.* Langmuir, 1999. **15**(1): p. 266-273.
7. Joannopoulos, J.D., et al., *Photonic Crystals: Molding the Flow of Light (Second Edition)*2008: Princeton University Press. 304.
8. Marlow, F., et al., *Opals: status and prospects.* Angewandte Chemie International Edition, 2009. **48**(34): p. 6212-33.
9. Yablonovitch, E., *PHOTONIC BAND-GAP STRUCTURES.* Journal of the Optical Society of America B-Optical Physics, 1993. **10**(2): p. 283-295.
10. Yablonovitch, E., T.J. Gmitter, and K.M. Leung, *PHOTONIC BAND-STRUCTURE - THE FACE-CENTERED-CUBIC CASE EMPLOYING NONSPHERICAL ATOMS.* Physical Review Letters, 1991. **67**(17): p. 2295-2298.
11. Yablonovitch, E., *INHIBITED SPONTANEOUS EMISSION IN SOLID-STATE PHYSICS AND ELECTRONICS.* Physical Review Letters, 1987. **58**(20): p. 2059-2062.
12. Gennady, S. and A.U. Yaroslav, *Electric and magnetic properties of sub-wavelength plasmonic crystals.* Journal of Optics A: Pure and Applied Optics, 2005. **7**(2): p. S23.
13. Zeghbroeck, B.V., *Principles of Semiconductor Devices*, 2011.
14. Schroden, R.C., et al., *Optical properties of inverse opal photonic crystals.* Chemistry of Materials, 2002. **14**(8): p. 3305-3315.
15. Busch, K. and S. John, *Photonic band gap formation in certain self-organizing systems.* Physical Review E, 1998. **58**(3): p. 3896-3908.
16. Vos, W.L., et al., *Strong effects of photonic band structures on the diffraction of colloidal crystals.* Physical Review B, 1996. **53**(24): p. 16231-16235.
17. Rinne, S.A., F. Garcia-Santamaria, and P.V. Braun, *Embedded cavities and waveguides in three-dimensional silicon photonic crystals.* Nature Photonics, 2008. **2**(1): p. 52-56.
18. Huang, Z., et al., *Design and Fabrication of Carbon Quantum Dots/TiO2 Photonic Crystal Complex with Enhanced Photocatalytic Activity.* Journal of Nanoscience and Nanotechnology, 2014. **14**(6): p. 4156-4163.
19. Quan, L.N., et al., *Soft-template-carbonization route to highly textured mesoporous carbon-TiO2 inverse opals for efficient photocatalytic and photoelectrochemical applications.* Physical Chemistry Chemical Physics, 2014. **16**(19): p. 9023-9030.

20. Xia, L., et al., *Zinc oxide inverse opal electrodes modified by glucose oxidase for electrochemical and photoelectrochemical biosensor.* Biosensors & bioelectronics, 2014. **59**: p. 350-7.
21. Lee, Y.J. and P.V. Braun, *Tunable inverse opal hydrogel pH sensors.* Advanced Materials, 2003. **15**(7-8): p. 563-566.
22. Zakhidov, A.A., et al., *Carbon structures with three-dimensional periodicity at optical wavelengths.* Science, 1998. **282**(5390): p. 897-901.
23. Holtz, J.H. and S.A. Asher, *Polymerized colloidal crystal hydrogel films as intelligent chemical sensing materials.* Nature, 1997. **389**(6653): p. 829-832.
24. Lee, K. and S.A. Asher, *Photonic crystal chemical sensors: pH and ionic strength.* Journal of the American Chemical Society, 2000. **122**(39): p. 9534-9537.
25. Velev, O.D. and E.W. Kaler, *In situ assembly of colloidal particles into miniaturized biosensors.* Langmuir, 1999. **15**(11): p. 3693-3698.
26. Eckert, A.W., *The World of Opals*1997, New York: Wiley.
27. Finlayson, C.E., et al., *3D bulk ordering in macroscopic solid opaline films by edge-induced rotational shearing.* Advanced Materials, 2011. **23**(13): p. 1540-4.
28. Yamada, H., et al., *Colloidal-Crystal Laser Using Monodispersed Mesoporous Silica Spheres.* Advanced Materials, 2009. **21**(41): p. 4134-+.
29. Aguirre, C.I., E. Reguera, and A. Stein, *Tunable Colors in Opals and Inverse Opal Photonic Crystals (vol 20, pg 2565, 2010).* Advanced Functional Materials, 2011. **21**(2): p. 210-210.
30. Kim, S.-H., et al., *Self-assembled colloidal structures for photonics.* Npg Asia Materials, 2011. **3**(1): p. 25-33.
31. Stöber, W., A. Fink, and E. Bohn, *Controlled growth of monodisperse silica spheres in the micron size range.* Journal of Colloid and Interface Science, 1968. **26**(1): p. 62-69.
32. Reese, C.E., et al., *Synthesis of highly charged, monodisperse polystyrene colloidal particles for the fabrication of photonic crystals.* Journal of Colloid and Interface Science, 2000. **232**(1): p. 76-80.
33. Ocier, C. and P.V. Braun, *Facile Growth of Micron-sized Silica Colloids into a Well Ordered Colloidal Crystal.* unpublished, 2014.
34. Deegan, R.D., et al., *Capillary flow as the cause of ring stains from dried liquid drops.* Nature, 1997. **389**(6653): p. 827-829.
35. Xu, J., J. Xia, and Z. Lin, *Evaporation-induced self-assembly of nanoparticles from a sphere-on-flat geometry.* Angewandte Chemie-International Edition, 2007. **46**(11): p. 1860-1863.
36. Fischer, B.J., *Particle Convection in an Evaporating Colloidal Droplet.* Langmuir, 2002. **18**(1): p. 60-67.
37. Jiang, P. and M.J. McFarland, *Large-scale fabrication of wafer-size colloidal crystals, macroporous polymers and nanocomposites by spin-coating.* Journal of the American Chemical Society, 2004. **126**(42): p. 13778-13786.
38. Ferrand, P., et al., *Micromoulding of three-dimensional photonic crystals on silicon substrates.* Nanotechnology, 2003. **14**(2): p. 323-326.
39. Ye, J., et al., *Integration of self-assembled three-dimensional photonic crystals onto structured silicon wafers.* Langmuir, 2006. **22**(17): p. 7378-7383.

40. Wong, S., V. Kitaev, and G.A. Ozin, *Colloidal crystal films: Advances in universality and perfection.* Journal of the American Chemical Society, 2003. **125**(50): p. 15589-15598.
41. Colodrero, S., et al., *Porous One-Dimensional Photonic Crystals Improve the Power-Conversion Efficiency of Dye-Sensitized Solar Cells.* Advanced Materials, 2009. **21**(7): p. 764-+.
42. Guldin, S., et al., *Dye-Sensitized Solar Cell Based on a Three-Dimensional Photonic Crystal.* Nano Letters, 2010. **10**(7): p. 2303-2309.
43. Halaoui, L.I., N.M. Abrams, and T.E. Mallouk, *Increasing the conversion efficiency of dye-sensitized TiO2 photoelectrochemical cells by coupling to photonic crystals.* Journal of Physical Chemistry B, 2005. **109**(13): p. 6334-6342.
44. Mihi, A. and H. Miguez, *Origin of light-harvesting enhancement in colloidal-photonic-crystal-based dye-sensitized solar cells.* Journal of Physical Chemistry B, 2005. **109**(33): p. 15968-15976.
45. Nishimura, S., et al., *Standing wave enhancement of red absorbance and photocurrent in dye-sensitized titanium dioxide photoelectrodes coupled to photonic crystals.* Journal of the American Chemical Society, 2003. **125**(20): p. 6306-6310.
46. Yang, S.-C., et al., *Hollow TiO2 hemispheres obtained by colloidal templating for application in dye-sensitized solar cells.* Advanced Materials, 2008. **20**(5): p. 1059-+.
47. Oregan, B. and M. Gratzel, *A Low-Cost, High-Efficiency Solar-Cell Based On Dye-Sensitized Colloidal TiO2 Films.* Nature, 1991. **353**(6346): p. 737-740.
48. Mihi, A., C. Zhang, and P.V. Braun, *Transfer of Preformed Three-Dimensional Photonic Crystals onto Dye-Sensitized Solar Cells.* Angewandte Chemie International Edition, 2011. **50**(25): p. 5712-5715.
49. Pursiainen, O.L.J., et al., *Compact strain-sensitive flexible photonic crystals for sensors.* Applied Physics Letters, 2005. **87**(10): p. -.
50. Nelson, E.C., et al., *Epitaxial growth of three-dimensionally architectured optoelectronic devices.* Nature Materials, 2011. **10**(9): p. 676-681.
51. Griffete, N., et al., *Inverse Opals of Molecularly Imprinted Hydrogels for the Detection of Bisphenol A and pH Sensing.* Langmuir, 2012. **28**(1): p. 1005-1012.
52. Pan, Z., et al., *Response of inverse-opal hydrogels to alcohols.* Journal of Materials Chemistry, 2012. **22**(5): p. 2018-2025.
53. Barry, R.A. and P. Wiltzius, *Humidity-sensing inverse opal hydrogels.* Langmuir, 2006. **22**(3): p. 1369-1374.
54. Wang, J., et al., *Multiresponsive inverse-opal hydrogels.* Advanced Materials, 2007. **19**(22): p. 3865-+.
55. Isshiki, Y., et al., *Electric Double-Layer Capacitance of Inverse Opal Carbon Prepared Through Carbonization of Poly(Furfuryl Alcohol) in Contact With Polymer Gel Electrolyte Containing Ionic Liquid.* Polymers for Advanced Technologies, 2011. **22**(8): p. 1254-1260.
56. Zhang, H., X. Yu, and P.V. Braun, *Three-dimensional bicontinuous ultrafast-charge and -discharge bulk battery electrodes.* Nature Nanotechnology, 2011. **6**(5): p. 277-281.
57. Mandlmeier, B., et al., *Formation of Interpenetrating Hierarchical Titania Structures by Confined Synthesis in Inverse Opal.* Journal of the American Chemical Society, 2011. **133**(43): p. 17274-17282.

58. Zhang, H. and P.V. Braun, *Three-Dimensional Metal Scaffold Supported Bicontinuous Silicon Battery Anodes.* Nano Letters, 2012. **12**(6): p. 2778-2783.
59. Zhang, M.-L., et al., *Inverse opal hydrogel sensor for the detection of pH and mercury ions.* Rsc Advances, 2014. **4**(39): p. 20567-20572.
60. Bai, Y., et al., *Enzyme-free glucose sensor based on a three-dimensional gold film electrode.* Sensors and Actuators B-Chemical, 2008. **134**(2): p. 471-476.
61. Scott, R.W.J., et al., *Tin dioxide opals and inverted opals: Near-ideal microstructures for gas sensors.* Advanced Materials, 2001. **13**(19): p. 1468-+.
62. Benak, K.R., et al., *Sulfonation of pyropolymeric fibers derived from phenol-formaldehyde resins.* Carbon, 2002. **40**(13): p. 2323-2332.
63. Zhang, J., et al., *Highly ordered macroporous carbon spheres and their catalytic application for methanol oxidation.* Journal of Colloid and Interface Science, 2011. **361**(2): p. 503-508.
64. Cheng, F., et al., *Template-directed materials for rechargeable lithium-ion batteries.* Chemistry of Materials, 2008. **20**(3): p. 667-681.
65. Xiao, J., et al., *Hierarchically porous graphene as a lithium-air battery electrode.* Nano Letters, 2011. **11**(11): p. 5071-8.
66. Liu, J., et al., *Extension of The Stober Method to the Preparation of Monodisperse Resorcinol-Formaldehyde Resin Polymer and Carbon Spheres.* Angewandte Chemie-International Edition, 2011. **50**(26): p. 5947-5951.
67. Sun, X.M. and Y.D. Li, *Colloidal carbon spheres and their core/shell structures with noble-metal nanoparticles.* Angewandte Chemie-International Edition, 2004. **43**(5): p. 597-601.
68. Yoon, S.B., et al., *Fabrication of carbon capsules with hollow macroporous core/mesoporous shell structures.* Advanced Materials, 2002. **14**(1): p. 19-21.
69. Zheng, M.B., et al., *Preparation of oxide hollow spheres by colloidal carbon spheres.* Materials Letters, 2006. **60**(24): p. 2991-2993.
70. Paraknowitsch, J.P., A. Thomas, and M. Antonietti, *Carbon Colloids Prepared by Hydrothermal Carbonization as Efficient Fuel for Indirect Carbon Fuel Cells.* Chemistry of Materials, 2009. **21**(7): p. 1170-+.
71. Chen, C.Y., et al., *A Two-Step Hydrothermal Synthesis Approach to Monodispersed Colloidal Carbon Spheres.* Nanoscale Research Letters, 2009. **4**(9): p. 971-976.
72. Lee, J., J. Kim, and T. Hyeon, *Recent progress in the synthesis of porous carbon materials.* Advanced Materials, 2006. **18**(16): p. 2073-2094.
73. Yamada, Y., et al., *Artificial black opal fabricated from nanoporous carbon spheres.* Langmuir, 2010. **26**(12): p. 10044-9.
74. Ferrari, A.C., et al., *Stress reduction and bond stability during thermal annealing of tetrahedral amorphous carbon.* Journal of Applied Physics, 1999. **85**(10): p. 7191-7197.
75. Yano, K. and Y. Fukushima, *Particle size control of mono-dispersed super-microporous silica spheres.* Journal of Materials Chemistry, 2003. **13**(10): p. 2577-2581.
76. Yano, K. and Y. Fukushima, *Synthesis of mono-dispersed mesoporous silica spheres with highly ordered hexagonal regularity using conventional alkyltrimethylammonium halide as a surfactant.* Journal of Materials Chemistry, 2004. **14**(10): p. 1579-1584.
77. Nakamura, T., Y. Yamada, and K. Yano, *Monodispersed nanoporous starburst carbon spheres and their three-dimensionally ordered arrays.* Microporous and Mesoporous Materials, 2009. **117**(1-2): p. 478-485.

78. Pan, H.H., *ACOUSTIC DYNAMICS OF NANOPARTICLES AND NANOSTRUCTURED PHONONIC CRYSTALS*, in *Physics*2013, National University of Singapore.
79. de Lima, M.M., R. Hey, and P.V. Santos, *Active photonic crystals based on surface acoustic waves.* Applied Physics Letters, 2003. **83**(15): p. 2997-2999.
80. Still, T., et al., *Colloidal systems: a promising material class for tailoring sound propagation at high frequencies.* Journal of Physics-Condensed Matter, 2008. **20**(40).
81. de Lima, M.M., et al., *Modulation of photonic crystals by surface acoustic waves.* Physica E-Low-Dimensional Systems & Nanostructures, 2004. **21**(2-4): p. 809-813.
82. Cheng, W., et al., *The spectrum of vibration modes in soft opals.* Journal of Chemical Physics, 2005. **123**(12).
83. Kuok, M.H., et al., *Brillouin Study of the Quantization of Acoustic Modes in Nanospheres.* Physical Review Letters, 2003. **90**(25): p. 255502.
84. Mihi, A., C.J. Zhang, and P.V. Braun, *Transfer of Preformed Three-Dimensional Photonic Crystals onto Dye-Sensitized Solar Cells.* Angewandte Chemie-International Edition, 2011. **50**(25): p. 5711-5714.
85. Jun, Y., et al., *Holographically Defined Nanoparticle Placement in 3D Colloidal Crystals.* Journal of the American Chemical Society, 2010. **132**(29): p. 9958-9959.
86. Yu, X.D., et al., *Template-Assisted Three-Dimensional Nanolithography via Geometrically Irreversible Processing.* Nano Letters, 2009. **9**(12): p. 4424-4427.
87. Zhu, G.H., et al., *Direct observation of the phonon dispersion of a three-dimensional solid/solid hypersonic colloidal crystal.* Physical Review B, 2013. **88**(14).
88. Yamauchi, Y., et al., *Electrochemical Synthesis of Mesoporous Pt-Au Binary Alloys with Tunable Compositions for Enhancement of Electrochemical Performance.* Journal of the American Chemical Society, 2012. **134**(11): p. 5100-5109.
89. Wang, H., et al., *Synthesis of Mesoporous Pt Films with Tunable Pore Sizes from Aqueous Surfactant Solutions.* Chemistry of Materials, 2012. **24**(9): p. 1591-1598.
90. Ma, J., et al., *Coherent Phonon-Grain Boundary Scattering in Silicon Inverse Opals.* Nano Letters, 2013. **13**(2): p. 618-624.
91. Losego, M.D., et al., *Ultralow Thermal Conductivity in Organoclay Nanolaminates Synthesized via Simple Self-Assembly.* Nano Letters, 2013. **13**(5): p. 2215-2219.
92. Uma, S., et al., *Temperature-dependent thermal conductivity of undoped polycrystalline silicon layers.* International Journal of Thermophysics, 2001. **22**(2): p. 605-616.
93. Hopkins, P.E. and L.M. Phinney, *Thermal Conductivity Measurements on Polycrystalline Silicon Microbridges Using the 3 omega Technique.* Journal of Heat Transfer-Transactions of the Asme, 2009. **131**(4): p. 043201-8
94. *Silicon (Si), sound velocities*, O. Madelung, U. Rössler, and M. Schulz, Editors. 2002.
95. Cahill, D.G., et al., *Nanoscale thermal transport.* Journal of Applied Physics, 2003. **93**(2): p. 793-818.
96. Lee, S.-M. and D.G. Cahill, *Heat transport in thin dielectric films.* Journal of Applied Physics, 1997. **81**(6): p. 2590-2595.
97. Fang, J., et al., *Temperature dependent thermal conductivity of pure silica MEL and MFI zeolite thin films.* Journal of Applied Physics, 2012. **111**(5): p. -.
98. Progelhof, R.C., J.L. Throne, and R.R. Ruetsch, *Methods for predicting the thermal conductivity of composite systems: A review.* Polymer Engineering & Science, 1976. **16**(9): p. 615-625.

99. Gesele, G., et al., *Temperature-dependent thermal conductivity of porous silicon.* Journal of Physics D-Applied Physics, 1997. **30**(21): p. 2911-2916.
100. Yang, H.T. and P. Jiang, *Scalable fabrication of superhydrophobic hierarchical colloidal arrays.* Journal of Colloid and Interface Science, 2010. **352**(2): p. 558-565.
101. Prevo, B.G. and O.D. Velev, *Controlled, rapid deposition of structured coatings from micro- and nanoparticle suspensions.* Langmuir, 2004. **20**(6): p. 2099-2107.
102. Mangun, C.L., et al., *Oxidation of activated carbon fibers: Effect on pore size, surface chemistry, and adsorption properties.* Chemistry of Materials, 1999. **11**(12): p. 3476-3483.
103. Koyanagi, M., T. Fukushima, and T. Tanaka, *High-Density Through Silicon Vias for 3-D LSIs.* Proceedings of the Ieee, 2009. **97**(1): p. 49-59.
104. Santos, P.S., H.S. Santos, and S.P. Toledo, *Standard transition aluminas. Electron microscopy studies.* Materials Research, 2000. **3**: p. 104-114.
105. von Freymann, G., et al., *Bottom-up assembly of photonic crystals.* Chemical Society Reviews, 2013. **42**: p. 2528-2554.
106. Wang, Q., et al., *Characteristics of high efficiency dye-sensitized solar cells.* Journal of Physical Chemistry B, 2006. **110**(50): p. 25210-25221.
107. Wang, Z.S., et al., *Significant influence of TiO2 photoelectrode morphology on the energy conversion efficiency of N719 dye-sensitized solar cell.* Coordination Chemistry Reviews, 2004. **248**(13-14): p. 1381-1389.
108. Mor, G.K., et al., *Use of highly-ordered TiO2 nanotube arrays in dye-sensitized solar cells.* Nano Letters, 2006. **6**(2): p. 215-218.
109. Park, N.G., J. van de Lagemaat, and A.J. Frank, *Comparison of Dye-Sensitized Rutile- and Anatase-Based TiO2 Solar Cells.* The Journal of Physical Chemistry B, 2000. **104**(38): p. 8989-8994.
110. Taberna, P.L., et al., *High rate capabilities Fe3O4-based Cu nano-architectured electrodes for lithium-ion battery applications.* Nature Materials, 2006. **5**(7): p. 567-73.
111. Tarascon, J.M. and M. Armand, *Issues and challenges facing rechargeable lithium batteries.* Nature, 2001. **414**(6861): p. 359-367.
112. Zhou, G., et al., *Graphene-Wrapped Fe3O4 Anode Material with Improved Reversible Capacity and Cyclic Stability for Lithium Ion Batteries.* Chemistry of Materials, 2010. **22**(18): p. 5306-5313.
113. Cui, L.F., et al., *Carbon-Silicon Core-Shell Nanowires as High Capacity Electrode for Lithium Ion Batteries.* Nano Letters, 2009. **9**(9): p. 3370-3374.
114. Chen, J. and K. Yano, *Highly Monodispersed Tin Oxide/Mesoporous Starbust Carbon Composite as High-Performance Li-Ion Battery Anode.* ACS Applied Materials & Interfaces, 2013. **5**(16): p. 7682-7687.
115. Kang, K.S., et al., *Electrodes with high power and high capacity for rechargeable lithium batteries.* Science, 2006. **311**(5763): p. 977-980.
116. Wang, H., et al., *Mn3O4-Graphene Hybrid as a High-Capacity Anode Material for Lithium Ion Batteries.* Journal of the American Chemical Society, 2010. **132**(40): p. 13978-13980.
117. Ding, N., et al., *Improvement of cyclability of Si as anode for Li-ion batteries.* Journal of Power Sources, 2009. **192**(2): p. 644-651.
118. Pikul, J.H., et al., *High-power lithium ion microbatteries from interdigitated three-dimensional bicontinuous nanoporous electrodes.* Nature Communications, 2013. **4**.

119. Winter, M., et al., *Insertion electrode materials for rechargeable lithium batteries.* Advanced Materials, 1998. **10**(10): p. 725-763.
120. Esmanski, A. and G.A. Ozin, *Silicon Inverse-Opal-Based Macroporous Materials as Negative Electrodes for Lithium Ion Batteries.* Advanced Functional Materials, 2009. **19**(12): p. 1999-2010.
121. Wu, H., et al., *Engineering Empty Space between Si Nanoparticles for Lithium-Ion Battery Anodes.* Nano Letters, 2012. **12**(2): p. 904-909.
122. Jiang, D., et al., *Electrodeposition and characterization of assembly of Sn on Cu nanorods for Li-ion microbattery application.* Journal of Solid State Electrochemistry, 2011. **15**(11-12): p. 2639-2644.
123. Kang, E., et al., *Fe3O4 Nanoparticles Confined in Mesocellular Carbon Foam for High Performance Anode Materials for Lithium-Ion Batteries.* Advanced Functional Materials, 2011. **21**(13): p. 2430-2438.
124. Li, B., et al., *Superparamagnetic Fe3O4 nanocrystals@graphene composites for energy storage devices.* Journal of Materials Chemistry, 2011. **21**(13): p. 5069-5075.
125. Zhou, G.M., et al., *Graphene-Wrapped Fe3O4 Anode Material with Improved Reversible Capacity and Cyclic Stability for Lithium Ion Batteries.* Chemistry of Materials, 2010. **22**(18): p. 5306-5313.
126. Dimov, N., S. Kugino, and M. Yoshio, *Carbon-coated silicon as anode material for lithium ion batteries: advantages and limitations.* Electrochimica Acta, 2003. **48**(11): p. 1579-1587.
127. Ng, S.-H., et al., *Highly reversible lithium storage in spheroidal carbon-coated silicon nanocomposites as anodes for lithium-ion batteries.* Angewandte Chemie-International Edition, 2006. **45**(41): p. 6896-6899.
128. Li, H., et al., *A high capacity nano-Si composite anode material for lithium rechargeable batteries.* Electrochemical and Solid State Letters, 1999. **2**(11): p. 547-549.
129. Wu, H., et al., *Stable cycling of double-walled silicon nanotube battery anodes through solid-electrolyte interphase control.* Nature Nanotechnology, 2012. **7**(5): p. 309-314.
130. Chen, L.B., et al., *Effect of vinylene carbonate (VC) as electrolyte additive on electrochemical performance of Si film anode for lithium ion batteries.* Journal of Power Sources, 2007. **174**(2): p. 538-543.
131. Li, M.Q., et al., *Effects of electrolytes on the electrochemical performance of Si/graphite/disordered carbon composite anode for lithium-ion batteries.* Electrochimica Acta, 2009. **54**(19): p. 4506-4513.
132. Wu, Y., et al., *Conformal Fe3O4 Sheath on Aligned Carbon Nanotube Scaffolds as High-Performance Anodes for Lithium Ion Batteries.* Nano Letters, 2013. **13**(2): p. 818-823.
133. Cui, Z.-M., et al., *High-Yield Gas-Liquid Interfacial Synthesis of Highly Dispersed Fe3O4 Nanocrystals and Their Application in Lithium-Ion Batteries.* Chemistry of Materials, 2009. **21**(6): p. 1162-1166.
134. Wang, J.-Z., et al., *Graphene-Encapsulated Fe3O4 Nanoparticles with 3D Laminated Structure as Superior Anode in Lithium Ion Batteries.* Chemistry-a European Journal, 2011. **17**(2): p. 661-667.
135. Wang, T.Q., et al., *Self-assembly of hierarchical Fe3O4 microsphere/graphene nanosheet composite: towards a promising high-performance anode for Li-ion batteries.* Rsc Advances, 2014. **4**(1): p. 322-330.

136. Kulova, T.L., et al., *A study of lithium insertion into electrodes with thin gold films.* Russian Journal of Electrochemistry, 2010. **46**(8): p. 877-881.
137. Chockla, A.M., et al., *Influences of Gold, Binder and Electrolyte on Silicon Nanowire Performance in Li-Ion Batteries.* Journal of Physical Chemistry C, 2012. **116**(34): p. 18079-18086.
138. Knoops, H.C.M., et al., *Atomic layer deposition for nanostructured Li-ion batteries.* Journal of Vacuum Science & Technology A: Vacuum, Surfaces, and Films, 2012. **30**(1): p. 010801-10.
139. Gratson, G.M., et al., *Direct-write assembly of three-dimensional photonic crystals: Conversion of polymer scaffolds to silicon hollow-woodpile structures.* Advanced Materials, 2006. **18**(4): p. 461-+.
140. Bain, M.F., et al., *Investigation into the selectivity of CVD iron from Fe(CO)(5) precursor on various metal and dielectric patterned substrates.* Surface & Coatings Technology, 2007. **201**(22-23): p. 8998-9002.
141. Low, Y.H., et al., *Selective deposition of CVD iron on silicon dioxide and tungsten.* Microelectronic Engineering, 2006. **83**(11-12): p. 2229-2233.
142. Cireasa, R., et al., *An experimental study on iron thin films obtained by laser pyrolysis of iron pentacarbonyl vapour.* Surface and Coatings Technology, 1996. **80**(1–2): p. 229-232.
143. Cloud, A.N., et al., *Additive synthesis of advanced nanostructures by high performance low temperature infilling.* unpublished, 2014.
144. Chen, S.-Y., et al., *Electron energy loss spectroscopy and ab initio investigation of iron oxide nanomaterials grown by a hydrothermal process.* Physical Review B, 2009. **79**(10): p. 104103.
145. Miedema, P.S. and F.M.F. de Groot, *The iron L edges: Fe 2p X-ray absorption and electron energy loss spectroscopy.* Journal of Electron Spectroscopy and Related Phenomena, 2013. **187**(0): p. 32-48.
146. Li, H. and G. Selvaduray. *Ellingham Diagram Web Project*. 2013 [cited 2013 8 Aug]; Available from: http://www.engr.sjsu.edu/ellingham/.
147. Kim, H.-S., et al., *Fe-Fe3O4 Composite Electrode for Lithium Secondary Batteries.* Journal of the Electrochemical Society, 2012. **159**(3): p. A325-A329.
148. Lee, S.H., et al., *Self-Assembled Fe3O4 Nanoparticle Clusters as High-Performance Anodes for Lithium Ion Batteries via Geometric Confinement.* Nano Letters, 2013. **13**(9): p. 4249-4256.
149. Kumar, D., et al., *High coercivity and superparamagnetic behavior of nanocrystalline iron particles in alumina matrix.* Journal of Magnetism and Magnetic Materials, 2001. **232**(3): p. 161-167.
150. Gangopadhyay, S., et al., *MAGNETIC-PROPERTIES OF ULTRAFINE IRON PARTICLES.* Physical Review B, 1992. **45**(17): p. 9778-9787.